AD NUMBER: AD0848028

LIMITATION CHANGES

TO:

Approved for public release; distribution is unlimited.

FROM:

Distribution authorized to Department of Defense components only; Administrative/Operational Use; 01 SEP 1968 Other requests shall be referred to Army Electronics Command, Fort Monmouth, NJ.

AUTHORITY

USAEC ltr dtd 28 JAN 1971

AD

Research and Development Technical Report
ECOM-0088-1

MICROWAVE SYNTHESIS TECHNIQUES

ANNUAL REPORT

By

E. G. Cristal *D. K. Adams*

R. Y. C. Ho *S. B. Cohn*

SEPTEMBER 1968

DISTRIBUTION STATEMENT

Each transmittal of this document outside the Department of Defense must have prior approval of CG, U.S. Army Electronics Command, Fort Monmouth, N.J., Attn: AMSEL-KL-EM

ECOM

UNITED STATES ARMY ELECTRONICS COMMAND · FORT MONMOUTH, N.J. 07703

CONTRACT DAAB07-68-C-0088

STANFORD RESEARCH INSTITUTE

Menlo Park, California 94025

NOTICES

Disclaimers

The findings in this report are not to be construed as an official Department of the Army position, unless so designated by other authorized documents.

The citation of trade names and names of manufacturers in this report is not to be construed as official Government endorsement or approval of commercial products or services referenced herein.

Disposition

Destroy this report when it is no longer needed. Do not return it to the originator.

Reports Control Symbol
OSD-1366

TECHNICAL REPORT ECOM 0088-1

SEPTEMBER 1968

MICROWAVE SYNTHESIS TECHNIQUES

ANNUAL REPORT

1 OCTOBER 1967 TO 30 JUNE 1968

SRI Project 6884

CONTRACT DAAB07-68-C-0088

Prepared By

E. G. CRISTAL D. K. ADAMS R. Y. C. HO S. B. COHN

STANFORD RESEARCH INSTITUTE

MENLO PARK, CALIFORNIA 94025

For

U.S. ARMY ELECTRONICS COMMAND, FORT MONMOUTH, N.J. 07703

ABSTRACT

Four major topics of research related to microwave synthesis techniques are covered: slot-line theory and applications, microstrip parallel-coupled-resonator filters, commensurate transmission-line all-pass equalizers, and active filters for UHF and microwave frequencies.

Slot line consists of a narrow gap in a conductive coating on one side of a dielectric substrate, the other side of the substrate being bare. If the substrate's permittivity is sufficiently high, such as ϵ_r = 10 to 30, the slot-mode wavelength will be much smaller than free-space wavelength, and the fields will be closely confined to the slot. Possible applications of slot line to filters, couplers, ferrite devices, and circuits containing semiconductor elements are discussed. Slot line can be used either alone or in conjunction with microstrip line on the opposite side of the substrate. A "second-order" analysis yields formulas for slot-line wavelength, phase velocity, group velocity, characteristic impedance, and effect of adjacent electric and magnetic walls.

Modified and alternative design equations for microstrip parallel-coupled-resonator filters are presented. Computed VSWR responses are given for designs having coupled lines with even- to odd-mode propagation velocity ratios of 1.0, 0.95, and 0.90. The responses show that practical, controlled designs are obtainable in all cases. Also presented are useful design data for microstrip directional couplers.

A general theory of commensurate transmission-line all-pass equalizers operating in either TEM, TE, or TM modes is presented. Application of the theory to practical problems is straightforward, and circuit realizations of the equalizers are often simply related to easily computed design curves. Although the theory, strictly speaking, is for commensurate transmission-line networks, it is not essential that the network being equalized, or even that the equalizer itself,

be of commensurate-length lines. Design formulas for narrow-band equalizers of up to two cavities are presented, and a method for extending the design to a greater number of cavities is described. The effect of equalizer dissipation loss is investigated and briefly described. Two example designs are presented.

A technique is described for using transistors directly as high-Q inductors at microwave frequencies. Several experimental bandpass filters have been built and tested to verify usefulness of the inductive transistor circuit. Stable filters with unity insertion loss have been realized at UHF. Observations made during temperature cycling show that environmental stabilization can also be achieved. Analysis has been made of noise figure and nonlinear distortion, and supporting experimental data are provided. The inductive transistor circuit is expected to be practical for a variety of small-signal filtering and multiplexing applications.

PURPOSES OF THE CONTRACT

The purposes of this contract are to develop techniques for the design of passive and active filters and components in the VHF to microwave frequency range, and to determine the electromagnetic properties of slot line for integration with microstrip technology.

CONTENTS

ABSTRACT iii

PURPOSES OF THE CONTRACT v

LIST OF ILLUSTRATIONS xi

LIST OF TABLES xvii

I INTRODUCTION 1

A. Slot Line 1

B. Design Considerations for Microstrip Parallel Coupled Resonator Bandpass Filters and Directional Couplers 1

C. Theory and Design of Commensurate Transmission-Line All-Pass Equalizers 2

D. Active Filters for UHF and Microwave Frequencies . . 3

II SLOT LINE 5

A. General 5

B. Approximations for Slot Line 10

C. Basis of Second-Order Solution 14

REFERENCES 19

III DESIGN CONSIDERATIONS FOR MICROSTRIP PARALLEL COUPLED RESONATOR BANDPASS FILTERS AND DIRECTIONAL COUPLERS . . . 21

A. General 21

B. Coupled Microstrip Transmission Lines 21

C. Modification of the Design Equations 26

1. Example Design C-1 (α = 0.95) 30
2. Example Design C-2 (α = 0.90) 34
3. Example Design C-3 (α = 0.95) 35
4. Example Design C-4 (α = 0.90) 38

D. Alternate Design Equations 38

1. Example Design D-1 (α = 0.95) 40
2. Example Design D-2 (α = 0.90) 42
3. Example Design D-3 (α = 0.95) 44
4. Example Design D-4 (α = 0.90) 46

E. Microstrip Directional Couplers 46

REFERENCES 49

IV THEORY AND DESIGN OF TRANSMISSION-LINE ALL-PASS EQUALIZERS 53

A. General 53

B. Theory. 54

C. Synthesis 66

D. Practical Circuit Realizations. 67

E. Example Equalizer Designs 77

F. Equalizer Dissipation Loss. 81

REFERENCES 83

V ACTIVE FILTERS FOR UHF AND MICROWAVE FREQUENCIES 85

A. The Internal Inductive Properties of a Transistor . 86

1. Impedance Rotation 87
2. The Useful Influence of Parasitics on Inductive Transistor Effects 88

B. Analysis of a High-Q Inductive Transistor Circuit . 89

C. Physical Model of the Inductive Transistor Effect . 96

D. Active Microwave Filters Using Inductive Transistors 97

1. Insertion Loss and Pass-Band Shape of Active Bandpass Filters. 98
2. Stability of High-Q Active Resonators. 100
3. Initial Results on Filter Tunability 104

E. Large Signal Limitations of Inductive Transistors . 104

F. Noise Characterization of Inductive Transistor Filters 111

REFERENCES 117

VI CONCLUSIONS. 119

A. Slot Line 119

B. Design Considerations for Microstrip Parallel Coupled Resonator Bandpass Filters and Directional Couplers. 119

C. Theory and Design of Transmission-Line All-Pass Equalizers 121

D. Active Filters for UHF and Microwave Frequencies. . 121

Appendix A--ALGORITHM FOR SYNTHESIS OF REACTANCE FUNCTIONS IN A CASCADE OF COMMENSURATE TRANSMISSION LINES . 123

Appendix B--MICROWAVE EQUIVALENT CIRCUIT OF THE INVERTED COMMON-COLLECTOR TRANSISTOR CONFIGURATION 127

Appendix C--LARGE SIGNAL CHARACTERIZATION OF THE INDUCTIVE TRANSISTOR CIRCUIT. 131

Appendix D--NOISE MEASUREMENT TECHNIQUES FOR ACTIVE FILTERS . 137

DISTRIBUTION LIST 143

DD Form 1473

ILLUSTRATIONS

Fig. II-1	Slot Line on a Dielectric Substrate.	5
Fig. II-2	Field and Current Distribution	6
Fig. II-3	Simple Transition between Slot Line and Microstrip	7
Fig. II-4	Broadband Transition between Slot Line and Miniature Semi-Rigid Coaxial Line.	8
Fig. II-5	Resonant Slots	8
Fig. II-6	Filter Applications.	9
Fig. II-7	Cylindrical Coordinates with Axis on Center Line of Slot	11
Fig. II-8	Development of Waveguide Models for Slot-Line Solution	16
Fig. III-1	Diagrammatic Form of Parallel-Coupled-Resonator Bandpass Filter.	22
Fig. III-2	Fractional Bandwidth for Microstrip Coupled Lines ($\alpha = \theta_e/\theta_o$).	25
Fig. III-3	Center Frequency Shift of Image Pass Band for Coupled Microstrip Lines	25
Fig. III-4	VSWR Response of Example Design C-1 Using Modified Design Equations ($\alpha = 1.0$).	31
Fig. III-5	VSWR Response of Example Design C-1 Using Modified Design Equations ($\alpha = 0.95$)	31
Fig. III-6	VSWR Response of Example Design C-1 Using Modified Design Equations with the First and Last Coupled Sections Lengthened by 1 Percent ($\alpha = 0.95$)	32
Fig. III-7	VSWR Response of Example Design C-2 Using Modified Design Equations ($\alpha = 0.90$)	32
Fig. III-8	VSWR Response of Example Design C-2 Using Modified Design Equations with the First and Last Sections Lengthened by 3 Percent ($\alpha = 0.90$)	33
Fig. III-9	VSWR Response of Example Design C-3 Using Modified Design Equations ($\alpha = 1.0$).	36
Fig. III-10	VSWR Response of Third Example Design C-3 Using Modified Design Equations ($\alpha = 0.95$) . .	36

Fig. III-11	VSWR Response of Example Design C-3 Using Modified Design Equations with the First and Last Sections Lengthened by 3 Percent (α = 0.95)	37
Fig. III-12	VSWR Response of Example Design C-4 Using Modified Design Equations (α = 0.90)	37
Fig. III-13	VSWR Response of Example Design D-1 Using Alternate Design Equations (α = 1.0)	41
Fig. III-14	VSWR Response of Example Design D-1 Using Alternate Design Equations (α = 0.95)	41
Fig. III-15	VSWR Response of Example Design D-1 Using Alternate Design Equations with the First and Last Sections Lengthened by 1.5 Percent (α = 0.95)	42
Fig. III-16	VSWR Response of Example Design D-2 Using Alternate Design Equations (α = 0.90)	43
Fig. III-17	VSWR Response of Example Design D-2 Using Alternate Design Equations with the First and Last Sections Lengthened by 3 Percent (α = 0.90)	43
Fig. III-18	VSWR Response of Example Design D-3 Using Alternate Design Equations (α = 1.0)	45
Fig. III-19	VSWR Response of Example Design D-3 Using Alternate Design Equations (α = 0.95)	45
Fig. III-20	VSWR Response of Example Design D-4 Using Alternate Design Equations (α = 0.90)	46
Fig. III-21	Shift in the Location of the Peak Coupling for Microstrip Directional Couplers.	48
Fig. III-22	Decrease in Peak Coupling of Microstrip Directional Couplers	48
Fig. III-23	Theoretical Maximum Directivity for -3.01-dB Microstrip Directional Couplers.	50
Fig. III-24	Theoretical Maximum Directivity for -6.02-dB Microstrip Directional Couplers.	50
Fig. III-25	Theoretical Maximum Directivity for -10.0-dB Microstrip Directional Couplers.	51
Fig. III-26	Theoretical Maximum Directivity for -20.0-dB Microstrip Directional Couplers.	52
Fig. III-27	Theoretical Maximum Directivity for -30.0-dB Microstrip Directional Couplers.	52
Fig. IV-1	Normalized Time Delay of C-Section Waveguide Equalizer.	59

Fig. IV-2	Normalized Time Delay of D-Section Waveguide Equalizer with $\|t_o\|$ Constant and σ_o as a Parameter.	60
Fig. IV-3	Normalized Time Delay of D-Section Waveguide Equalizer with σ_o Constant and $\|t_o\|$ as a Parameter.	61
Fig. IV-4	Diagram of an Idealized, General, Microwave Equalizer.	63
Fig. IV-5	General Reactance Network in the Form of Cascaded Transmission Lines.	67
Fig. IV-6	Inductive Coupled Two-Cavity Reactance Network for a Second-Order Microwave Equalizer.	70
Fig. IV-7	Equivalent Network to that of Fig. IV-6 Using Impedance Inverters.	71
Fig. IV-8	Capacitive Coupled Two-Resonator Reactance Network for a Second-Order TEM Transmission-Line Equalizer	74
Fig. IV-9	Differential Delays of Microwave Filter and C-Section Equalizers for Example in Text . . .	78
Fig. IV-10	Differential Delays of Microwave Filter and D-Section Equalizer for Example in Text. . . .	80
Fig. IV-11	Dissipation Loss of a Microwave D-Section Equalizer.	82
Fig. V-1	Active-Filter Resonator, Suitable for Low-Frequency Applications	85
Fig. V-2	Inductive Transistor Circuit Suitable for Microwave Applications	86
Fig. V-3	Inverted Common-Collector Circuit for Realizing Stable, High-Q Inductance at Microwave Frequencies.	89
Fig. V-4	Reflected Reactance and Resistance Components of Z' in Fig. V-3, Excluding the Contribution of r_e	92
Fig. V-5	Measured Emitter Impedance of 2N3866 Transistor in the Inverted Common-Collector Configuration, Excluding the Contribution of r_e	93
Fig. V-6	Theoretical Prediction of the Maximum Obtainable x_m for Two Grounded Collector Configurations as a Function of f_{max}/f_α of the Transistor Used.	95

Fig. V-7	Cross Section of a Typical Microwave Transistor	96
Fig. V-8	Bandpass Filter Configuration Used for Active Resonator Testing	98
Fig. V-9	Two-Resonator, Active Bandpass Filter for UHF Application	99
Fig. V-10	Typical Pass Band Obtained with the Filter in Fig. V-9	100
Fig. V-11	Computed Response of Three Five-Resonator Transistor Filters	101
Fig. V-12	Pass Band Shape of the Two-Resonator Active Filter at 620 MHz Compared with a 0.1 dB Ripple Prototype	102
Fig. V-13	Insertion Loss Temperature Dependence of the Active Filter in Fig. V-9	103
Fig. V-14	Comparison of Large- and Small-Signal Pass Band and Insertion Loss for the Two-Resonator Active Filter	105
Fig. V-15	Small- and Large-Signal Reflection Characteristics of Two-Resonator Active Filter, Showing Limiting Effect	107
Fig. V-16	Comparison of the Saturation Effects Produced by the Coefficient a_3 for Low and High Bias Voltage (and Current)	110
Fig. V-17	Measured Third-Order Intermodulation Coefficient vs. Bias Current for the Two-Resonator Active Filter	112
Fig. V-18(a)	Noise Sources in the Inductive Transistor Circuit	113
Fig. V-18(b)	Norton Equivalent Circuit	113
Fig. V-19	Noise Equivalent Circuit of the n-Resonator Capacitively-Coupled Active Filter	114
Fig. B-1	Transistor Model, Showing Package and Interelectrode Parasitics	129
Fig. C-1	Equivalent Circuit of a Symmetrically Coupled, Single-Resonator Filter	133
Fig. D-1	Block Diagram of Equipment Used to Measure Active Filter Noise Figure	139
Fig. D-2	Simplified Equivalent Network for Fig. D-1	139

Fig. D-3 Noise Figure of the Network in Fig. D-2 vs. Insertion Loss of L_2 141

Fig. D-4 Block Diagram of Equipment Used for the Direct Measurement of Active Filter Noise Figure 142

TABLES

Table I E_{φ} and V(r)/V vs. r and r/λ. 14

Table II Matthaei's Design Equations for Parallel-Coupled Filters. 27

Table III Alternate Design Equations for Parallel-Coupled Filters. 39

Table IV Formulas for All-Pass Equalizers 68

I INTRODUCTION

A. Slot Line

Microstrip integrated circuits on a dielectric substrate are currently the subject of widespread interest and application. Section II shows that microstrip is not the only kind of transmission line that can be deposited or etched on a substrate. An alternative is slot line, which may be used by itself or in conjunction with microstrip. Slot line consists of a narrow gap in a conductive coating on one side of a substrate, the other side being open to the surrounding air. The nature of the slot mode appears to offer interesting possibilities for realization of filters, ferrite devices, and other components, as well as complete circuits including semiconductor elements. The theoretical analysis outlined in this report yields formulas for all of the basic electrical parameters: wavelength, phase velocity, group velocity, and characteristic impedance. Also, the effect of adjacent electric and magnetic walls is determined. Despite the non-TEM nature of the mode, and the inhomogeneous dielectric cross section, the analytical approach appears capable of high accuracy. Work is continuing on theoretical computation and measurement of slot-wave parameters, and applications to components and circuits are planned.

B. Design Considerations for Microstrip Parallel Coupled Resonator Bandpass Filters and Directional Couplers

The increasing importance of small planar microwave circuits has generated new interest in microstrip media. Unfortunately, however, microstrip media does not support a TEM mode, although the mode configuration is often sufficiently close to TEM that useful engineering designs can be obtained by assuming that it alone is present. One area where this assumption leads to difficulty is in designs that call for coupled microstrip lines. Here it is found that the even- and odd-mode propagation velocities are unequal. Consequently, the usual TEM equivalent circuits for coupled lines are invalid, and all component designs based on these circuits are, strictly speaking, invalid. Of course, one may boldly

proceed to use the standard design equations anyway and see whether the resulting design satisfies the required specifications. But what if it doesn't?

The answer to this question is to develop new, or modified, design equations which take into account, as much as possible, the degrading effects of unequal even- and odd-mode propagation velocities. However, there are a large number of components using coupled lines. Which one should be investigated first? It was decided that the parallel-coupled-resonator bandpass filter should be given priority for several reasons: (1) because of its suitability for microstrip, (2) because it can be designed for both narrow and wide bandwidths, and (3) because of its potential use in diplexer and multiplexer applications. In Sec. III both modified and new alternate design equations for parallel-coupled-resonator bandpass filters are presented. Many computer calculations testing the modified and alternative equations are presented.

Another important microwave component is the quadrature directional coupler. In Sec. III useful design data for microstrip couplers are also presented.

C. Theory and Design of Transmission-Line All-Pass Equalizers

In microwave filter design it is most common to specify requirements on insertion loss, selectivity, and VSWR. Time delay and phase are often not mentioned. However, there are many applications in which the latter characteristics are equally important. In some components, such as phase shifters, delay lines, and pulse compression devices, they are the more important characteristics. In microwave filters phase can be controlled by designing nonminimum phase filters. However, this is usually very difficult in the microwave region. What is usually done is to design the filters to meet loss, selectivity, and VSWR specifications, with little regard paid to the phase (or delay), and then to equalize the phase (or delay) by means of a low-loss equalizer.

Although many authors have treated various aspects of microwave equalizer design, no unifying principle appears to have been described

that relates the various known techniques to one another, or that permits their extension to higher-order networks, with the exception of the work of J. O. Scanlan for TEM networks. However, in Sec. IV a general theory for microwave equalizers is presented, which is equally valid for both waveguide and TEM transmission lines. Also described are synthesis procedures, practical circuit realizations, and two design examples.

D. Active Filters for UHF and Microwave Frequencies

Miniaturization of commonly used microwave circuits is often retarded by the lack of compact filter designs. Although design techniques for conventional microwave filters have reached an advanced state, filter size is still a serious problem. With passive-filter techniques, the available trade-off is size for element Q, but low-Q resonators yield poor filter selectivity and high insertion loss. Active filters offer another trade-off, size for dynamic range, but practical active filters for UHF and microwave frequencies have not existed until the present time. Section V of this report describes a transistor circuit configuration that is capable of producing stable, high-Q inductance up to and above the alpha-cutoff frequency of the transistors used. The inductive effect in a transistor is mainly an internal mechanism arising from carrier diffusion delay, and does not require highly stable feedback networks. Experimental filters have been built at UHF and tests conducted to evaluate temperature stability, noise figure, and nonlinear distortion. Analysis is presented which explains the experimental observations.

II SLOT LINE

A. General

There has recently been a strong revival of interest in microstrip transmission line on a dielectric substrate for microwave-integrated-circuit applications. This section describes an alternative transmission line on a dielectric substrate that may be used with microstrip or instead of microstrip. As shown in Fig. II-1, this alternative consists of a narrow slot or gap in a conductive coating on one side of the substrate. The other side of the substrate is exposed directly to air.

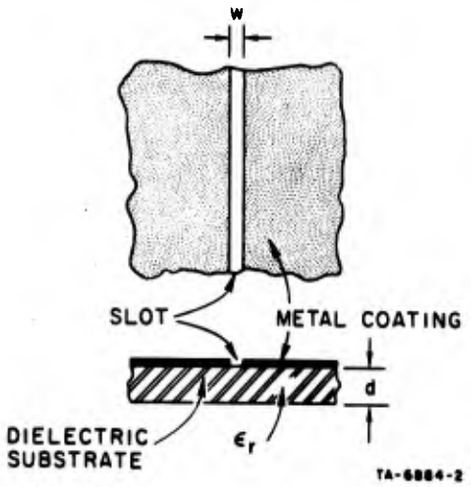

FIG. II-1 SLOT LINE ON A DIELECTRIC SUBSTRATE

Both resonant and propagating slots in thin conductive sheets have had extensive use as radiating elements in microwave antennas. (For example, see Refs. 1, 2, and 3, and their bibliographies.)* For slot line to be practical as a transmission line, radiation must be minimized. This is accomplished through the use of a high-permittivity

---

*References are listed at the end of each section.

substrate, which causes the slot-mode wavelength λ' to be small compared to free-space wavelength λ, and thereby results in the fields being closely confined to the slot with negligible radiation loss. For example, if $\epsilon_r = 20$, then $\lambda'/\lambda \approx 1/3$, and analysis shows the slot-mode fields to be sharply attenuated at a distance $r/\lambda = 1/8$, or $r = 0.5$ in at 3 GHz.

Figure II-2(a) shows the slot-mode fields in a cross-sectional view. A voltage difference V exists between the slot edges. The electric field extends across the slot; the magnetic field is perpendicular to the slot. Because the voltage occurs across the slot, the configuration is especially convenient for connecting shunt elements such as diodes, resistors, and capacitors. The longitudinal view in Fig. II-2(b) shows that in the

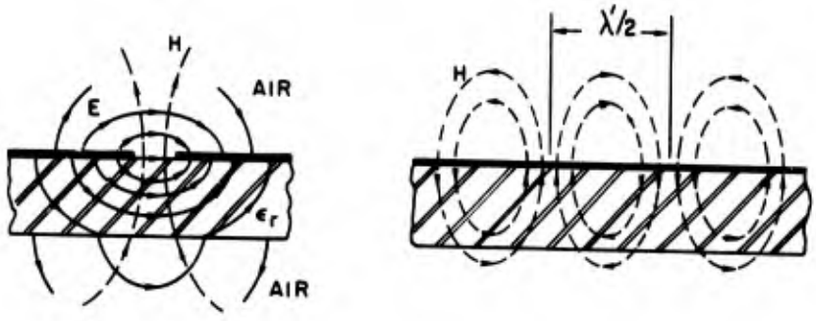

(a) FIELD DISTRIBUTION IN CROSS-SECTION

(b) H FIELD IN LONGITUDINAL SECTION

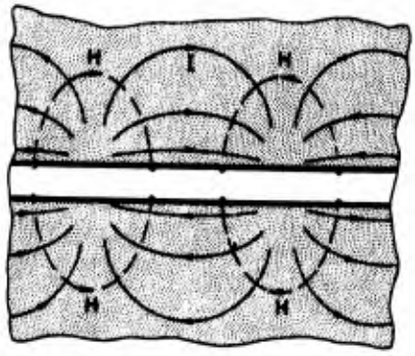

(c) CURRENT DISTRIBUTION ON METAL SURFACE

TA-6884-4R

FIG. II-2 FIELD AND CURRENT DISTRIBUTION

air regions the magnetic field lines curve and return to the slot at half-wavelength intervals. Consequently, a propagating wave has elliptically polarized regions that can be usefully applied in creating certain ferrite components. The current paths on the conducting surface are shown in Fig. II-2(c). The surface-current density is greatest at the edges of the slot and decreases rapidly with distance from the slot. A propagating wave has regions of elliptically polarized current and magnetic field in this view, also. In fact, in a transverse cross-section of slot line, the magnetic field is elliptically polarized at all points.

An interesting possibility for microwave integrated circuits is the use of slot lines on one side of a substrate and microstrip lines on the other. When close to each other, coupling between the two types of lines will exist, and when sufficiently far apart they will be independent. Coupling between a slot and a strip can be used intentionally in certain components. For example, parallel lengths of slot and strip can be made to act as a directional coupler. If a slot and strip cross each other at right angles, as in Fig. II-3, coupling will be especially tight, and a transition covering approximately 30-percent bandwidth can be achieved when the characteristic impedances of the strip and slot lines are equal and when the strip and slot are extended approximately one-quarter wavelength beyond the point of crossing. With matching techniques, a bandwidth of an octave or so should be feasible.

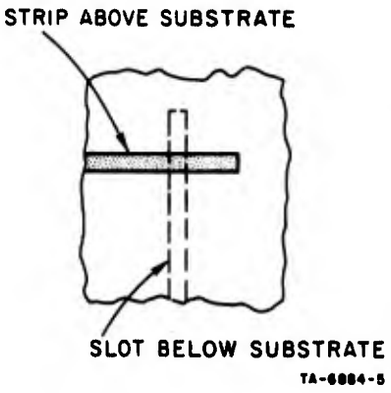

FIG. II-3 SIMPLE TRANSITION BETWEEN SLOT LINE AND MICROSTRIP

Figure II-4 shows one way that a wideband transition between miniature-cross-section coaxial line and slot line can be made. Additional structural details may be needed to obtain optimum matching and to prevent radiation loss.

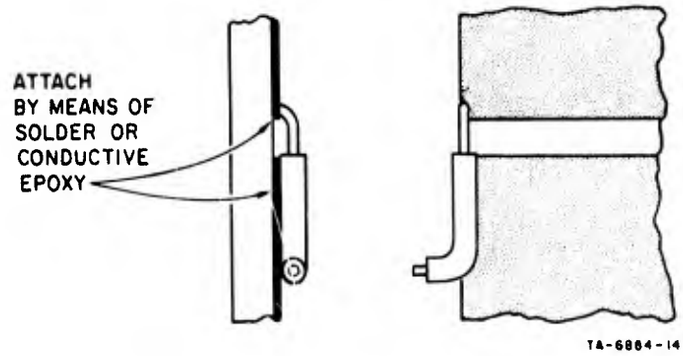

FIG. II-4 BROADBAND TRANSITION BETWEEN SLOT LINE AND MINIATURE SEMI-RIGID COAXIAL LINE

A half-wavelength slot as shown in Fig. II-5(a) can be used as a resonator. If desired, the resonant slot may be made more compact by capacitively loading its center as in Fig. II-5(b), or by bending it as

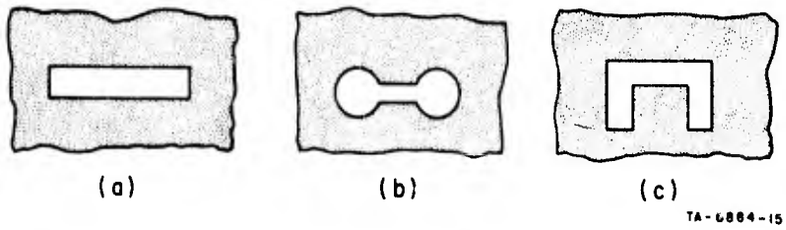

FIG. II-5 RESONANT SLOTS

in Fig. II-5(c). Applications to bandstop and bandpass filters are shown in Fig. II-6. In the bandstop example, the terminating lines are microstrip, and in the bandpass example they are slot lines. Many other filter configurations are feasible, using slots alone or slots with strips on the opposite side of the substrate.

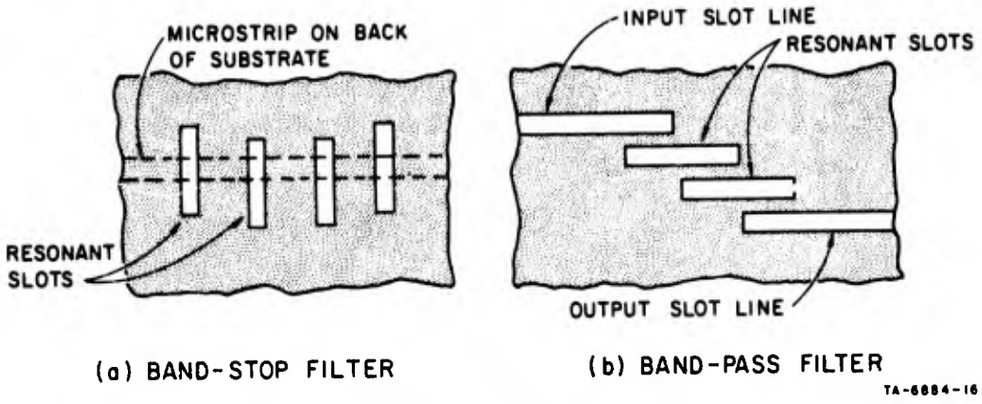

FIG. II-6 FILTER APPLICATIONS

The basic electrical parameters of a slot line are the characteristic impedance Z_o and the phase velocity v. Relative velocity and wavelength are $v/c = \lambda'/\lambda$, where c is velocity of light, λ' is slot-line wavelength, and λ is free-space wavelength. Because of the non-TEM nature of the slot-line mode, these relative parameters are not constant, but vary with frequency at a rather slow rate per octave. This behavior contrasts with quasi-TEM microstrip line, whose Z_o and v/c are very nearly independent of frequency from dc to the highest frequency of ordinary interest. On the other hand, slot line differs from waveguide in that it has no cutoff frequency. Propagation along the slot occurs at all frequencies down to $f = 0$, where, if the metal-coated substrate is assumed infinite in length and width, v/c approaches unity and Z_o approaches zero. Other important parameters are the ratio of phase velocity to group velocity v/v_g, the effect of adjacent walls on the basic parameters, and the minimum allowable spacing of such walls from the slot for negligible effect. In the remainder of this section approximate formulas are given, and the basis of a second-order theory presented.

Theoretical and experimental studies are being continued under an extension of the program covered by this report. Theoretical topics are planned to include computation of families of design curves of Z_o and λ'/λ versus slot width, permittivity, and thickness of the substrate;

attenuation and Q_u of slot line; coupling between slots and between a slot and a microstrip; and design theory for filters, ferrite devices, and other components. Experimental studies will be carried out to determine the accuracy of the various theoretical formulas. The design of broadband transitions of slot line to coaxial line and microstrip will be investigated, and components such as directional couplers, filters, and various ferrite devices will be designed and tested.

B. Approximations for Slot Line

Half-wavelength slots in a conducting sheet have had extensive applications in antennas as radiating elements.[1,2,3] The slots are typically open on one side to free space and coupled on the other side to a waveguide or TEM line. If dielectric material is used near the slot, it is usually intended to serve a mechanical purpose only, and its electrical effect is minimized.

Several references on slot antennas were found in which the presence of a substantial amount of dielectric material in or near the slot was taken into account. Strumwasser, Short, Stegen, and Miller[4] have studied experimentally the effects of filling a slot in a thick metal plate with dielectric material. They give data on resonant-length reduction and radiation resistance coupled into an air-dielectric TEM line. M. C. Bailey[5] has measured resonant length and radiation conductance of a slot in a waveguide wall covered by a protective layer of dielectric material. J. Galejs[6] has analyzed theoretically a slot in a zero-thickness, perfectly conducting sheet separating free space from a lossy dielectric medium of infinite extent. For example, a slot radiator in a wire mesh on the surface of the ground would be simulated by this model.

Galejs utilizes an integral-equation method to obtain complex expressions for radiation efficiency and other parameters of the slot antenna. His zero-order solution for the propagation constant along the slot can be easily modified into the following simple formula for relative wavelength:

$$\frac{\lambda'}{\lambda} = \sqrt{\frac{2}{\epsilon_r + 1}} \quad . \tag{II-1}$$

Since wavelength is inversely proportional to the square root of permittivity, an effective permittivity of a uniform medium replacing the two different dielectric half spaces may be defined as

$$\epsilon_r' = \frac{\epsilon_r + 1}{2} \quad . \tag{II-2}$$

The second-order solution for slot line, derivation of which is outlined later in this section, shows that Eq. (II-1) is a fair approximation for slot line, yielding values within about 10 percent in typical slot-line cases. The second-order solution shows quantitatively how λ'/λ varies with the parameters d, w, ϵ_r, and λ.

The field components on the air side of the slot can be computed quite easily as a function of distance r from the slot (Fig. II-7), free space wavelength λ, and slot wavelength λ'. If we assume $w/\lambda \ll 1$, then

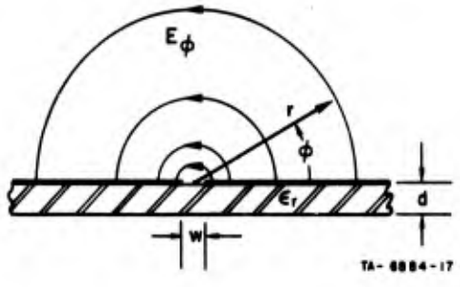

FIG. II-7 CYLINDRICAL COORDINATES WITH AXIS ON CENTER LINE OF SLOT

the electric voltage across the slot may be replaced by an equivalent line source of magnetic current. At a distance r at least several times larger than w the longitudinal component of magnetic field is given by[7]

$$H_z = A\, H_o^{(1)}(k_c r) \tag{II-3}$$

where $H_n^{(1)}(x)$ is the Hankel function of first kind, order n, and argument x. The coefficient k_c is

$$k_c = \sqrt{\gamma_z^2 + k^2} \qquad \text{(II-4)}$$

where

$$\gamma_z = j\frac{2\pi}{\lambda_z} = j\frac{2\pi}{\lambda'}$$

$$k = \frac{2\pi}{\lambda} \quad .$$

Therefore,

$$k_c = j\frac{2\pi}{\lambda}\sqrt{\left(\frac{\lambda}{\lambda'}\right)^2 - 1} \quad . \qquad \text{(II-5)}$$

By Eq. (II-1), a zero-order value of k_c is

$$k_c = j\frac{2\pi}{\lambda}\sqrt{\frac{\varepsilon_r - 1}{2}} \quad . \qquad \text{(II-6)}$$

The other field components are H_r and E_φ. They are related to H_z by[7]

$$H_r = -\frac{\gamma_z}{k_c^2}\frac{\partial H_z}{\partial r} = \frac{A}{\sqrt{1 - \left(\frac{\lambda'}{\lambda}\right)^2}} H_1^{(1)}(k_c r) \qquad \text{(II-7)}$$

$$E_\varphi = \frac{j\omega\mu}{k_c^2}\frac{\partial H_z}{\partial r} = \frac{-\eta(\lambda'/\lambda)A}{\sqrt{1 - \left(\frac{\lambda'}{\lambda}\right)^2}} H_1^{(1)}(k_c r) \qquad \text{(II-8)}$$

where the identity $d\left[H_o^{(1)}(x)\right]/dx = -H_1^{(1)}(x)$ was used.

The Hankel function of imaginary argument, $H_n^{(1)}(j|x|)$, approaches zero proportional to $e^{-|x|}/\sqrt{|x|}$ for $|x|$ large. For n = 0 the function is negative imaginary and for n = 1 it is negative real. Tabulations of $jH_o^{(1)}(j|x|)$ and $-H_1^{(1)}(j|x|)$ are given by Jahnke and Emde.[8] Equation (II-5) shows that the argument $k_c r$ is imaginary for $\lambda'/\lambda < 1$. Hence a relative wavelength ratio less than unity is a sufficient condition to

ensure decay of the slot-mode field with radial distance. As λ'/λ is decreased, the decay becomes sharper, and the fields become more tightly bound to the slot.

A radius r_{cp} of circular polarization of the magnetic field requires $|H_z/H_r| = 1$. By means of Eqs. (II-3) and (II-7), r_{cp} must satisfy

$$\left| \frac{H_1^{(1)}(k_c r_{cp})}{H_0^{(1)}(k_c r_{cp})} \right| = \sqrt{1 - \left(\frac{\lambda'}{\lambda}\right)^2} \quad . \qquad \text{(II-9)}$$

However, tables show that $|H_1^{(1)}(j|x|)| > |H_0^{(1)}(j|x|)|$ for all $|x|$. Since the right-hand side of Eq. (II-9) is less than one, a solution for r_{cp} does not exist. Nevertheless, elliptical polarization occurs for all r, and low axial ratios occur for r sufficiently large. Circular polarization may exist on the substrate side of the slot, but this has not yet been investigated.

Also of interest is the ratio of voltage along a semicircular path at constant radius divided by the voltage directly across the slot. This ratio is

$$\frac{V(r)}{V} = \frac{k_c r \, H_1^{(1)}(k_c r)}{\lim_{|x|\to 0} \left[|x| H_1^{(1)}(j|x|) \right]} = \frac{\pi}{2} k_c r \, |H_1^{(1)}(k_c r)| \quad . \qquad \text{(II-10)}$$

As an example of field decay, let $\epsilon_r = 16$, f = 3 GHz, and $\lambda = 4$ in. The zero-order value of λ'/λ is 0.343, and of $k_c r$ is 4.30 r, where r is in inches. Table I shows how E_φ and V(r)/V vary in relation to r and r/λ. If a plane metal wall is positioned perpendicular to the radius vector at distance r/2 from the slot, an image of the slot will appear at distance r/2 behind the wall. The effect will be that of two equally excited parallel slots spaced by r. Thus if the metal wall is at distance 0.5 in in the above example, r = 1 in and V(r)/V of one slot is down by 28.36 dB at the other slot. Coupling between slots is even weaker than this, since only part of the total voltage V(r) of one slot affects the other slot.

Table I

E_φ AND V(r)/V VS. r AND r/λ

r (inches)	r/λ	$E_\varphi \propto \lvert H_1^{(1)}(k_c r) \rvert$	V(r)/V	20 $\log_{10}$ V(r)/V (dB)
0	0	∞	1.000	0
0.05	0.0125	2.81	0.950	-0.44
0.1	0.025	1.274	0.861	-1.28
0.2	0.05	0.490	0.663	-3.57
0.3	0.075	0.241	0.489	-6.23
0.5	0.125	0.0733	0.248	-12.11
0.7	0.175	0.0253	0.120	-18.42
1.0	0.250	0.00565	0.0382	-28.36
1.3	0.325	0.00134	0.0118	-38.58

We may conclude for the parameters of the above example that a metal wall or other perturbing object can be placed as close as r = 0.5 in for f = 3 GHz, or r/λ = 0.125, with very little effect on λ' or Z_o. We may also conclude that the fields and stored energy of the slot mode are mainly confined within this same radial distance, and that this is true on the substrate side of the slot as well as on the air side. These conclusions have been verified both by experiment and by computations using the second-order solution.

C. Basis of Second-Order Solution

An analytical approach for slot line offering high accuracy is described in this section. The solution obtained by this approach will be referred to as second order. A first-order solution offering intermediate complexity and accuracy between zero-order Eq. (II-1) and the second-order equations would also be useful, but has not yet been completed.

The key feature of the approach used in the second-order solution is the introduction of boundary walls permitting the slot-line configuration to be treated as a rectangular-waveguide problem rather than a

problem in cylindrical coordinates. Thus the infinite, orthogonal sets of relatively simple rectangular-waveguide modes apply rather than sets of cylindrical modes embodying all orders of Hankel functions. A further important advantage is that the surfaces of the substrate lie in transverse planes of the rectangular waveguide, permitting matching of fields at these boundaries to be accomplished in the easiest possible manner. The second-order solution obtained by this approach yields the major parameters of slot line as functions of dimensions, dielectric constant, and frequency. Parameters that can be evaluated using the present second-order theory are relative-wavelength ratio λ'/λ, characteristic impedance Z_o, ratio of phase velocity to group velocity v/v_g, and the effect of nearby electric and magnetic walls. Under the continuing program the second-order solution will be extended to yield the even- and odd-mode characteristic impedances and velocities of parallel slots, the effect of metal-coating thickness greater than zero, attenuation per unit length, and unloaded Q of a resonance slot.

Conversion of the slot-line configuration into a rectangular-waveguide problem is illustrated in Fig. II-8. First assume that slot waves of equal amplitude are traveling in the +x and -x directions. Then transverse planes spaced by $\lambda'/2$ exist where the transverse E field and normal H field cancel to zero. Let two such planes occur at $x = 0$ and $x = \lambda'/2 = a$ in Fig. II-8(a). Conducting (or electric) walls of infinite extent may be inserted in these planes without disturbing the field components between the planes, and the semiinfinite regions at $x < 0$ and $x > a$ may be eliminated. The section of slot line between the transverse planes supports a resonant slot-wave mode with no loss of energy, if the dielectric substrate and the conducting walls are assumed dissipationless.

Next, conducting walls are inserted in planes parallel to the slot and perpendicular to the substrate at $y = \pm b/2$. The region separated out of the original infinite space has the rectangular-waveguide boundary shown in Fig. II-8(b). Since the fields are tightly bound to the vicinity of the slot, the walls at $y = \pm b/2$ will have negligible effect

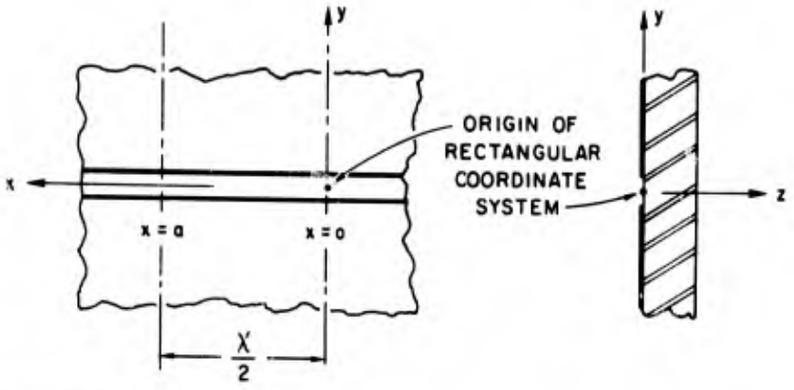

(a) INSERTION OF TRANSVERSE CONDUCTING PLANES AT x = o AND a

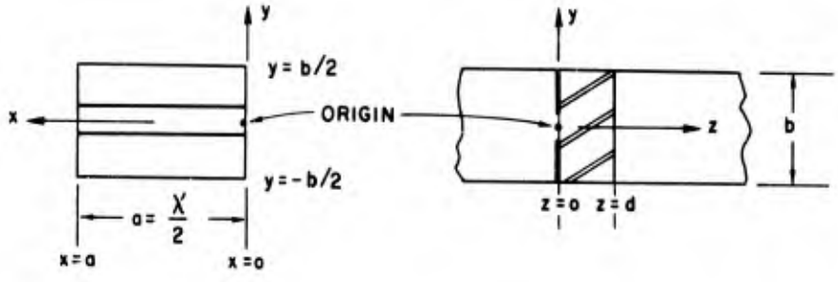

(b) INSERTION OF CONDUCTING PLANES (ELECTRIC WALLS) AT y = ± b/2

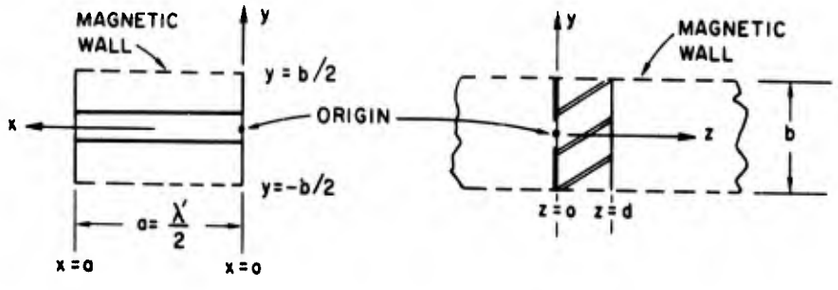

(c) INSERTION OF MAGNETIC WALLS AT y = ± b/2

TA-6884-16

FIG. II-8 DEVELOPMENT OF WAVEGUIDE MODELS FOR SLOT-LINE SOLUTION

on the slot-wave parameters when b is sufficiently large. For example, computation with the second-order solution shows that for $\epsilon_r = 20$, d = 0.137 in, w = 0.025 in, and f = 3.0 GHz, values of Z_o and λ'/λ are perturbed from their $b \to \infty$ values by roughly one percent for b = 1.0 in and 0.1 percent for b = 1.5 in. It is interesting that these walls have

little effect for $b > 1$ in, yet they serve the important function of enabling the use of rectangular-waveguide mode sets, thereby greatly simplifying the analysis. The small effect at $b = 1.0$ in agrees with the conclusion obtained for a similar example from the Hankel-function relation in Sec. II-B, above.

Magnetic walls may be placed at $y = \pm b/2$ instead of electric walls. The result is the rectangular waveguide boundary shown in Fig. II-8(c), where two magnetic walls spaced by b and two electric walls spaced by a are used. The second-order solution has been carried out for the boundaries in both Figs. II-8(b) and II-8(c).

Images of the slot in the electric or magnetic walls at $y = \pm b/2$ result in an infinite array of parallel slots in the $z = 0$ plane having center-to-center spacing of b. Therefore, the effect of adjacent slots may be computed for both electric- and magnetic-wall imaging, allowing the even- and odd-mode characteristic impedances and wavelengths to be evaluated for a slot in an infinite array. For one pair of slots rather than an array, these even- and odd-mode quantities are given approximately by the $b \to \infty$ values modified by one half the change computed for the infinite array. The subject of even- and odd-mode parameters of slot line will be investigated further and treated in a subsequent report.

Thus, the introduction of walls in Fig. II-8 has created the configuration of a capacitive iris in a rectangular waveguide, with air and dielectric regions as indicated. Consider the metal-walled case in Fig. II-8(b). All waveguide modes must have the $\lambda'/2$ variation of the slot wave in the x direction. Also, because of symmetry of the structure, all modes must have an E-field maximum at the center of the slot. Therefore the full set of modes satisfying the boundary conditions are TE_{10}, TE_{12}, TE_{14}, ..., and TM_{12}, TM_{14}, ...; that is, $TE_{1,2n}$ for n an integer ≥ 0 and $TM_{1,2n}$ for $n \geq 1$.

For the slot wave, $\lambda' < \lambda$ and hence $a < \lambda/2$. Therefore, the TE_{10} and all higher modes are cut off, or nonpropagating, in the air regions. In the dielectric region the TE_{10} mode is propagating, and the first few higher modes may propagate or all higher modes may be cut off, depending

on the size of b. Since all modes are cut off in the two air regions, the energy of the resonant slot-wave mode is trapped near the slot. The amplitude of each mode in each region must be such that when the full set of modes are superimposed, the boundary conditions in the iris plane at z = 0 will be met, and all field components on either side of the dielectric-to-air interface at z = d will be matched. An alternative but equivalent condition is that the sum of the susceptances at the iris plane be equal to zero. This sum includes the susceptances of the TE_{10} mode looking in the -z and +z directions, and the capacitive-iris susceptance representing higher modes on the -z and +z sides of the iris. When the iris susceptance for +z is computed, the effect of the dielectric-air interface at z = d must be included.

Total susceptance equal to zero is the transverse-resonance condition for the slot wave. Each set of w, d, b, ϵ_r, and λ determines a unique value of $\lambda' = 2a$ at transverse resonance, thus giving λ'/λ, v/c, and v.

A formula for characteristic impedance has also been derived by a method utilizing the total-susceptance formula. Because of the non-TEM nature of the slot wave, definition of characteristic impedance is somewhat arbitrary. The reasonable and useful definition chosen here is $Z_o = V^2/2P$, where $V = -\int E_y\, dy$ is voltage amplitude across the slot and P is power flow of the wave. Power flow is related to stored energy in the rectangular-waveguide model of a $\lambda'/2$ length of slot line, and to the group velocity of the wave. Stored energy for a given value of V is evaluated from the derivative of total susceptance with respect to frequency, computed at the frequency of transverse resonance. Group velocity is evaluated from the derivative of λ'/λ with respect to frequency. Details of the characteristic-impedance analysis will be in the next report.

REFERENCES

1. H. Jasik, ed.. Antenna Engineering Handbook, Chapter 8 by J. Blass and Chapter 9 by M. J. Ehrlich (McGraw-Hill Book Co., Inc., New York, New York, 1961).

2. A. F. Harvey, Microwave Engineering, pp. 633-638 (Academic Press, New York, 1963).

3. W. H. Watson, Waveguide Transmission and Antenna Systems (Clarendon Press, Oxford, 1947).

4. E. Strumwasser, J. A. Short, R. J. Stegen, and J. R. Miller, "Slot Study in Rectangular TEM Transmission Line," Hughes Aircraft Co. Technical Memo No. 265, Air Force Contract AF 19(122)-454 (January 1952).

5. M. C. Bailey, "Design of Dielectric-Covered Resonant Slots in a Rectangular Waveguide," IEEE Trans., Vol. AP-15, pp. 594-598 (September 1967).

6. J. Galejs, "Excitation of Slots in a Conducting Screen Above a Lossy Dielectric Half Space," IRE Trans., Vol. AP-10, pp. 436-443 (July 1962).

7. S. Ramo and J. R. Whinnery, Fields and Waves in Modern Radio, 2nd Edition, pp. 357-358 (John Wiley and Sons, New York, New York, 1953).

8. E. Jahnke and F. Emde, Tables of Functions with Formulae and Curves, pp. 236-243 (Dover Publications, 1943).

III DESIGN CONSIDERATIONS FOR MICROSTRIP PARALLEL COUPLED RESONATOR BANDPASS FILTERS AND DIRECTIONAL COUPLERS

A. General

Circuit design in microstrip can be much more difficult than in homogeneous media because coupled microstrip lines usually have different velocities of propagation for the even- and odd-mode. In quarter-wave coupled transmission line directional couplers the effects are to significantly degrade the directivity and to shift the frequency at which maximum coupling is normally achieved. In parallel-coupled-resonator bandpass filters the effects are to degrade the pass-band and stop-band responses and to shift the nominal center frequency of the pass band.

One approach to designing microstrip components is to treat each parameter having a different propagation velocity as an independent variable, and then use multivariable network synthesis techniques.[1] Unfortunately, the present state of multivariable network theory makes this approach impractical at this time. A second approach is to attempt to bypass the shortcoming of the medium by designing components that do not use, or at least minimize the use of, coupled lines. The equalizer theory presented next in Sec. IV is an example of this method. A third approach, and the one used in this section for parallel-coupled-resonator bandpass filters, is to modify existing (or develop new) design equations to account for the different velocities of propagation.

B. Coupled Microstrip Transmission Lines

The parallel-coupled-resonator bandpass filter, shown diagrammatically in Fig. III-1, is particularly well suited to microstrip because its resonators need not be grounded. An accurate, though approximate, design procedure for these filters in homogeneous media is the one of Matthaei.[2] Matthaei's method of synthesis is essentially based on image parameter concepts, but with a variation that is extremely important in achieving accurate, controlled designs. In the first phase

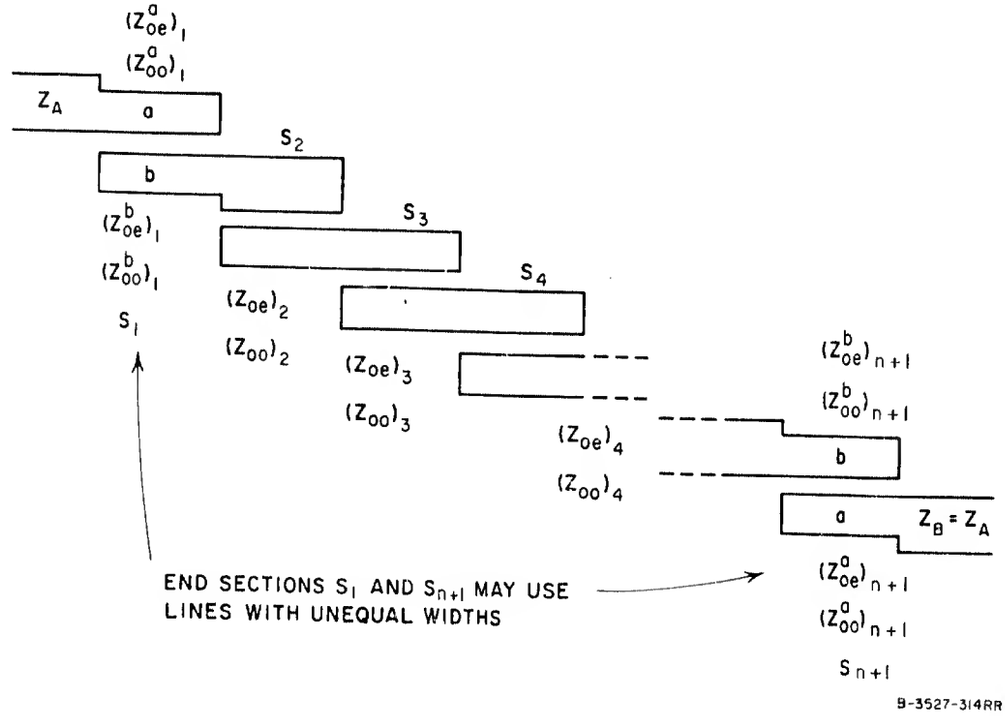

FIG. III-1 DIAGRAMMTIC FORM OF PARALLEL-COUPLED-RESONATOR BANDPASS FILTER.
(Each coupled section is a quarter wavelength at band center.)

of the design method, a lumped element, low-pass prototype filter is converted to an equivalent filter that uses ideal impedance inverters and reactive elements of one kind only. Next, the equivalent filter is divided into symmetrical sections, each of which is then characterized by its image parameters. The second phase of the design method is similarly to divide the parallel-coupled-resonator filter into symmetrical sections of quarter-wavelength coupled lines. This is easily done as is seen from the physical configuration in Fig. III-1. Next, the image impedance of a section of microwave filter and a corresponding section of the equivalent lumped element prototype filter are equated at two critical frequencies: band center and band edge. This is done for each section of the filter except the end sections, which are treated somewhat differently. Since the image impedance of each component section of the microwave filter and the prototype filter have been made equal at band center and band edge, it is expected that the responses of the filters will be very nearly the same at these frequencies. Also, one would not expect the responses to differ too greatly for frequencies

in between. In practice the method works quite satisfactorily in most cases.

In modifying the design equations for microstrip parallel-coupled-resonator band-pass filters, the same design philosophy was followed. Thus, the first step in the analysis was to examine the image parameters of a pair of parallel coupled quarter-wavelength lines in microstrip. The image impedance and phase for a pair of coupled microstrip lines were found by analysis to be

$$Z_I = z\left\{\frac{1}{2}(1 + k^2) - \frac{1}{2}(1 - k^2)(\cot\theta_o \cot\theta_e + \csc\theta_o \csc\theta_o)\right\}^{\frac{1}{2}} \qquad \text{(III-1)}$$

$$\gamma = \frac{1}{2} \ln\left\{\frac{C + Z_I/z}{C - Z_I/z}\right\} \quad , \qquad \text{(III-2)}$$

respectively.

The parameters in Eqs. (III-1), (III-2) are defined as follows:

Z_I = image impedance (III-3)

γ = image phase (III-4)

$$z = \frac{z_{oo} + z_{oe}}{2} \qquad \text{(III-5)}$$

z_{oo} = odd-mode impedance (III-6)

z_{oe} = even-mode impedance (III-7)

k = voltage coupling coefficient which is equal to

$$\frac{z_{oo} - z_{oe}}{z_{oo} + z_{oe}} \qquad \text{(III-8)}$$

θ_o = odd-mode phase variable (III-9)

θ_e = even-mode phase variable (III-10)

$$C = -i\left\{\frac{(1+k)}{2}\cot\theta_e + \frac{(1-k)}{2}\cot\theta_o\right\} \qquad \text{(III-11)}$$

$$i = \sqrt{-1} \quad . \qquad \text{(III-12)}$$

It was convenient to eliminate the even-mode phase variable from Eq. (III-1). To do this α was defined as the ratio of even- to odd-mode phase,

$$\alpha = \theta_e/\theta_o \quad . \qquad \text{(III-13)}$$

Then Eq. (III-1) may be rewritten as

$$Z_1 = z\left\{\frac{1}{2}(1+k^2) - \frac{1}{2}(1-k^2)(\cot\theta\cot\alpha\theta + \csc\theta\csc\alpha\theta)\right\}^{\frac{1}{2}} \quad . \qquad \text{(III-14)}$$

Note that the notation was further simplified by dropping the subscript "o" from the odd-mode phase variable. (In all subsequent discussion and on the graphical data, the variable θ is to be understood as θ_o.)

The image bandwidth of two coupled microstrip lines was determined by solving Eq. (III-5) for θ with Z_I set equal to 0. This was done for several values of α between 0.8 and 1.0. Let the two lowest solutions be denoted as θ_1 and θ_2. Then the fractional bandwidth is given by

$$w = 2\left[\frac{\theta_2 - \theta_1}{\theta_2 + \theta_1}\right] \quad . \qquad \text{(III-15)}$$

The fractional bandwidth versus coupling in dB (i.e., $-20\log_{10} k$) is shown in Fig. III-2. Only two curves for $\alpha = 0.8$ and 1.0 are given since intermediate values of α give curves lying between those shown. The important result that emerges from the data is that for microstrip the image bandwidth is virtually independent of the ratio of even- to odd-mode propagation velocities, at least for ratios down to 0.8.

A second set of useful data is the shift of the center of the image pass band from 90 degrees. The center of the image pass band, denoted by θ_c, is determined by the formula

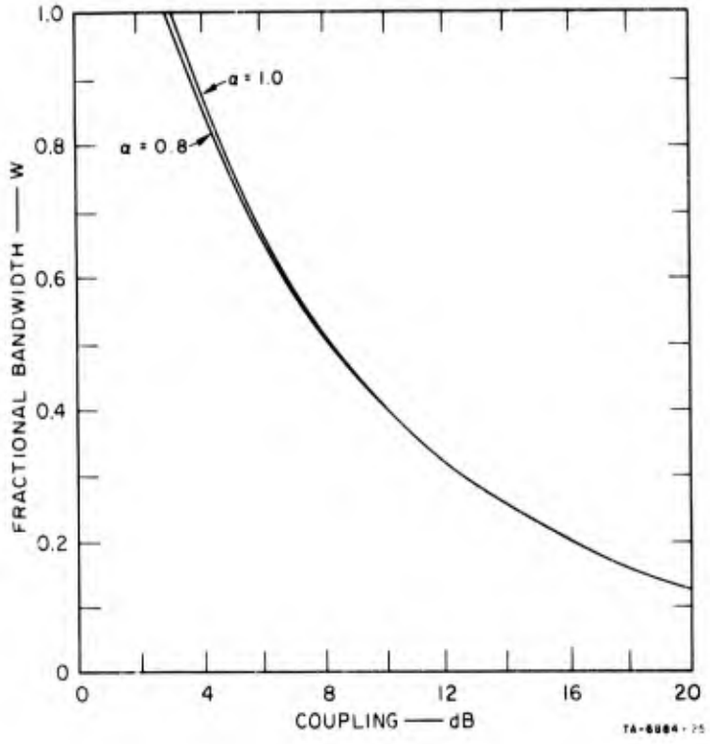

FIG. III-2 FRACTIONAL BANDWIDTH FOR MICROSTRIP COUPLED LINES ($\alpha = \theta_e/\theta_o$)

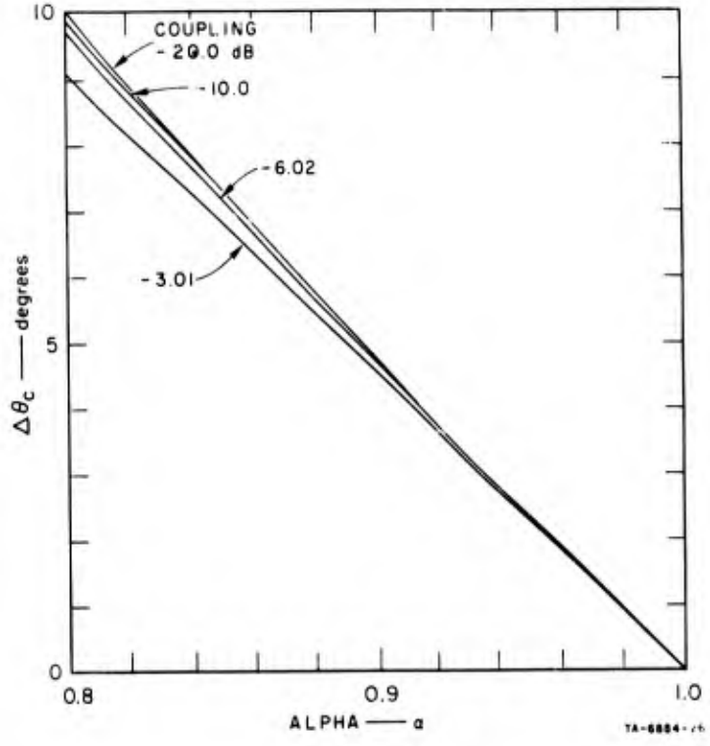

FIG. III-3 CENTER FREQUENCY SHIFT OF IMAGE PASS BAND FOR COUPLED MICROSTRIP LINES

$$\theta_c = \frac{\theta_2 + \theta_1}{2} \quad .$$

The shift from 90 degrees, denoted by $\Delta\theta_c$, is given in Fig. III-3 with α as abscissa and coupling as a parameter. It is seen to be very nearly linear over the range of α tested and is only weakly dependent on coupling. A good approximation to the curves of Fig. III-3 is

$$\Delta\theta_c = 48(1.0 - \alpha) \text{ degrees} \quad . \qquad \text{(III-16)}$$

The approximation has a maximum error of 4 5 percent at $\alpha = 0.8$. For narrow-band filters, for which the couplings are usually less than -6.02 dB, a slightly better approximation is

$$\Delta\theta_c = 49(1.0 - \alpha) \quad .$$

Other calculations of image impedance for various values of coupling and α showed that the peak normalized image impedances, $Z_I/(zk)$, occur at or very near θ_c and are virtually unity. Thus, $Z_I/(zk)$ is also independent of α.

C. Modification of the Design Equations

The data given in Sec. III-B indicated that several modifications of the parallel-coupled-resonator filter equations[2] should be made. [These equations (without modifications) are given in Table II for convenience.] Those equations independent of α were modified.

An examination of the derivation of the design equations showed that the parameters K_k/Z_A given by*

$$K_k/Z_A = \frac{1}{\omega_1' \sqrt{g_k g_{k-1}}} \quad \text{or} \quad \frac{1}{\sqrt{\omega_1' \, g_k g_{k-1}}}$$

*The parameters g_k and ω_1' are the element values and radian cutoff frequency of the low-pass prototype filters. See Ref. 2 for details.

Table II

MATTHAEI'S DESIGN EQUATIONS FOR PARALLEL-COUPLED FILTERS

End Sections 1 and n + 1

For k = 1 and k = n + 1 compute:

$$\frac{K_k}{Z_A} = \frac{1}{\sqrt{g_k g_{k-1}}\,\omega_1'} \quad , \quad \left(Z^a_{oe}\right)_k = Z_A\left(\frac{K_k}{Z_A}\sqrt{h} + 1\right)$$

$$\left(Z^a_{oo}\right)_k = 2Z_A - \left(Z^a_{oe}\right)_k \quad , \quad \theta_1 = \frac{\pi\omega_1}{2\omega_0} = \frac{\pi}{2}\left(1 - \frac{w}{2}\right)$$

$$\left(Z^b_{oo}\right)_k = \left(Z^a_{oo}\right)_k + hZ_A\left[\frac{\tan\theta_1}{2} + \left(\frac{K_k}{Z_A}\right)^2\right] - Z_A$$

$$\left(Z^b_{oe}\right)_k = \left(Z^b_{oo}\right)_k + \left(Z^a_{oe}\right)_k - \left(Z^a_{oo}\right)_k$$

The parameter h is a dimensionless scale factor which may be chosen arbitrarily so as to give a convenient admittance level in the filter (see Ref. 2).

Interior Sections 2 to n

For k = 2 to k = n compute:

$$\frac{K_k}{Z_A} = \frac{1}{\omega_1'\sqrt{g_k g_{k-1}}} \quad , \quad N_k = \sqrt{\left(\frac{K_k}{Z_A}\right)^2 + \frac{\tan^2\theta_1}{4}}$$

$$\left(Z_{oe}\right)_k = hZ_A\left(N_k + \frac{K_k}{Z_A}\right)$$

$$\left(Z_{oo}\right)_k = hZ_A\left(N_k - \frac{K_k}{Z_A}\right)$$

were obtained by equating appropriate image impedances of the prototype filter and microwave filter at band center. Since the image admittance of coupled microstrip lines was found to be independent of α, these equations required no modifications.

On the other hand, the parameters N_k are functions of α. They are given in Table III as

$$N_k = \sqrt{(K_k/Z_A)^2 + \frac{(\tan \theta_1)^2}{4}} \quad . \tag{III-17}$$

They arose by equating image impedances at band edge. In homogeneous media the band-edge phase in radians is given by

$$\theta_1 = \frac{\pi}{2}\left(1 - \frac{w}{2}\right) \quad , \tag{III-18}$$

the $\pi/2$ factor occurring because band center happens for $\theta = \pi/2$. However, in microstrip media band center is shifted by an amount $\Delta\theta$ which is proportional to α. Specifically,

$$\theta_c = \frac{\pi}{2} + \Delta\theta \quad ,$$

or via Eq. (III-16) converted to radians,

$$\theta_c = \frac{\pi}{2} + 0.838\ (1 - \alpha) \quad . \tag{III-19}$$

Hence, θ_1 for microstrip is

$$\theta_1 = \theta_c\left[1 - \frac{w}{2}\right] = \left\{\frac{\pi}{2} + 0.838\ (1 - \alpha)\right\}\left\{1 - \frac{w}{2}\right\} \quad . \tag{III-20}$$

In addition to this modification a second one was called for. The function $\tan \theta_1$, which appears in the design equations of Table III, occurs as a result of its implicit representation in Eq. (III-14) for $\alpha = 1$. To see this, note that the trigonometric part of Eq. (III-14) is equal to $1 + 2\cot^2 \theta$ for $\alpha = 1$. Thus, Eq. (III-14) could also be written as

$$Z_1 = z \left\{ k^2 - (1 - k^2) \cot^2 \theta \right\}^{\frac{1}{2}} ,$$

which makes the presence of the tan θ dependence quite evident. When image impedances are equated at band edge, it is clear that the results will have a tan θ_1 dependence.

In the microstrip case the function

$$F(\alpha,\theta) = \cot\theta \cot\alpha\theta + \csc\theta \csc\alpha\theta \qquad \text{(III-21)}$$

plays the role of $1 + 2\cot^2\theta$. By straightforward trigonometric manipulation it is easily proved that

$$\tan\theta = \sqrt{\frac{2}{F(1,\theta) - 1}} \quad . \qquad \text{(III-22)}$$

This suggests that in microstrip tan θ_1 in Table III should be replaced by

$$\tan\theta_1 = \sqrt{\frac{2}{F(\alpha_1\theta_1) - 1}} \quad . \qquad \text{(III-23)}$$

Note that this substitution reduces to the correct value for designs in homogeneous media.*

In summary, then, there are two modifications to the design equations of Table III:

(1) $\theta_1 = \left[\frac{\pi}{2} + 0.838\,(1 - \alpha)\right]\left[1 - \frac{w}{2}\right]$

(2) tan θ_1 is to be replaced by

$$\sqrt{\frac{2}{F(\alpha,\theta_1) - 1}}$$

with $F(\alpha,\theta) = \cot\theta \cot\alpha\theta + \csc\theta \csc\alpha\theta$.

---

*That Eq. (III-23) is the proper modification can also be shown by a more lengthy derivation, but this will not be done here.

In order to examine the effects of the modified design equations on the filter responses, a computer program was written to design filters with arbitrary α and to compute the frequency response. Several representative cases are described in the following paragraphs. Figures III-4 through III-8 present VSWR responses of filters all of whose designs are based on a lumped element prototype filter having the following specifications:

N = number of resonators = 5

VSWR = 1.2 Chebyshev ripple

w = fractional bandwidth = 0.20.

The first response is shown in Fig. III-4 for the case $\alpha = 1.0$. It is given for the purpose of comparisons with later examples. The response is seen to be virtually ideal, exhibiting near perfect equal ripple response, and having a fractional bandwidth of 0.20.

1. Example Design C-1 ($\alpha = 0.95$)

Figure III-5 gives the VSWR response for the same filter but designed for $\alpha = 0.95$. (Remember that the abscissa variable θ is the odd-mode phase variable.) Note that the lower band edge has shifted from 81 to 83.3 degrees, and the upper band edge has shifted from 99 to 101.3 degrees. The center of the band is the arithmetic mean of the band edges, which calculates to

$$\theta_c = 92.4 \text{ degrees} \quad .$$

The shift from 90 degrees is thus 2.4 degrees. It is interesting to compare this with the shift predicted by Eq. (III-16). This value is $\Delta\theta_c = 48\ (1 - \alpha) = 48\ (1 - 0.95) = 2.4$ degrees. The agreement is excellent in this case.

The fractional bandwidth, given by Eq. (III-15), calculates to

$$w = 0.195 \quad ,$$

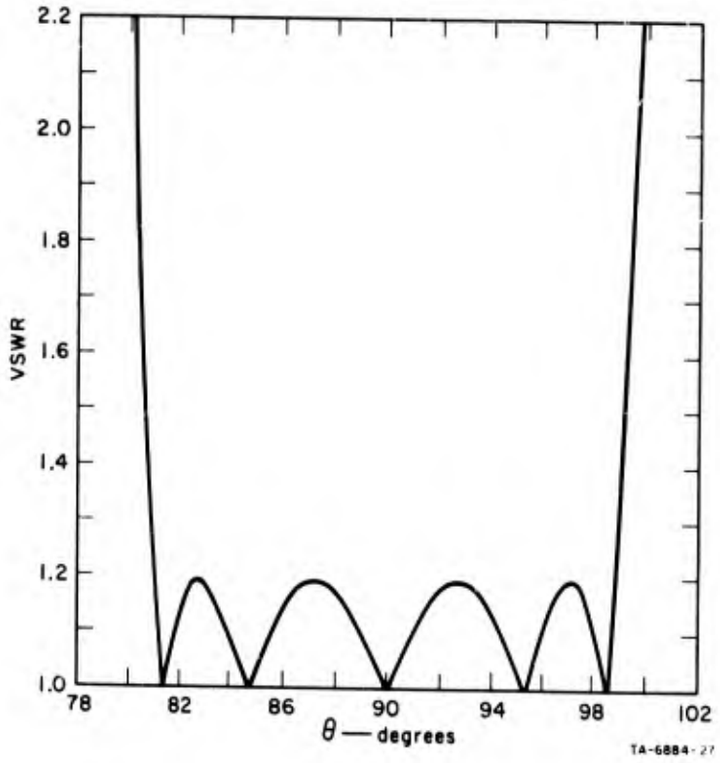

FIG. III-4 VSWR RESPONSE OF EXAMPLE DESIGN C-1 USING MODIFIED DESIGN EQUATIONS ($\alpha = 1.0$)

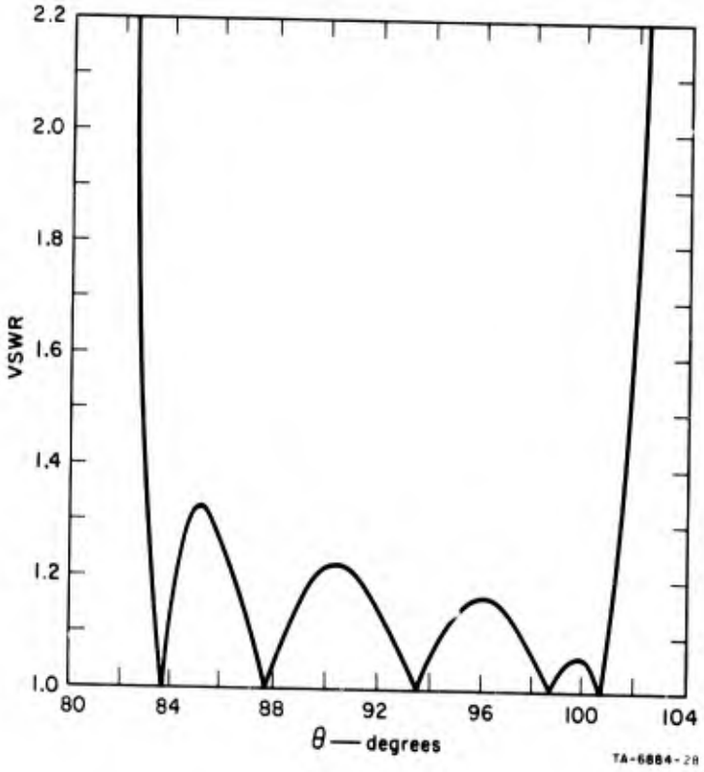

FIG. III-5 VSWR RESPONSE OF EXAMPLE DESIGN C-1 USING MODIFIED DESIGN EQUATIONS ($\alpha = 0.95$)

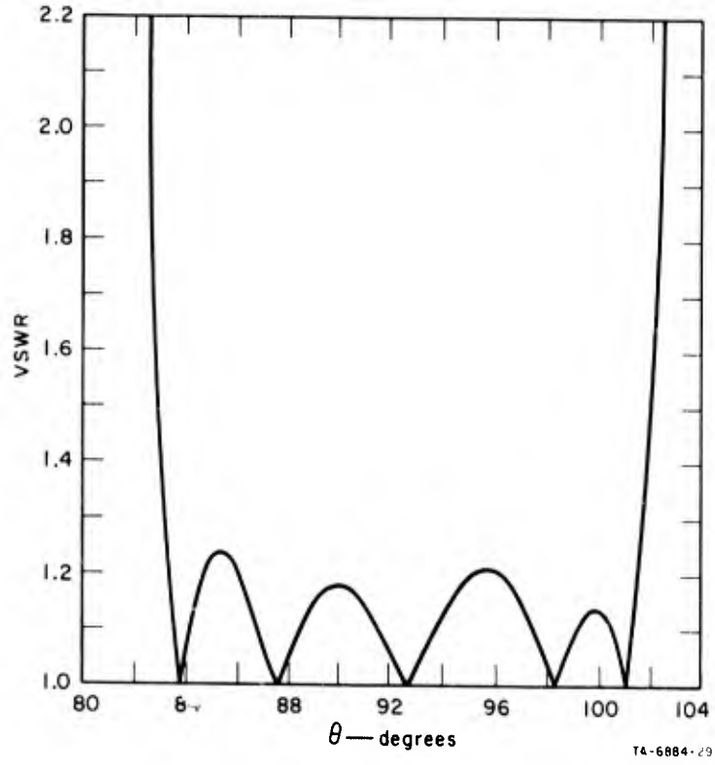

FIG. III-6 VSWR RESPONSE OF EXAMPLE DESIGN C-1 USING MODIFIED DESIGN EQUATIONS WITH THE FIRST AND LAST COUPLED SECTIONS LENGTHENED BY 1 PERCENT ($\alpha = 0.95$)

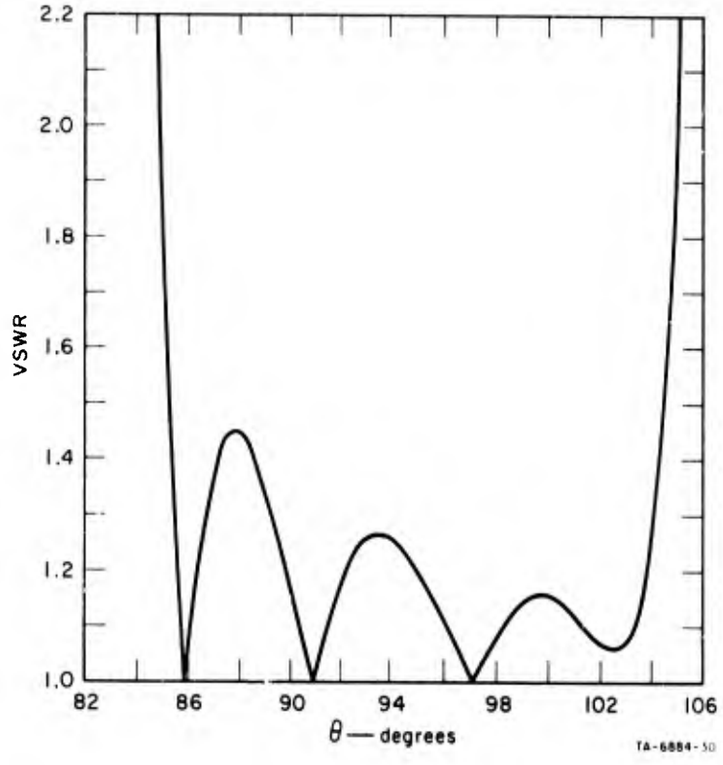

FIG. III-7 VSWR RESPONSE OF EXAMPLE DESIGN C-2 USING MODIFIED DESIGN EQUATIONS ($\alpha = 0.90$)

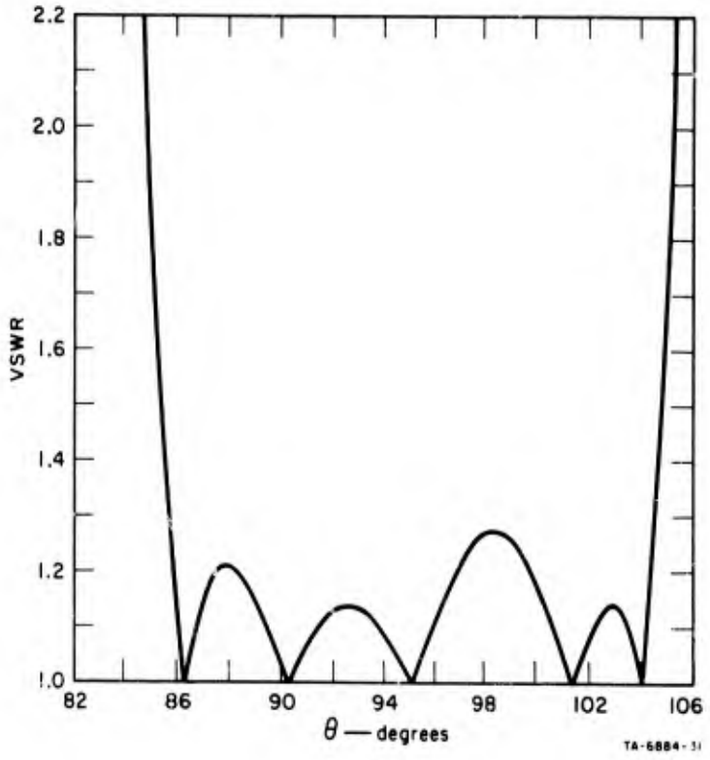

FIG. III-8 VSWR RESPONSE OF EXAMPLE DESIGN C-2 USING MODIFIED DESIGN EQUATIONS WITH THE FIRST AND LAST SECTIONS LENGTHENED BY 3 PERCENT (α = 0.90)

which is slightly smaller than the design specification, although not a serious shrinkage. The most serious degradation of the filter performance is the excessive peak ripple at the low end of the pass band and the ripple skewness throughout the band. This result is caused by the asymmetry of the image impedance as a function of θ, which is, itself, a direct consequence of the asymmetry of the function F (α,θ) defined in Eq. (III-21). For although the image cutoff frequencies are located symmetrically with respect to the center of the pass band, the remainder of the function F (α,θ) is only approximately symmetrical about band center.

A close examination of the input impedance of the filter revealed that the main effect of the asymmetry of F (α,θ) was to cause a small reactive component within the pass band. Fortunately, this reactance can be approximately cancelled by lengthening the first and last coupled pairs of lines by a small fraction. The amount of lengthening was determined experimentally.

Figure III-6 gives the response of the identical filter design, except that the first and last sections were lengthened by 1 percent. The VSWR is greatly improved over the previous design, and although not ideally equal ripple it would probably be acceptable in most applications. The fractional bandwidth was recalculated for this design and found to be equal to the previous case.

2. Example Design C-2 ($\alpha = 0.90$)

The response of a second filter design, having $\alpha = 0.90$, is illustrated in Figs. III-7 and III-8. Figure III-7 is the case for which the end sections are equal in length to all of the other sections. As might be expected the VSWR is much more distorted than for the previous example which had $\alpha = 0.95$. The bandwidth, measured between points of 1.2 VSWR, was calculated to be 0.193, which is virtually the same as in the previous example.

To improve the pass-band response, the end sections were lengthened by small amounts and the responses computed for each case. The result shown in Fig. III-8 is for the case in which the end sections were lengthened 3 percent. If the end sections were reduced slightly from 3 percent to say 2.8 percent, the ripple centered at 88 degrees would increase slightly, while the one at 99 degrees would decrease slightly. Therefore a lengthening of the end sections of between 2.5 to 3 percent probably would be optimum. However, here again, the response given in Fig. III-8 is likely to be acceptable in most practical applications.

The fractional bandwidth was recalculated for this case and found equal to 0.194, which is essentially the same as the example design of Fig. III-7. The shift in the center frequency was calculated from the data and found equal to 5.15 degrees. The predicted value is 48 (1 - 0.9) = 4.8 degrees, which differs by only 0.35 degrees from the measured value. Thus, it appears so far that the shift of the center of the band is very well approximated by Eq. (III-15).

The question arises, for a given prototype filter, how does varying α affect the coupling of individual coupled sections? Examination

of the design data for the three previous cases showed that in all sections of the filters coupling was decreased when α was made smaller.

Wide-band designs were also investigated on the computer. Figures III-9 through III-12 present VSWR responses of filters all of whose designs were based on a lumped element prototype filter having these specifications:

$N = 9$

VSWR = 1.2 Chebyshev ripple

$w = 0.6667.$

The first response for the wideband case is shown in Fig. III-9 for $\alpha = 1.0$. It is given for purposes of comparisons with later examples. The VSWR is seen to be within specifications over most of the pass band, but rises to 1.64 near the band edges. This is a consequence of the approximate design procedure. The fractional bandwidth, being equal to 0.659, is slightly less than the specification.

3. Example Design C-3 ($\alpha = 0.95$)

Figure III-10 gives the corresponding response for the same filter with $\alpha = 0.95$. The same qualitative effects as seen in the previous examples are apparent in this example: The center of the band is shifted from 90 degrees; the VSWR is somewhat degraded and tilted across the pass band. Again, by lengthening the end sections, it was possible to improve the response considerably. Figure III-11 gives the corresponding VSWR for the same filter design except that the end sections are 3 percent longer than the other sections. It is seen that the response is now very close to that given in Fig. III-9, except for the shifted center, which was calculated from the data to be 2.5 degrees. The predicted value is 2.4 degrees so that again there is very good agreement.

The fractional bandwidth was calculated from the data and found equal to 0.660. This is slightly less than the design bandwidth, but is in keeping with the result obtained from the original design equations for $\alpha = 1.0$.

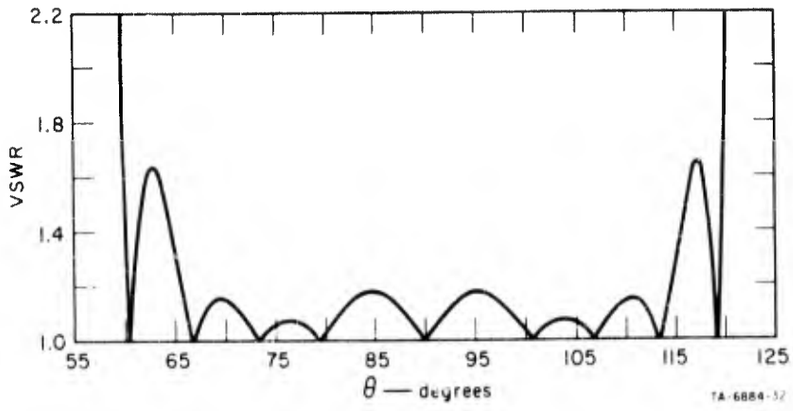

FIG. III-9 VSWR RESPONSE OF EXAMPLE DESIGN C-3 USING MODIFIED DESIGN EQUATIONS (α = 1.0)

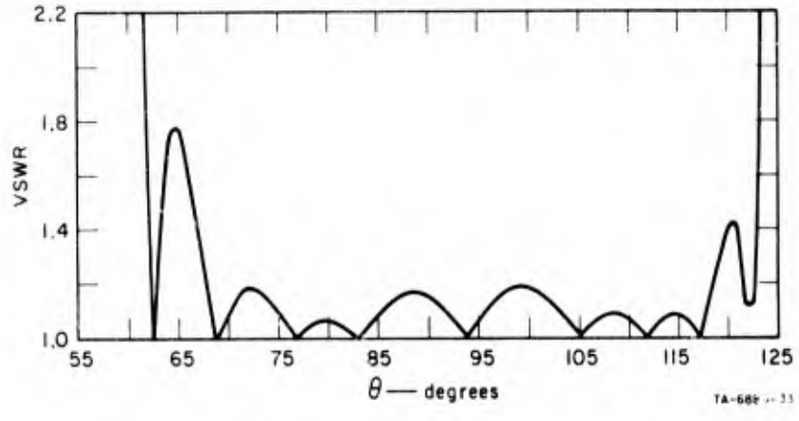

FIG. III-10 VSWR RESPONSE OF THIRD EXAMPLE DESIGN C-3 USING MODIFIED DESIGN EQUATIONS (α = 0.95)

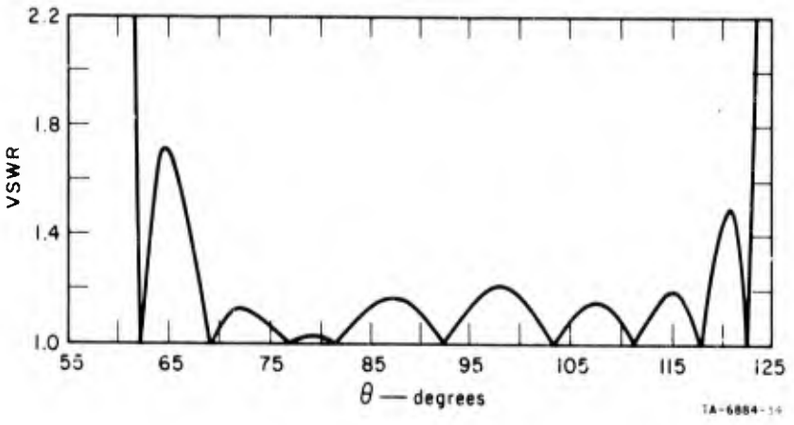

FIG. III-11 VSWR RESPONSE OF EXAMPLE DESIGN C-3 USING MODIFIED DESIGN EQUATIONS WITH THE FIRST AND LAST SECTIONS LENGTHENED BY 3 PERCENT (α = 0.95)

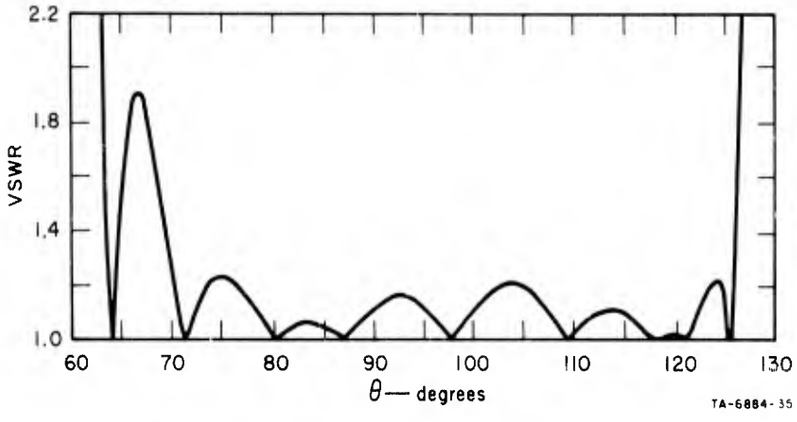

FIG. III-12 VSWR RESPONSE OF EXAMPLE DESIGN C-4 USING MODIFIED EQUATIONS (α = 0.90)

4. Example Design C-4 (α = 0.90)

The VSWR response for this design is given in Fig. III-12. The end sections were not altered from their nominal value. As before, the VSWR was slightly degraded, although in this case there was less tilting of the response than in previous cases. The peak ripple at the low end of the pass band increased from 1.64 to 1.9, while at the high end the peak ripple decreased from 1.64 to 1.24. Throughout the rest of the band the VSWR did not change significantly.

In this example it was found that lengthening the end sections improved the response only slightly. For example, lengthening the end sections by 2 percent reduced the peak VSWR at the low end of the band to 1.85; lengthening them by 5 percent reduced the peak VSWR to only 1.80, while at the same time it raised the VSWR peaks in the middle of the band above the design goal of 1.2. Thus, a lengthening of the end sections by about 2 to 3 percent is probably optimum, although this would improve the overall response only a little.

D. Alternate Design Equations

Although the modifications to the design equations presented in Sec. III-C were successful in achieving practical, controlled designs, it was thought useful to seek an alternate approach in hopes of obtaining still better results. In the method of Sec. III-C the technique of equating image impedance at two critical frequencies was employed. Image phase was ignored. In the alternate approach described in this section, image impedance is equated at the lower band edge, and image phase is equated at the upper band edge. Note that in this method, in addition to using image phase, the critical points for equating image phase and impedance are the band edges in contrast to one band edge and band center in the previous method. It was felt that this might give more precise control over the fractional bandwidth. The alternate design equations are presented in Table III. The final parameters are the same as those in Table II (i.e., even- and odd-mode admittances) so that further explanations are not required. To examine and compare the responses of filters designed from the alternate equations, the same designs presented previously are repeated in the following examples.

Table III

ALTERNATE DESIGN EQUATIONS FOR PARALLEL-COUPLED FILTERS

End Sections 1 and n + 1

For k = 1 and k = n + 1 compute:

$$\frac{K_k}{Z_A} = \frac{1}{\sqrt{g_k g_{k-1}}\,\omega_1'} \quad , \quad \left(Z^a_{oe}\right)_k = Z_A\left(\frac{K_k}{Z_A}\sqrt{h} + 1\right)$$

$$\theta_1 = \frac{\pi}{2}\left\{1 + 0.53333\,(1 - \alpha)\right\}\left\{1 - \frac{w}{2}\right\}$$

$$\left(Z^a_{oo}\right)_k = 2Z_A - \left(Z^a_{oe}\right)_k \quad ; \quad \theta_1 = \frac{\pi\omega_1}{2\omega_0} = \frac{\pi}{2}\left(1 + \frac{w}{2}\right)$$

$$\left(Z^b_{oo}\right)_k = \left(Z^a_{oo}\right)_k + hZ_A\left[\frac{\tan\theta_1}{2} + \left(\frac{K_k}{Z_A}\right)^2\right] - Z_A$$

$$\left(Z^b_{oe}\right)_k = \left(Z^b_{oo}\right)_k + \left(Z^a_{oe}\right)_k - \left(Z^a_{oo}\right)_k$$

The parameter h is a dimensionless scale factor which may be chosen arbitrarily so as to give a convenient admittance level in the filter (Ref. 2).

Interior Sections 2 to n

For k = 2, to n, compute

$$\theta_2 = \frac{\pi}{2}\left[1 + 0.5333\,(1 - \alpha)\right]\left[1 + \frac{w}{2}\right]$$

$$C = \sin\theta_2$$

$$D = \sin\alpha\theta_2$$

$$A = \left|C\cos\alpha\theta_2\right|$$

$$B = \left|D\cos\alpha\theta_2\right|$$

$$G = \frac{1}{2}\sqrt{g_k g_{k-1}}$$

$$\mathcal{K} = \frac{GD - B}{GC + A}$$

$$\theta_1 = \frac{\pi}{2}\left[1 + 0.5333\,(1 - \alpha)\right]\left[1 - \frac{w}{2}\right]$$

$$T = \cot\theta_1\cot\alpha\theta_1 + \csc\theta_1\csc\alpha\theta_1$$

$$k = \frac{1 - \mathcal{K}}{1 + \mathcal{K}}$$

$$\Sigma = \frac{h\sqrt{1 - G^2}}{G\left[\sqrt{\frac{1 + k^2}{2} - \frac{1 - k^2}{2}T}\right]}$$

$$Z_{oo_k} = \frac{\Sigma}{1 + \mathcal{K}} \qquad Z_{oe_k} = \mathcal{K}Z_{oo_k}$$

Figures III-13 through III-17 are VSWR responses of filters all of whose designs are based on the lumped element prototype of five resonators having the same specifications as before: w = 0.20, VSWR = 1.2 Chebyshev ripple. Figure III-13 is the response for α = 1.0, presented for purposes of later comparisons. It is interesting to compare the graphs of Fig. III-13 and Fig. III-4. The only distinct difference is that in the response of Fig. III-13 the ripple peaks near the center of the band are slightly less than the corresponding peaks of the response of Fig. III-4. The fractional bandwidth is exactly 0.20 as is the corresponding case given in Fig. III-4.

1. Example Design D-1 (α = 0.95)

The VSWR response shown in Fig. III-14 is for the case α = 0.95. It is clearly degraded from that shown in Fig. III-13, although on closer examination it is seen to meet all specifications except for the VSWR peak at θ = 85 degrees. It differs also in that there are only four points of match in the pass band as compared to five in the previous figure. This is not totally unexpected, however, since the alternate design equations concentrate on the band edges and ignore the center of the band, where the fifth point of match is now eliminated. The fractional bandwidth was determined to be 0.206, which is quite satisfactory. The shift of the center of the band was determined to be 2.3 degrees, which compares well with a predicted value of 2.4 degrees.

As was the case for filters designed from the modified design equations of Sec. III-C, it was also found with the alternate equations that the VSWR response could be significantly improved in many cases by lengthening the end sections by a small fraction. Figure III-15 gives the response of the identical design above, but with the end sections lengthened by 1.5 percent. The VSWR peak that occurred at 85 degrees is now 1.2, and the remainder of the response also meets the specifications, for all practical purposes. The fifth point of match is not restored in this example, but this is not absolutely essential in meeting the design goals. In any case the effect of finite loss in the system would obliterate the points of match in all cases.

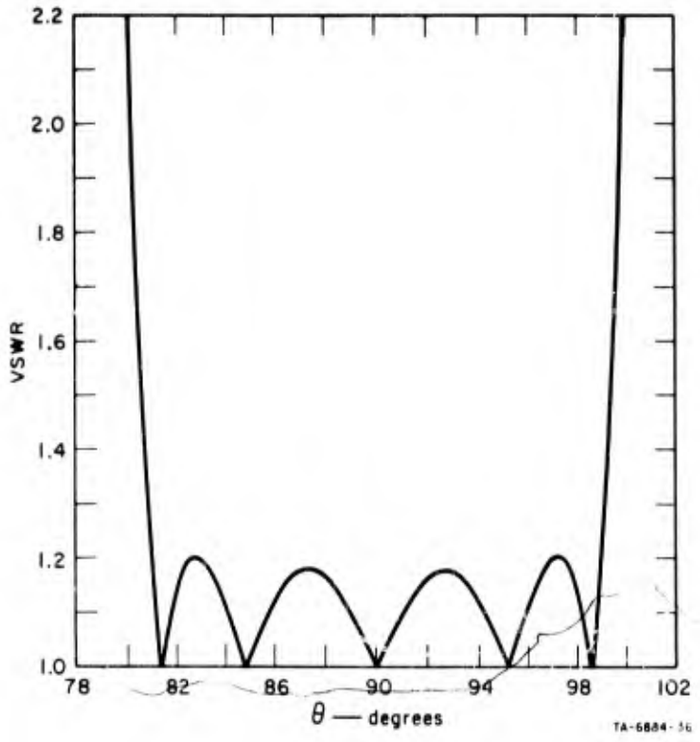

FIG. III-13 VSWR RESPONSE OF EXAMPLE DESIGN D-1 USING ALTERNATE DESIGN EQUATIONS (α = 1.0)

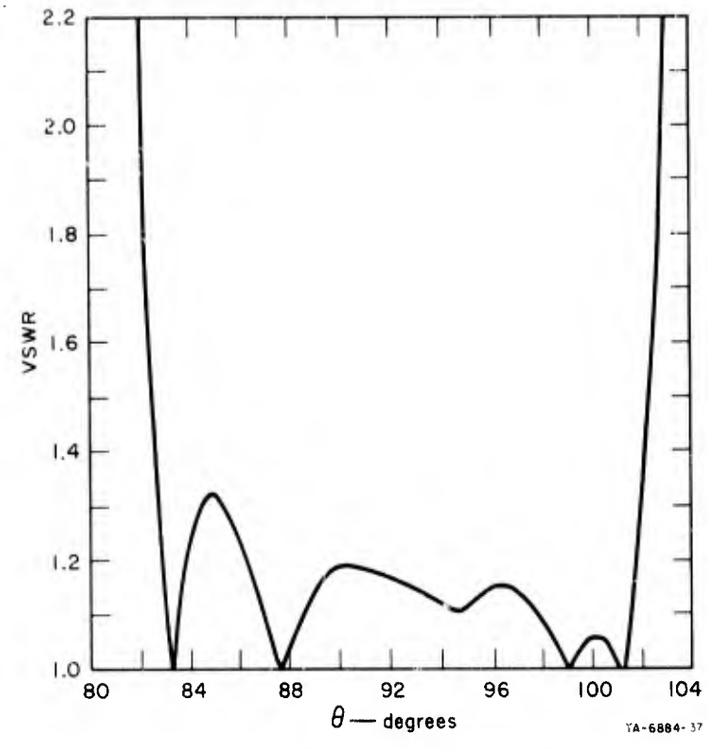

FIG. III-14 VSWR RESPONSE OF EXAMPLE DESIGN D-1 USING ALTERNATE DESIGN EQUATIONS (α = 0.95)

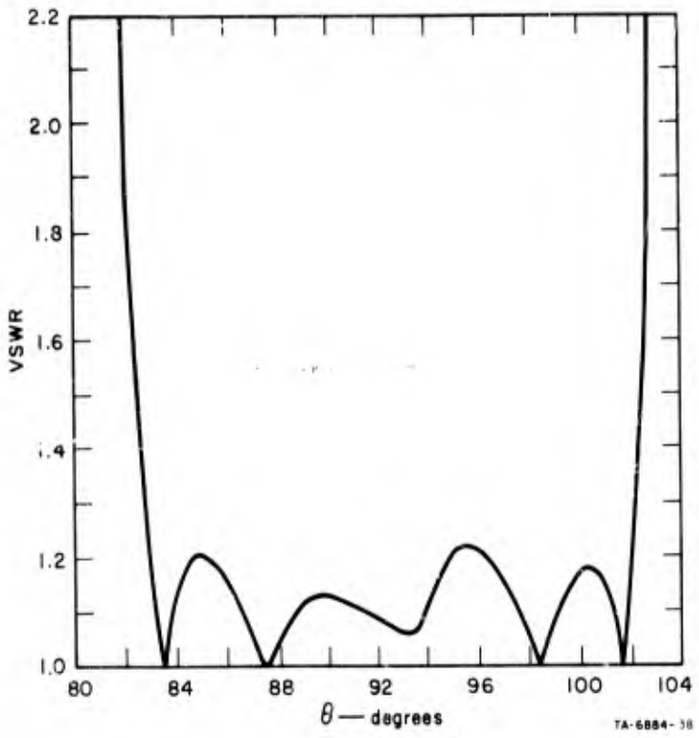

FIG. III-15 VSWR RESPONSE OF EXAMPLE DESIGN D-1 USING ALTERNATE DESIGN EQUATIONS WITH THE FIRST AND LAST SECTIONS LENGTHENED BY 1.5 PERCENT (α = 0.95)

2. Example Design D-2 (α = 0.90)

The response of the same design except that α = 0.90 is shown in Fig. III-16. As is expected the VSWR is somewhat more degraded than in the previous case. Three points of match are eliminated in this example, although the fractional bandwidth, calculated to be 0.209, is still very close to the design value.

Figure III-17 shows the corresponding response for the same filter except that the end sections are lengthened by 3 percent. Although the VSWR exceeds 1.2 in two places, it is only by a small amount. The points of match are seen to be restored except at the upper band edge. The fractional bandwidth was determined to be 0.211, which exceeds the design bandwidth by slightly more than 5 percent. The shift in the center of the band is 5.15 degrees, which is to be compared with a predicted value of 4.8 degrees.

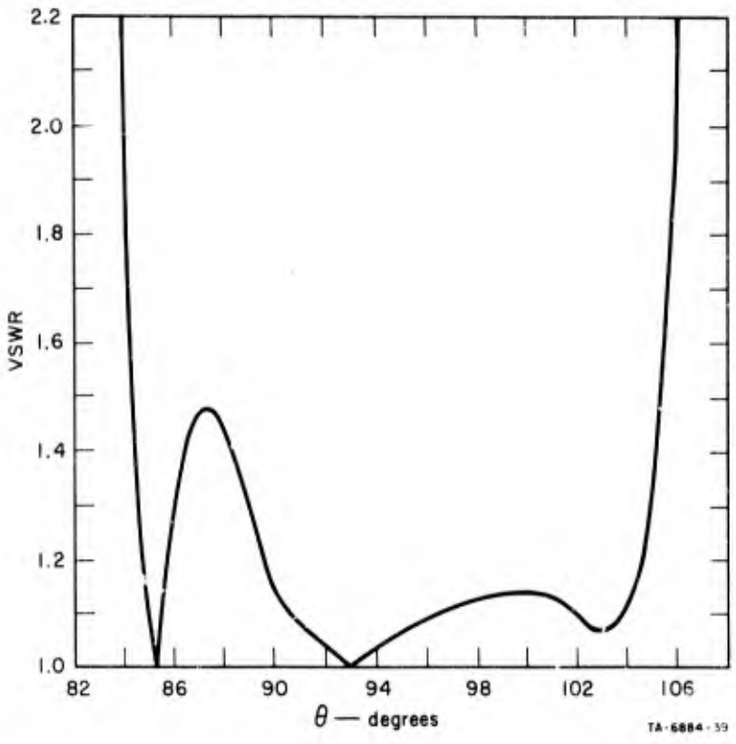

FIG. III-16 VSWR RESPONSE OF EXAMPLE DESIGN D-2 USING ALTERNATE EQUATIONS (α = 0.90)

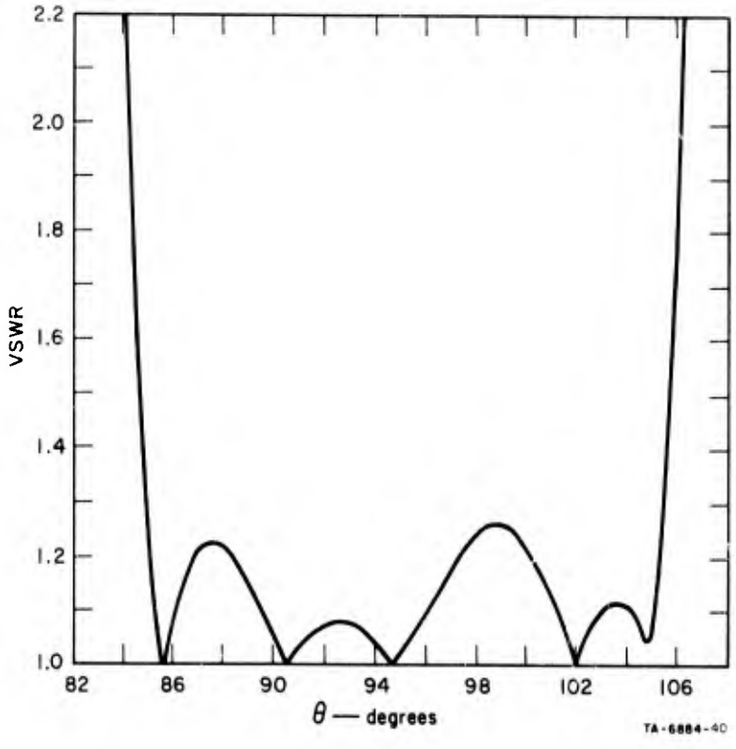

FIG. III-17 VSWR RESPONSE OF EXAMPLE DESIGN D-2 USING ALTERNATE DESIGN EQUATIONS WITH THE FIRST AND LAST SECTIONS LENGTHENED BY 3 PERCENT (α = 0.90)

Based on the previous results the alternate design equations, while satisfactory, do not appear superior to the modified equation. However, the following examples indicate that the alternate design equations are somewhat superior for wide-band designs, particularly for α values near or equal 1.0. Figure III-18 gives the response of a filter, with $\alpha = 1.0$, based on a lumped element prototype having the specifications:

N = 9

VSWR = 1.2 Chebyshev ripple

w (of bandpass filter) = 0.6667.

The corresponding response for the same design using Matthaei's equations is given in Fig. III-11. In comparing the two cases it is seen that the design based on the alternate equations is superior in two respects:

(1) The VSWR is more nearly equal ripple about the design value, including the band edges.

(2) The band edges occur precisely at 60 and 120 degrees, as desired, giving a theoretical fractional bandwidth of 0.6667.

3. Example Design D-3 ($\alpha = 0.95$)

Figure III-19 gives the VSWR for a design having $\alpha = 0.95$ based on the alternate equations. Except for one ripple peak of 1.34, the pass-band response is judged very satisfactory, as is the fractional bandwidth, which was calculated to be 0.664. The shift in the center of the band is 1.75 degrees, which differs quite a bit from the predicted value of 2.4 degrees.

In the present case the response is quite satisfactory without lengthening the end sections. In fact, lengthening the end sections would tend to tilt the response upward from left to right, which would degrade it rather than improve it.

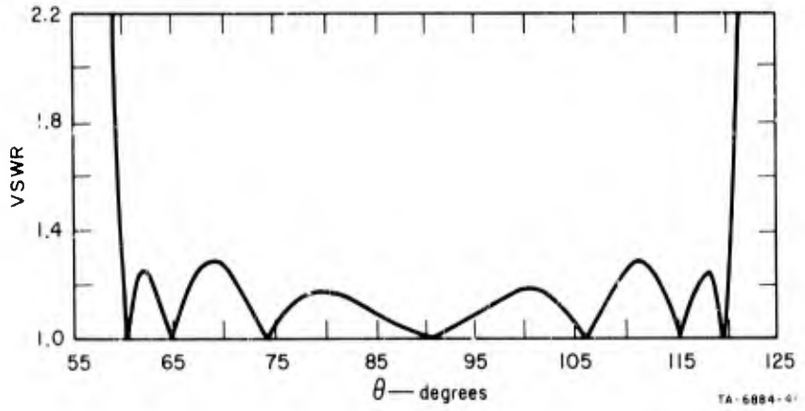

FIG. III-18 VSWR RESPONSE OF EXAMPLE DESIGN D-3 USING ALTERNATE DESIGN EQUATIONS (α = 1.0)

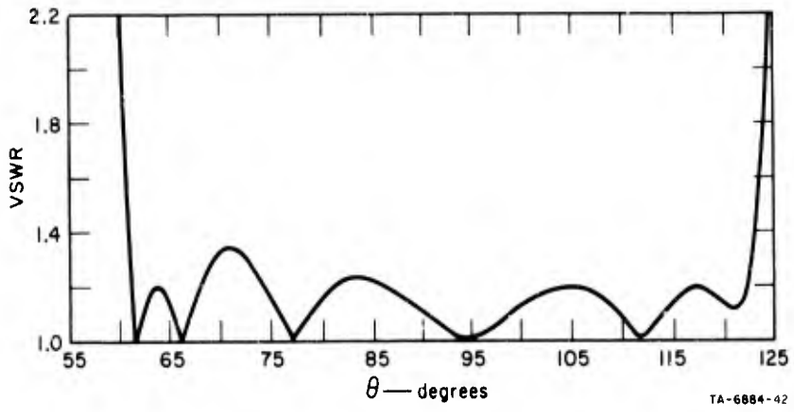

FIG. III-19 VSWR RESPONSE OF EXAMPLE DESIGN D-3 USING ALTERNATE DESIGN EQUATIONS (α = 0.95)

4. Example Design D-4 (α = 0.90)

The final example is the case of α = 0.90. The response for this design is shown in Fig. III-20. The fractional bandwidth and the shift in the center of the pass band are calculated to be 0.649 and 2.88 degrees, respectively. Thus, just as in the previous example the shift in the center of the band differs considerably from the predicted value given by formula Eq. (III-16). As in the previous examples, the peak ripples can be reduced slightly by lengthening the end sections a small amount in this case by approximately 2 percent.

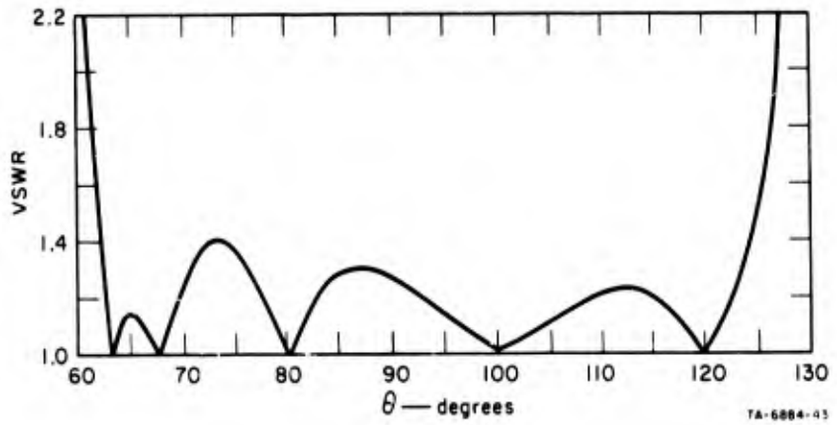

FIG. III-20 VSWR RESPONSE OF EXAMPLE DESIGN D-4 USING ALTERNATE DESIGN EQUATIONS (α = 0.90)

Comparison of the response of Fig. III-20 with the corresponding response of the Fig. III-12 shows the former to be slightly superior in achieving a more uniform ripple. However, the center of its pass band is not predictable by a simple analytical or graphical equation.

E. Microstrip Directional Couplers

In general, TEM transmission line directional couplers achieve their directional properties by the careful balancing (and resulting cancellation in one direction) of the magnetically and capacitively induced traveling waves in the coupled line. Naturally, the coupler response is degraded when the two induced waves travel at different

velocities since the required balance can not then be maintained. This is the case in microstrip couplers.

In order to quantitatively determine the amount of degradation, and thus determine the limitations on optimum coupler designs, the equations of Brenner[3] were used to obtain theoretical data on input VSWR, coupling, directivity, and phase difference between in-line and coupled waves. These data are presented in the following paragraphs. In the data, the same nomenclature is used as for the analyses of the parallel-coupled-resonator filters. The variable θ is the odd-mode phase variable; the symbol α is θ_e/θ_o.

One effect of a difference in the even- and odd-mode phase velocities is a shift of the location of the peak coupling from 90 degrees to $90 + \Delta\theta$ degrees. The amount of shift as a function of α is given by the data of Fig. III-21. The data show the shift to be virtually independent of coupling, at least for α greater than 0.80. A good analytic approximation to the curves in Fig. III-21 is the formula

$$\Delta\theta = 4.222 - 38.2\ (\alpha - 0.90) - 39.7\ (\alpha - 0.90)^2 \quad , \qquad \text{(III-24)}$$

which has a maximum error of only 0.082 degrees at $\alpha = 0.80$.

Not only is the location of the maximum displaced, but the maximum itself is diminished by an amount $-|\Delta C|$ - dB. If we define the nominal value of the coupler for $\alpha = 1.0$ as $-|C_0|$ - dB, and the maximum coupling achieved when $\alpha \neq 1.0$ as $-|C_{max}|$ - dB, then $-|C_{max}|$ - dB is given by

$$-|C_{max}| = -|C_0| - |\Delta C| - \text{dB} \quad . \qquad \text{(III-25)}$$

In Fig. III-22 the decrement $|\Delta C|$ - dB is given as a function of α for C_0 ranging from -3.01 to -20.0 dB. Values of C_0 less than -20.0 dB differed by less than 2.5 percent from the -20.0 dB curve. The data show that slightly greater coupling is required to achieve the design value in microstrip couplers. The precise amount can be obtained from the graph.

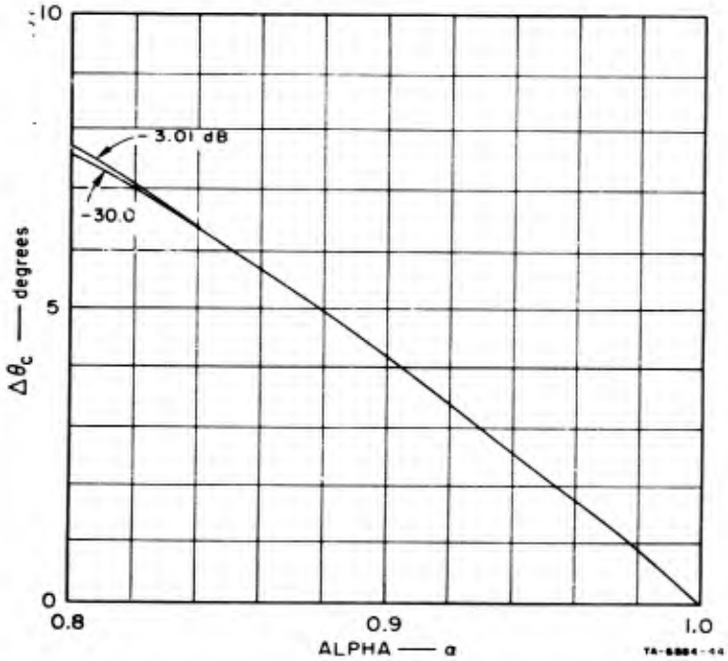

FIG. III-21 SHIFT IN THE LOCATION OF THE PEAK COUPLING FOR MICROSTRIP DIRECTIONAL COUPLERS

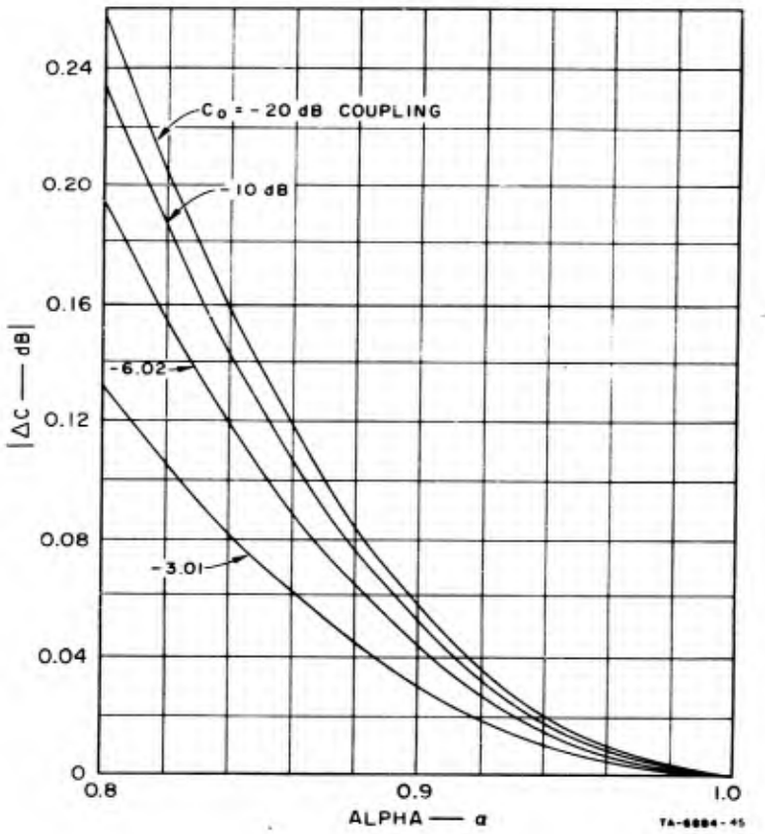

FIG. III-22 DECREASE IN PEAK COUPLING OF MICROSTRIP DIRECTIONAL COUPLERS

Figures III-23 to III-27 give data of theoretical maximum directivity as a function of θ for various values of α and coupling. Only values down to $\alpha = 0.90$ are plotted, since the directivity is extremely degraded below this value. The data show the directivity to be very sensitive to even extremely small differences in even- and odd-mode phase velocities. Naturally, the degradation is much worse for weak couplers, although it is here that the even- and odd-mode velocities will be very nearly the same. Brenner[3] showed that contributions to the directivity by differences in the phase velocities and perturbations from the correct values of the even- and odd-mode impedances are 90 degrees out of phase. Thus, the directivity cannot be improved by perturbing the even- and/or odd-mode impedance values. However, by designing a suitably small mismatch a proper distance from the coupled line region, it should be possible to improve the directivity considerably without seriously degrading the VSWR of the coupler.

REFERENCES

1. M. Saito, "Synthesis of Transmission Line Networks by Multivariable Techniques," Proc. Polytechnic Inst. of Brooklyn Symp. on Generalized Networks, pp. 353-392 (April 1966).

2. G. L. Matthaei, L. Young, and E. M. T. Jones, Design of Microwave Filters, Impedance Matching Networks, and Coupling Structures, Chap. 10 (McGraw-Hill Book Co., New York, 1964).

3. H. E. Brenner, "Perturbations of the Critical Parameters of Quarter Wave Directional Couplers," IEEE Trans. on Microwave Theory and Techniques, Vol. MTT-15, pp. 384-385 (June 1967).

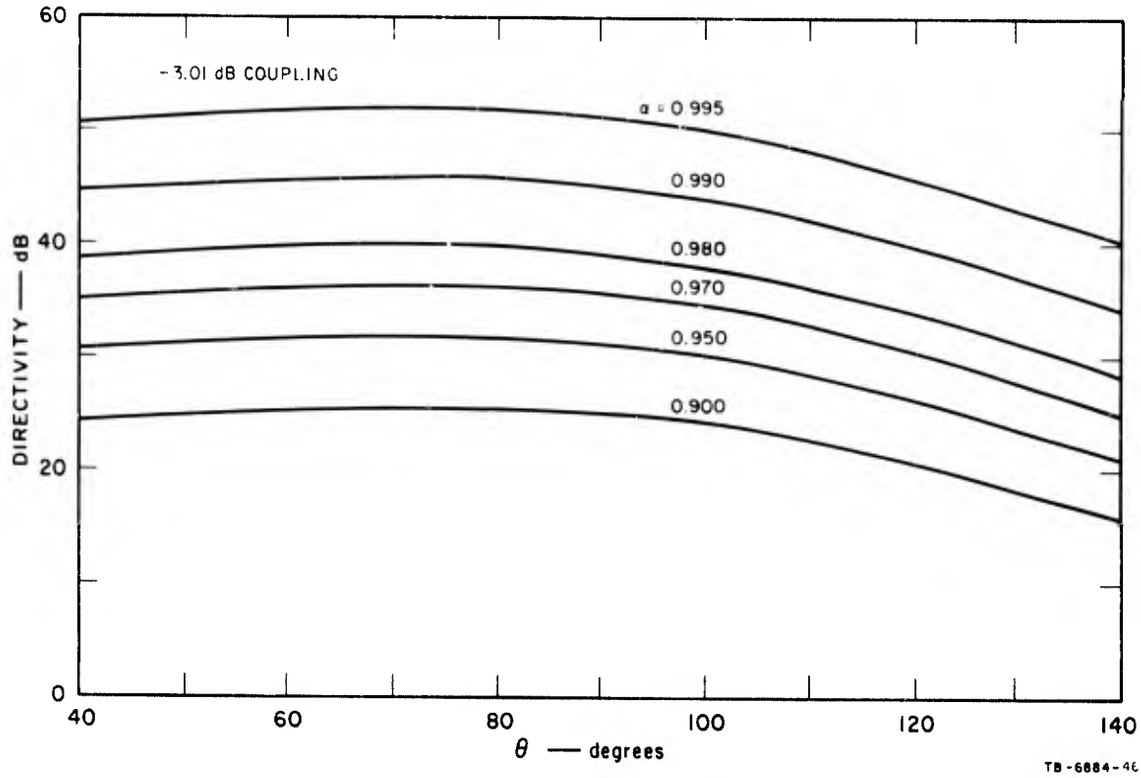

FIG. III-23 THEORETICAL MAXIMUM DIRECTIVITY FOR -3.01-dB MICROSTRIP DIRECTIONAL COUPLERS

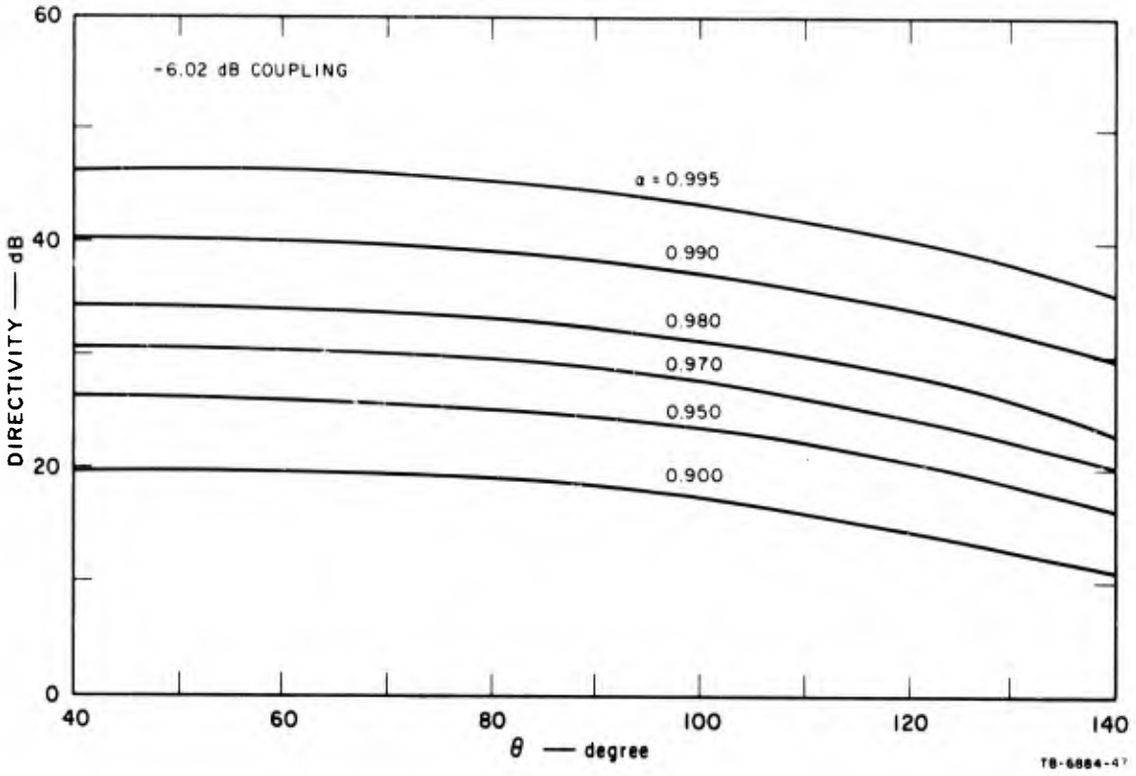

FIG. III-24 THEORETICAL MAXIMUM DIRECTIVITY FOR -6.02-dB MICROSTRIP DIRECTIONAL COUPLERS

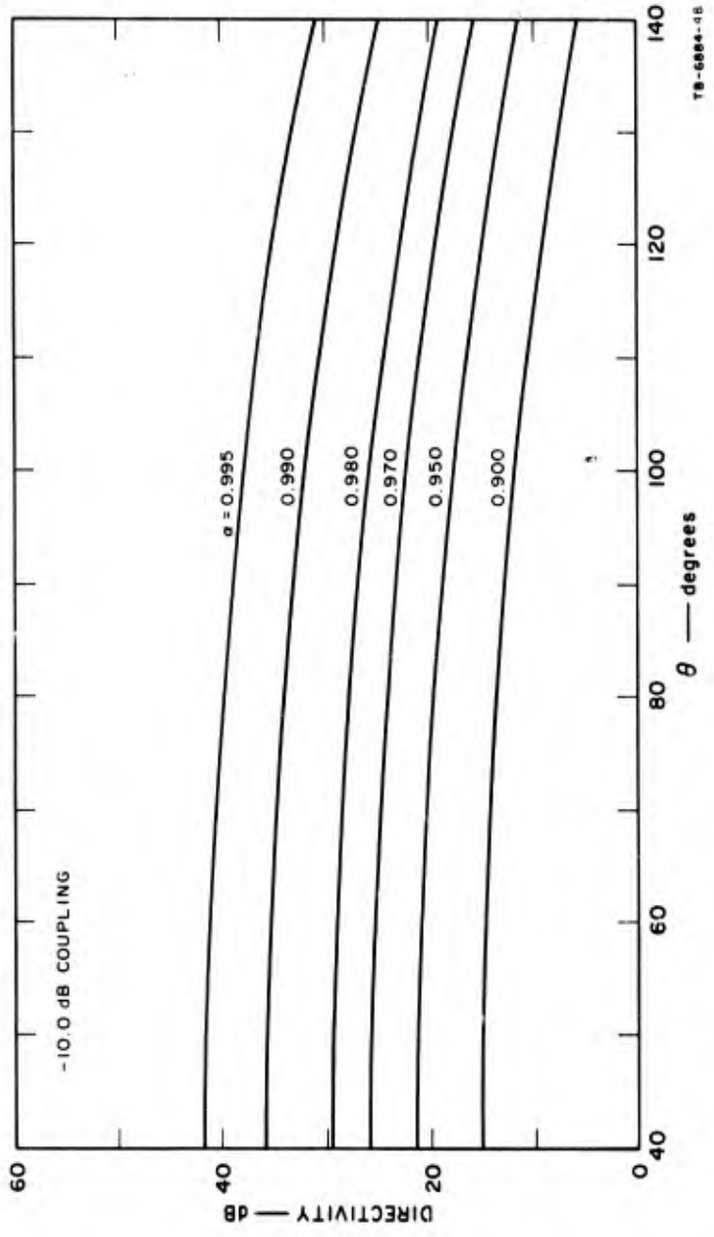

FIG. III-25 THEORETICAL MAXIMUM DIRECTIVITY FOR -10.0-dB MICROSTRIP DIRECTIONAL COUPLERS

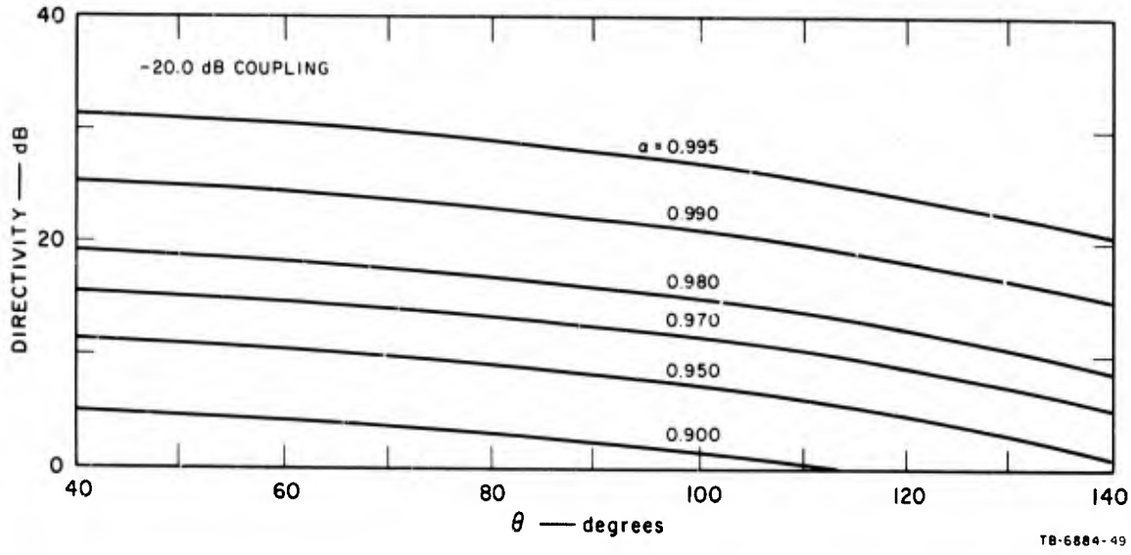

FIG. III-26 THEORETICAL MAXIMUM DIRECTIVITY FOR -20.0-dB MICROSTRIP DIRECTIONAL COUPLERS

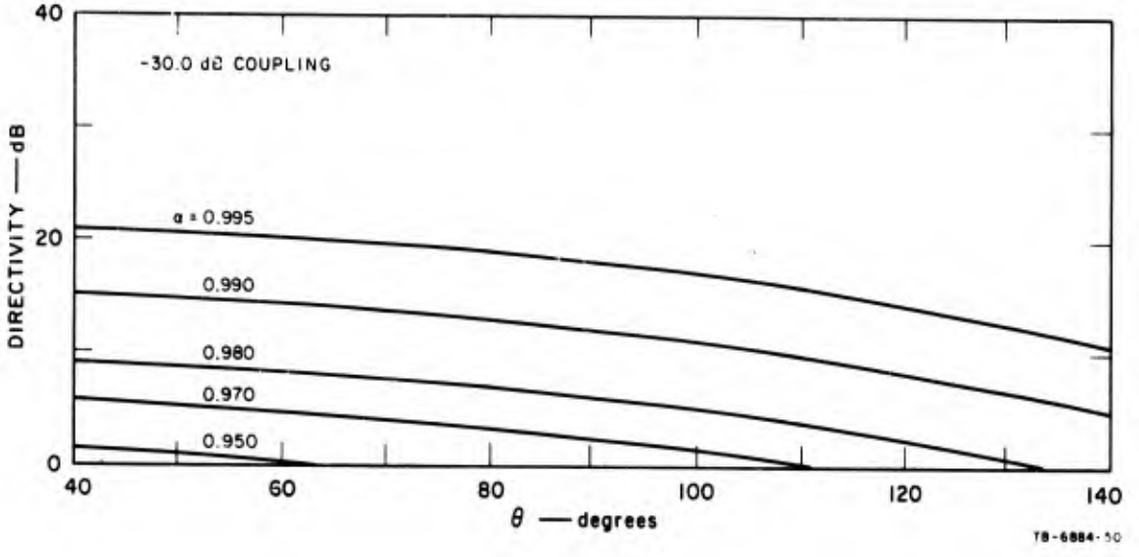

FIG. III-27 THEORETICAL MAXIMUM DIRECTIVITY FOR -30.0-dB MICROSTRIP DIRECTIONAL COUPLERS

IV THEORY AND DESIGN OF TRANSMISSION-LINE ALL-PASS EQUALIZERS

A. General

In this section a general theory for transmission-line equalizers is presented. The theory is equally valid for both waveguide and TEM transmission lines. Strictly speaking, the theory applies for commensurate transmission-line networks only, but it is not essential that the network being equalized, or even the equalizer itself, be of commensurate length lines. Particularly in narrow-band systems various approximate equivalent circuits are possible, indeed necessary.

Microwave equalizer design has been treated by several authors. Beatty[1] described a differential phase shifter using two couplers and ganged short circuits; Woo[2] an adjustable delay equalizer utilizing an adjustable dielectric rod in a circular waveguide, and Abele and Wang[3] an adjustable narrow-band equalizer that uses a circular cylindrical cavity supporting two orthogonal modes. Other authors[4-7] described designs of special circuits of TEM equalizers that use coupled-line techniques. All of these circuits have proved useful contributions to the microwave art. However, in the above papers no unifying principle appears to have been described that relates these designs to one another, or that permits extension to higher-order networks. The paper of Scanlan and Rhodes,[8] in which a general theory for all-pass TEM commensurate transmission-line equalizers is presented, is therefore particularly significant in that such a unifying principle is described.

In their paper, Scanlan and Rhodes extended the concepts of lumped element equalizer theory, such as those described by Bode,[9] to commensurate transmission-line networks. They showed that any commensurate line length TEM all-pass equalizer can be realized by a cascade of first- and second-order all-pass networks, the first-order network being one that realizes the real, and the second-order network being one that

realizes the complex zeroes of the transmission function. They also presented design methods for circuits that could realize these transmission zeroes regardless of their locations in the complex plane. These circuits, however, are not extendible to waveguide equalizers.

In this section, a general theory for analysis and design of transmission-line equalizers which use circulators, or 3-dB hybrids, is developed. The theory is equally applicable to both waveguide and TEM networks. The basic approach is similar to Merlo's.[10]

B. Theory

Scanlan and Rhodes[8] pointed out that any TEM all-pass commensurate transmission network must have a transfer function of the form*

$$S_{12}(t) = \pm \left(\frac{1 - t}{1 + t}\right)^{n/2} \frac{H(-t)}{H(t)} \qquad \text{(IV-1)}$$

where

$$t = \tanh(\gamma L) = \Sigma + i\Omega \qquad \text{(IV-2)}$$

is Richards' transformation,[11] γ is the complex propagation constant, and L is a commensurate length of the network. H(t) is a strict Hurwitz polynomial.

Of course, Richards' transformation applies also to commensurate waveguide transmission-line networks, so that Eq. (IV-1) is equally valid for TE- and TM-mode supporting waveguides. On the "real frequency axis," $\Sigma = 0$, and it is well known that

$$t = i\Omega = i \tan \theta \quad , \qquad \text{(IV-3)}$$

$$\theta = \frac{2\pi}{\lambda_g} L \quad , \qquad \text{(IV-4)}$$

*The minus sign in Eq. (IV-1) was not present in the Scanlan-Rhodes paper. It is inserted here for full generality. In this section there is no difficulty realizing networks with $S_{12}(0) = -1$. This is not possible with the circuits of Scanlan and Rhodes.

with λ_g being the guide wavelength, and $i = \sqrt{-1}$. Equation (IV-4) can also be expressed in terms of frequency variables. Define

$$f = \text{frequency} \tag{IV-5}$$

$$f_{co} = \begin{cases} \text{cutoff frequency of the waveguide} \\ \text{(0 for TEM lines)} \end{cases} \tag{IV-6}$$

$$f_0 = \text{center frequency of the equalizer} \quad . \tag{IV-7}$$

Then,

$$\theta = \frac{\pi}{2}\left[\frac{F^2 - F_0^2}{1 - F_0^2}\right]^{1/2} \quad , \tag{IV-8}$$

with

$$F = f/f_0 \quad , \tag{IV-9}$$

$$F_0 = f_{co}/f_0 \quad , \tag{IV-10}$$

and L chosen so that $\theta = \pi/2$ at $F = 1$. At this point it is also convenient to introduce the function $S(F,F_0)$ which will be present in subsequent equations. This function is defined as

$$S(F,F_0) = \frac{F}{\left[F^2 - F_0^2\right]^{1/2}\left[1 - F_0^2\right]^{1/2}} = \frac{2}{\pi}\frac{d\theta}{dF} \tag{IV-11}$$

with

$$S(F,0) = 1 \quad , \tag{IV-12}$$

for all F. On the real frequency axis, the phase of the transfer function, denoted as β, is*

---

*In Eq. (IV-14) and all subsequent expressions involving the phase, β should be replaced by $\beta + \pi$ if $S_{12}(0) = -1$.

$$\beta = - i \left\{ \ln S_{12}(i\Omega) \right\} \qquad \text{(IV-13)}$$

$$= - i \left\{ \frac{n}{2} \ln \frac{1 - i\Omega}{1 + i\Omega} + \ln \frac{H(-i\Omega)}{H(i\Omega)} \right\} \quad . \qquad \text{(IV-14)}$$

This can also be written as

$$\beta = - n \tan^{-1} \Omega - 2 \tan^{-1} \left\{ \frac{\text{odd part of } H(i\Omega)}{\text{even part of } H(i\Omega)} \right\} \qquad \text{(IV-15)}$$

$$= - n \theta - 2 \tan^{-1} \left\{ (-i) \frac{H(i\Omega) - H(-i\Omega)}{H(i\Omega) + H(-i\Omega)} \right\} \quad . \qquad \text{(IV-16)}$$

It is seen from Eq. (IV-16) that the contribution to β of the factor $[(1 - t)/(1 + t)]^{n/2}$ is $-n\,\theta$. This is equivalent to a transmission phase delay of a matched line $n\,\theta$ degrees long. The second contribution is the term $-2 \tan^{-1} \{[\text{odd part of } H(i\Omega)]/[\text{even part of } H(i\Omega)]\}$. Note that the argument of the $\tan^{-1}$ function is a rational fractional polynomial consisting of the odd part divided by the even part of a Hurwitz polynomial. Such rational fractional polynomials are known to be reactance functions.*

This is an important point since it is a property of reactance functions to be monotonic increasing throughout the real frequency axis. Consequently, the phase must be monotonic decreasing regardless of the complexity of the equalizer. Naturally, this places a fundamental limitation on the equalization obtainable with an all-pass equalizer.

The analytic form of the reactance function is

$$-i \frac{\text{Od}[H(i\Omega)]}{\text{Ev}[H(i\Omega)]} = A \frac{\Omega\left[\Omega^2 - \Omega_2^2\right]\left[\Omega^2 - \Omega_4^2\right] \cdots}{\left[\Omega^2 - \Omega_1^2\right]\left[\Omega^2 - \Omega_3^2\right] \cdots} \quad , \qquad \text{(IV-17)}$$

with

$$\Omega_1 < \Omega_2 < \Omega_3 \quad ,$$

and A and Ω_i positive but otherwise arbitrary.

---

*A reactance function is an impedance or admittance whose real part is zero for all frequencies.

The time delay τ of the all-pass equalizer may be defined as

$$\tau = \frac{-d\beta}{d\omega} \quad , \tag{IV-18}$$

which in normalized form can be shown to equal

$$\tau_N = \frac{1}{4}\left[n + \left(1 + \Omega^2\right)\frac{d}{dt}\left\{\ln H(t) - \ln H(-t)\right\}_{t=i\Omega}\right]S\left(F,F_0\right) \quad , \tag{IV-19}$$

$$\tau_N = \frac{1}{4}\left[n + \left(1 + \Omega^2\right)\left\{\frac{H'(t)}{H(t)} - \frac{H'(-t)}{H(-t)}\right\}_{t=i\Omega}\right]S\left(F,F_0\right) \quad , \tag{IV-20}$$

where

$$H'(-t) = \frac{d}{dt}\left[H(-t)\right]$$

and

$$\tau_N = \tau f_0 \quad . \tag{IV-21}$$

Note, that for TEM lines, $F_0 = 0$ and the function $S\left(F,F_0\right)$ reduces to 1.0, making Eqs. (IV-19) and (IV-20) equivalent to those given by Scanlan and Rhodes.[8] Since H(t) is a Hurwitz polynomial, it is expressible as a produce of factors of its real and complex zeroes. That is

$$H(t) = \prod_{i=1}^{k}\left(t + \sigma_i\right)\prod_{j=1}^{m}\left(t^2 + 2\,\sigma_j t + \left|t_j\right|^2\right) \tag{IV-22}$$

with

$$\sigma_i > 0$$

$$t_j = \sigma_j + i\,\omega_j$$

$$k + m = \text{degree of } H.$$

Substituting Eq. (IV-22) into Eq. (IV-20) results in

$$\tau_N = \frac{1}{4}\left[n + (1+\Omega^2)\left\{\sum_{i=1}^{k}\frac{1}{\sigma_i + i\Omega} + \frac{1}{\sigma_i - i\Omega} + 2\sum_{j=1}^{m}\frac{\sigma_j + i\Omega}{|t_j|^2 - \Omega^2 + i2\,\sigma_j\,\Omega} + \frac{\sigma_j - i\Omega}{|t_j|^2 - \Omega^2 - i2\,\sigma_j\,\Omega}\right\}\right] S(F,F_0) \quad . \quad \text{(IV-23)}$$

Equation (IV-23) reveals the time delay of an all-pass equalizer to be equivalent to the delay of a cascade of first-order all-pass networks (all-pass C-sections) and second-order all-pass networks (all-pass D-sections). Thus, any all-pass equalizer response can be realized by a cascade of all-pass networks that are of no greater complexity than second-order.[8,9]

The phase and normalized time delay for a first-order all-pass equalizer are

$$\beta = -2\tan^{-1}\frac{\Omega}{\sigma} \quad , \quad \text{(IV-24)}$$

$$\tau_N = \frac{1}{2}\,\frac{\sigma(1+\Omega^2)}{\sigma^2 + \Omega^2}\,S(F,F_0) \quad , \quad \text{(IV-25)}$$

respectively.

The phase and normalized time delay for a second-order all-pass equalizer are

$$\beta = -2\tan^{-1}\frac{2\,\sigma_o\,\Omega}{|t_o|^2 - \Omega^2} \quad , \quad \text{(IV-26)}$$

$$\tau_N = \sigma_o(1+\Omega^2)\,\frac{\Omega^2 + |t_o|^2}{\Omega^4 + 2\,\Omega^2\left(\sigma_o^2 - \omega_o^2\right) + |t_o|^4}\,S(F,F_0) \quad , \quad \text{(IV-27)}$$

respectively.

Scanlan and Rhodes presented delay data for TEM C-sections and D-sections. Consequently, those data will not be repeated here. Limited data for waveguide C- and D-sections are given in Figs. IV-1 through IV-3.

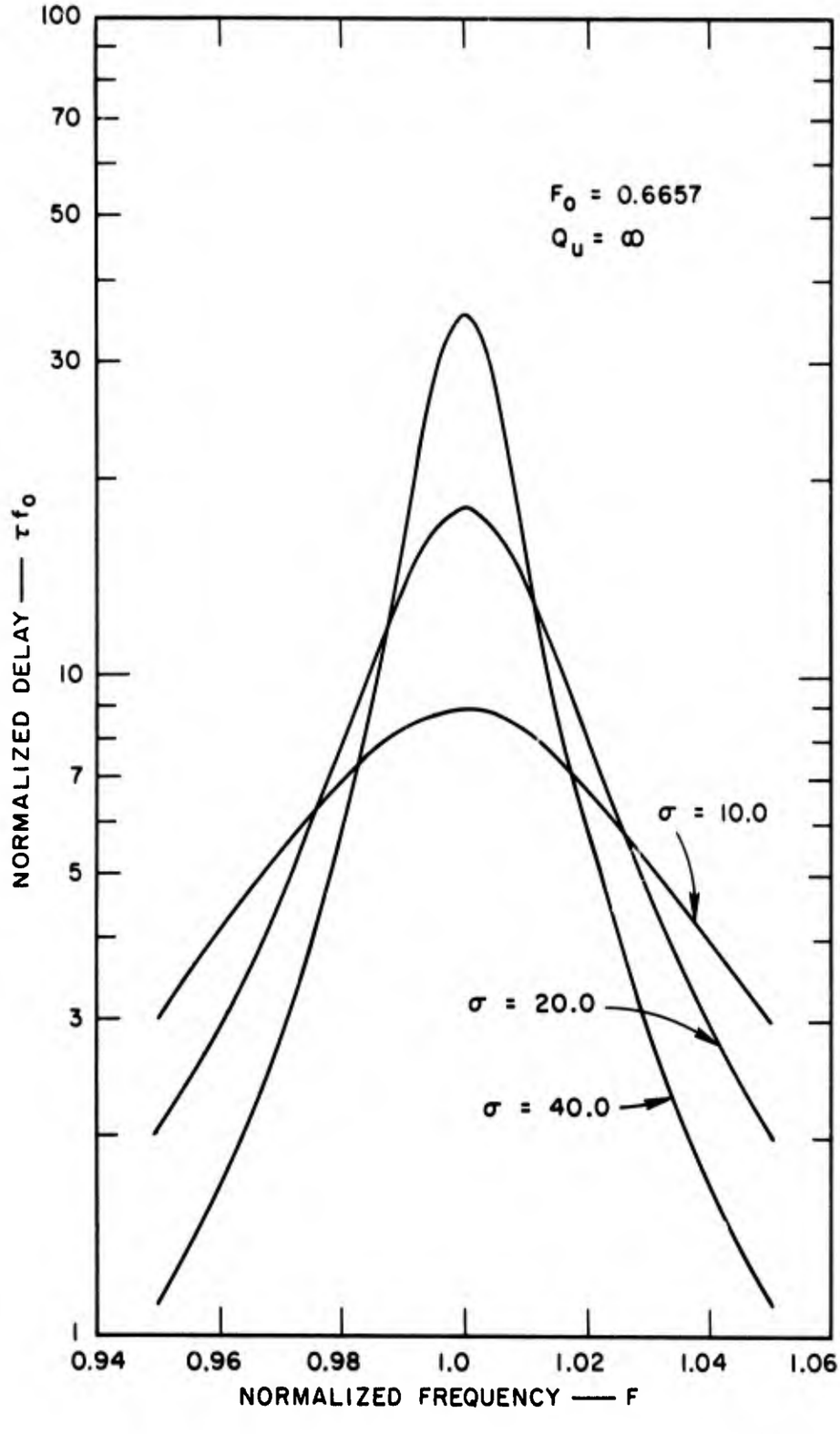

FIG. IV-1 NORMALIZED TIME DELAY OF C-SECTION WAVEGUIDE EQUALIZER

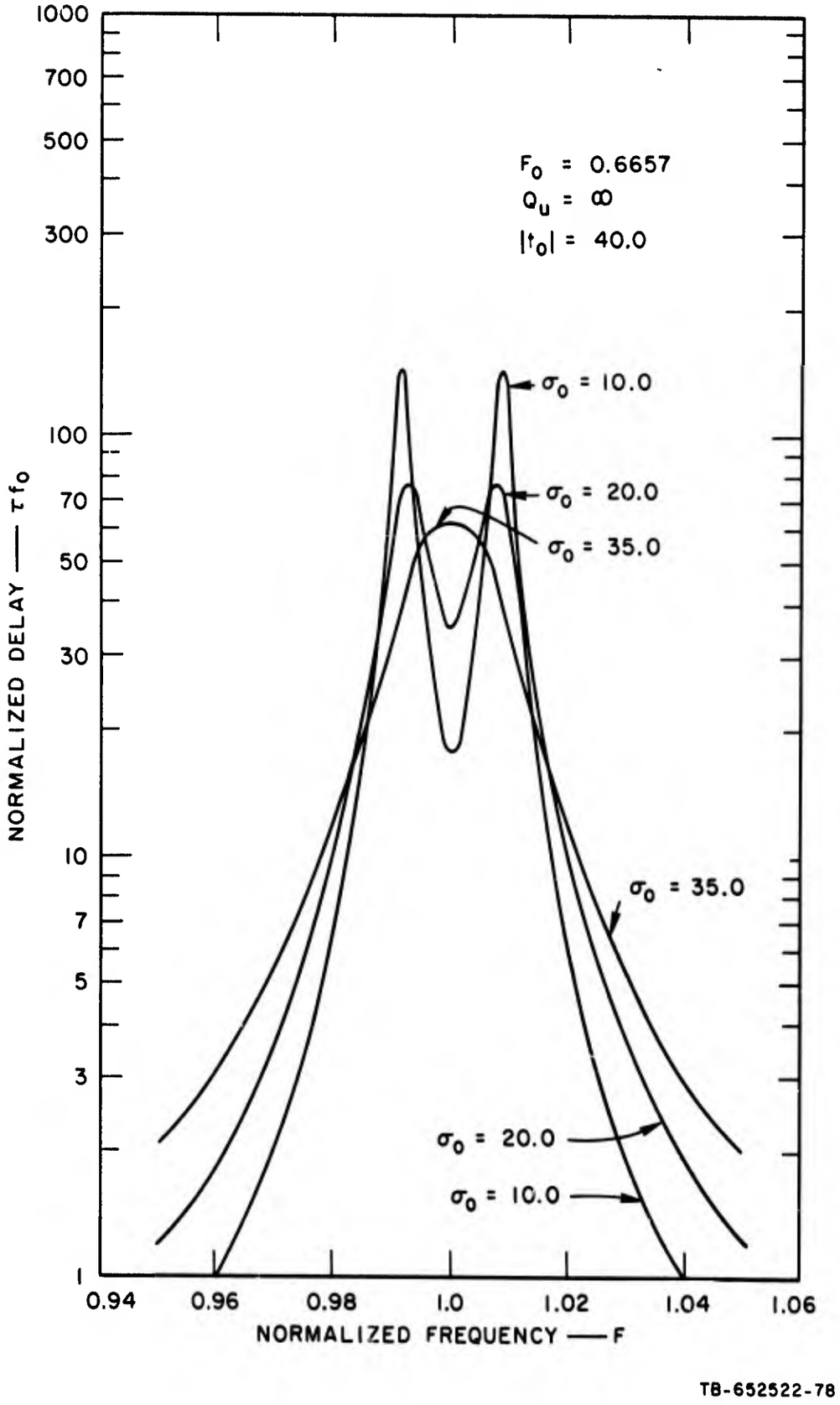

FIG. IV-2 NORMALIZED TIME DELAY OF D-SECTION WAVEGUIDE EQUALIZER WITH $|t_0|$ CONSTANT AND σ_0 AS A PARAMETER

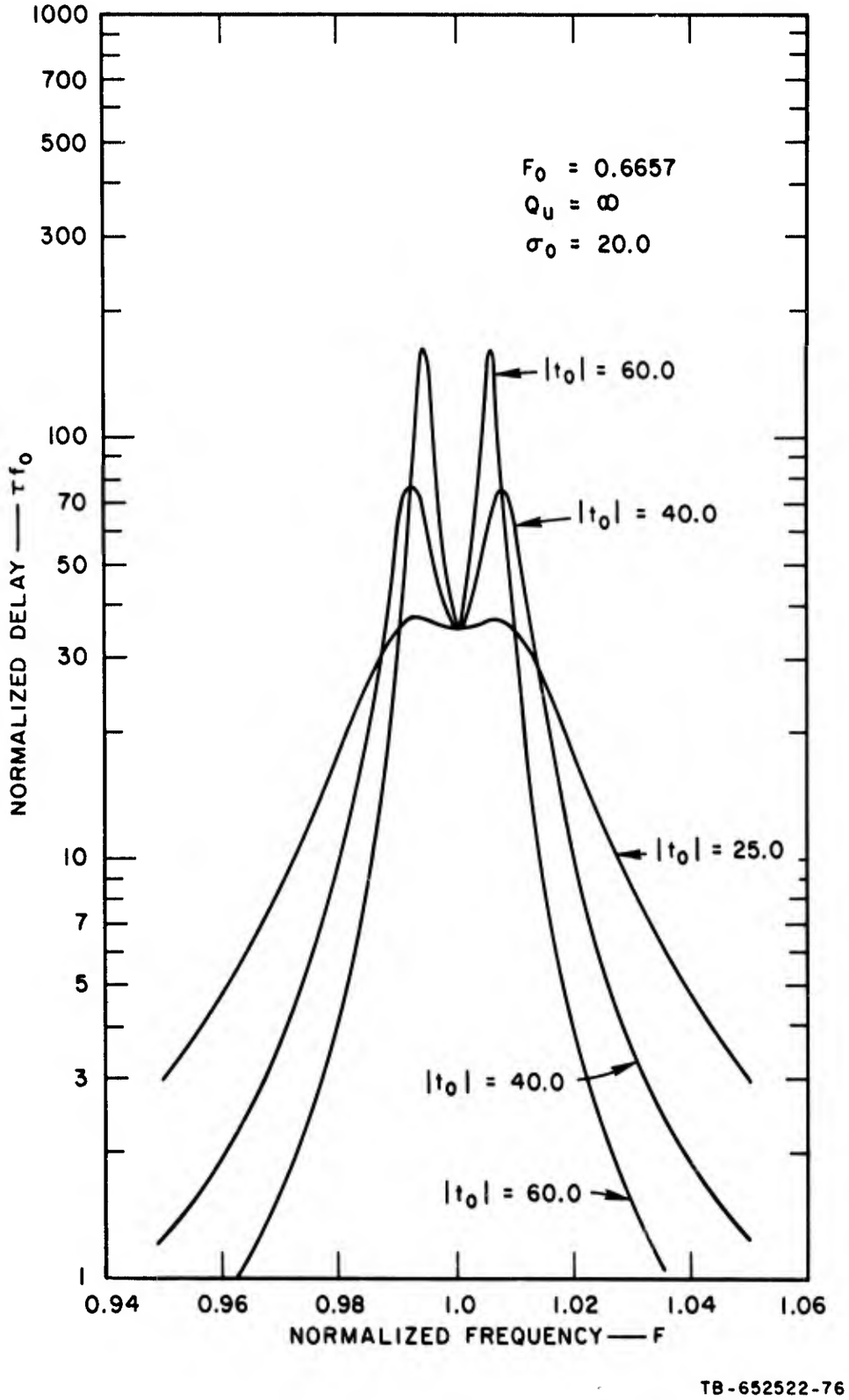

FIG. IV-3 NORMALIZED TIME DELAY OF D-SECTION WAVEGUIDE EQUALIZER WITH σ_0 CONSTANT AND $|t_0|$ AS A PARAMETER

However, for waveguide networks, the additional factor $S(F,F_0)$ in Eqs. (IV-25) and (IV-27) makes it impractical to present extensive data in the limited space available. The example data in Figs. IV-1 through IV-3 are for $F_0 = 0.6657$, corresponding to an X-band waveguide network having a center frequency of 10.0 GHz.

Figure IV-1 gives normalized time delay versus F for lossless waveguide C-sections.* The transfer function is $S_{12}(t) = \pm (\sigma - t)/(\sigma + t)$. The data show that increasing σ results in more narrow-band responses and greater peak delays. Although it is not clearly evident from the graphs, the curves in Fig. IV-1 as well as in Figs. IV-2 and IV-3, are asymmetrical about F = 1 because of the function $S(F,F_0)$ in the delay formulas. However, for narrow-band responses the near symmetry is apparent.

Figure IV-2 gives corresponding data for waveguide D-sections. The transfer function is

$$S_{12}(t) = \pm \frac{|t_o|^2 - 2\,\sigma_o\, t + t^2}{|t_o|^2 + 2\,\sigma_o\, t + t^2} \quad .$$

The data of Fig. IV-2 are for $|t_o| = 40$ with σ_o as a parameter. For second-order systems it is seen that increasing σ_o from a relatively small value to that approaching $|t_o|$ diminishes the extremes of the delay and eventually produces a form of "critically coupled" response in which the double peak delay curve is eliminated.

Figure IV-3 also gives data for waveguide D-sections, but with σ_o held constant and $|t_o|$ as a parameter. These data show that increasing $|t_o|$ makes the delay response more narrow band while simultaneously increasing the peak delay. The local minimum at F = 1 is independent of $|t_o|$, and, by Eq. (IV-27), is

$$\tau_N\ (F = 1) = \sigma_o\, S(1,F_0) \quad .$$

---

*The effects of loss are described later.

Figures IV-1 through IV-3 give sufficient data to indicate the dependence of the delay curves on the locations of the real and complex zeroes of the transmission function. A designer may use these data to obtain insight in choosing suitable zeroes in the design of specific equalizers. However, it is emphasized that the data are not universal, but rather, depend on the value of F_0 in the function $S(F,F_0)$. Therefore, it should be anticipated that each equalizer problem may require its own set of delay curves. However, since the delay equations are quite simple, and computers are generally available, this should present no problem.

The next step in the development of the theory requires analyzing the transmission-line network shown in Fig. IV-4. It is seen to consist

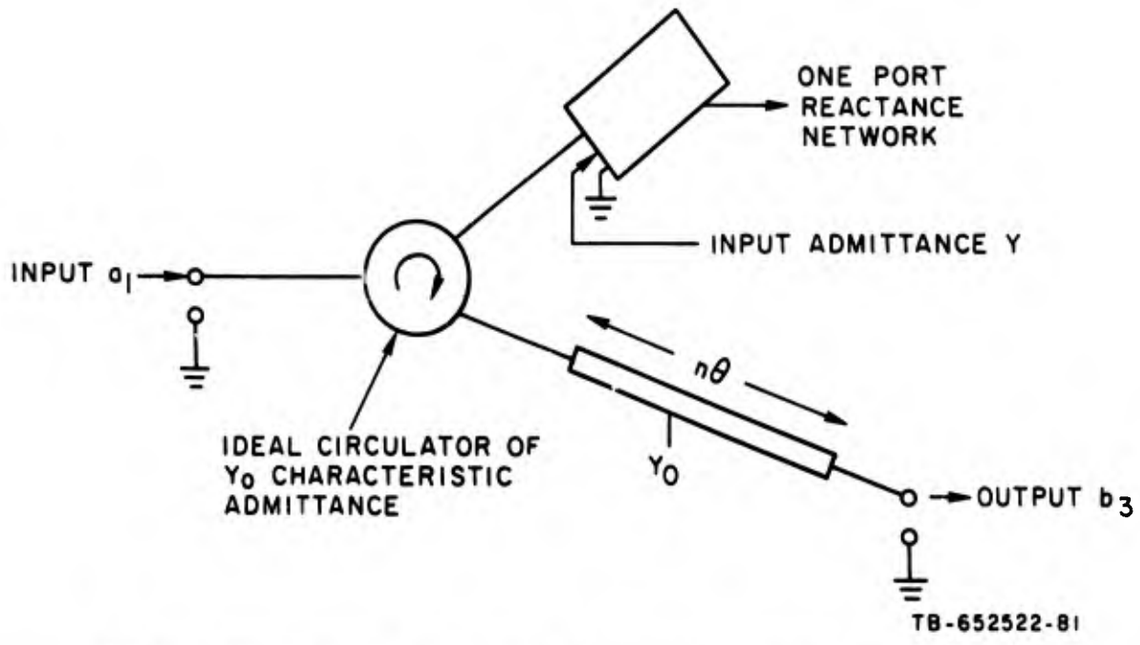

FIG. IV-4 DIAGRAM OF AN IDEALIZED, GENERAL, MICROWAVE EQUALIZER

of an ideal three-part circulator, having Port 1 as input, Port 2 terminated in a lossless reactance network of commensurate transmission lines and, in the general case, the output port in series with a matched line n θ long. Calculation of the transfer function gives

$$\frac{b_3}{a_1}(i\Omega) = S_{13}(i\Omega) = e^{-in\theta}\,\Gamma(i\Omega) \quad , \tag{IV-28}$$

where

$$\Gamma(i\Omega) = \frac{Y_0(i\Omega) - Y(i\Omega)}{Y_0(i\Omega) + Y(i\Omega)} = \frac{1 - y(i\Omega)}{1 + y(i\Omega)} \quad , \tag{IV-29}$$

Y_0 being the characteristic admittance of the circulator, $Y(i\Omega)$ the input admittance of the reactance network, and

$$y = Y/Y_0 \quad . \tag{IV-30}$$

Since y is a reactance function, it may be expressed as the ratio of the odd-to-even or even-to-odd parts of an associated Hurwitz polynomial. Choosing the former,

$$y(i\Omega) = \frac{\text{odd } H(i\Omega)}{\text{even } H(i\Omega)} = \frac{H(i\Omega) - H(-i\Omega)}{H(i\Omega) + H(-i\Omega)} \quad . \tag{IV-31}$$

Substituting Eq. (IV-31) into Eq. (IV-29) gives

$$\Gamma(i\Omega) = \frac{1 - y(i\Omega)}{1 + y(i\Omega)} = \frac{H(-i\Omega)}{H(i\Omega)} \quad . \tag{IV-32}$$

Also, using the identity

$$e^{i2\theta} = \frac{1 - i\tan\theta}{1 + i\tan\theta} = \frac{1 - i\Omega}{1 + i\Omega} \quad , \tag{IV-33}$$

it is found that

$$e^{-in\theta} = \left(\frac{1 - i\Omega}{1 + i\Omega}\right)^{n/2} \quad . \tag{IV-34}$$

Finally, by substituting Eqs. (IV-34) and (IV-32) into Eq. (IV-28) and by analytic continuation, replacing $i\Omega$ by t, we obtain

$$\frac{b_3}{a_1}(t) = S_{13}(t) = \left(\frac{1 - t}{1 + t}\right)^{n/2} \frac{H(-t)}{H(t)} \quad . \tag{IV-35}$$

A dual formulation with

$$\Gamma(i\Omega) = \frac{z(i\Omega) - 1}{z(i\Omega) + 1} \quad , \tag{IV-36}$$

$$z(i\Omega) = \frac{H(i\Omega) - H(-i\Omega)}{H(i\Omega) + H(-i\Omega)} \tag{IV-37}$$

results in

$$\frac{b_3}{a_1}(t) = S_{13}(t) = -\left(\frac{1 - t}{1 + t}\right)^{n/2} \frac{H(-t)}{H(t)} \quad . \tag{IV-38}$$

Equations (IV-35) and (IV-38) taken together are identical with Eq. (IV-1). Consequently, it has been proven that any arbitrary transmission-line all-pass transfer function can be realized by the network* of Fig. IV-4.

A practical objection to the network of Fig. IV-4 is that the required reactance function calls for combinations of open- and short-circuited stubs all connected at a single reference plane. This requirement can be removed by calling on a theorem of Richards.[11] Richards proved that any transmission-line reactance network is realizable as a cascade of commensurate transmission lines terminated in a short or open circuit. Therefore, the following theorem may be stated:

> Any arbitrary all-pass commensurate transmission-line transfer function is realizable by a network consisting of an ideal three-port circulator having (1) the second port terminated in a reactance network of cascaded commensurate transmission lines, and (2) a matched line n θ long connected in series with either the input or output port.

*The network of Fig. IV-4 is clearly nonreciprocal. A reciprocal equalizer can be obtained by replacing the three-port circulator by a four-port one and terminating nonadjacent ports in identical reactance networks. Alternatively, a quadrature hybrid may be used in place of the four-port circulator, with the normally coupled ports being terminated in identical reactance networks.

C. Synthesis

A general design procedure for synthesizing an equalizer of the type shown in Fig. IV-4 is as follows.

First, determine suitable locations for the zeroes of H(t) that give the required equalization. To this end Eqs. (IV-25) and (IV-27) may be programmed to give extensive graphical data. (Much graphical data are already given in Scanlan and Rhodes for TEM networks.) More generally, special numerical or analogue methods[12] may be used to obtain suitable, real, and complex zeroes of H(t). Once the zeroes have been determined, the Hurwitz function H(t) is formed. Next, y(t) [or z(t)] is determined via

$$\left.\begin{matrix} y(t) \\ z(t) \end{matrix}\right\} = \frac{H(t) - H(-t)}{H(t) + H(t)} \quad . \qquad \text{(IV-39)}$$

Last, y(t) is realized as a cascade of transmission lines terminated in an open circuit [or z(t) is similarly realized and terminated in a short circuit] using Richards' synthesis procedure.*

A similar synthesis procedure may be used to develop a phase equalizer. In this case one starts with the negative of the tangent of one-half the phase function,

$$\tan \frac{\beta}{2} = \frac{H(i\Omega) - H(-i\Omega)}{i[H(i\Omega) + H(i\Omega)]} = \frac{A\,\Omega\left(\Omega^2 - \Omega_2^2\right)\cdots}{\left(\Omega^2 - \Omega_1^2\right)\left(\Omega^2 - \Omega_3^2\right)} = \frac{y(i\Omega)}{i} \quad . \qquad \text{(IV-40)}$$

The poles and zeroes, Ω_1, Ω_2, ... and A, are chosen to obtain the required phase equalization. Once these have been determined, y(t) or z(t) is formed by replacing $i\Omega$ by t, and then synthesized as described.

---

*A general recursive formula that develops the reactance function y(t) [or z(t)] in a cascade of transmission lines using the associated Hurwitz function H(t) rather than y(t) is given in Appendix A. The formula is based on Richards' method but is specialized to reactance functions. It is generally simpler to program on a computer.

In many cases of practical interest, delay or phase qualization can be obtained with only a first- or second-order network, or a combination of first- and second-order networks. Therefore, it is useful to tabulate the formulas for their design for quick reference. The form of the cascaded transmission-line reactance network is shown in Fig. IV-5, and the notation there is consistent with the formulas given in Table IV. The formulas were obtained by the method described in Appendix A.

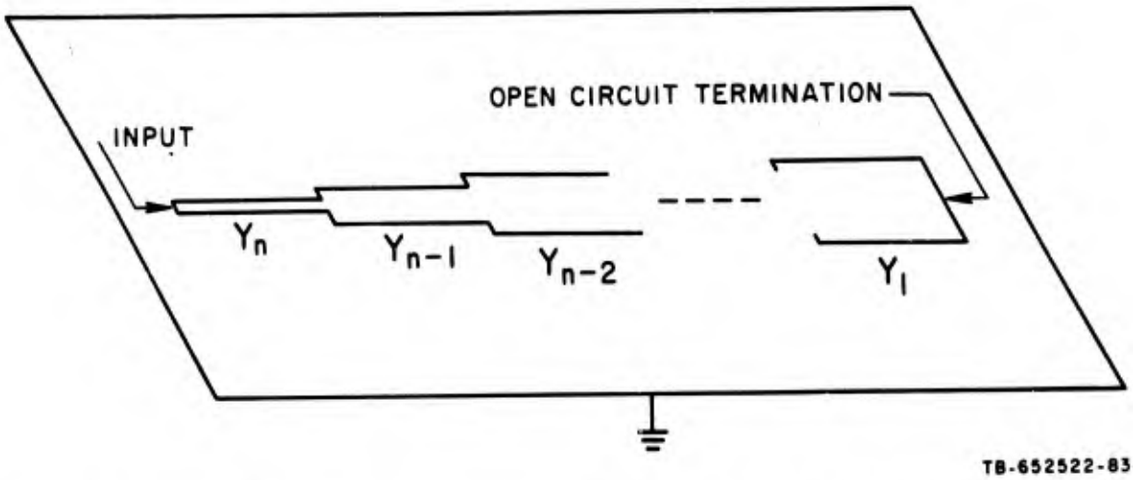

FIG. IV-5 GENERAL REACTANCE NETWORK IN THE FORM OF CASCADED TRANSMISSION LINES (The subscripts of the line admittance are consistent with the formulas in table IV-1)

D. Practical Circuit Realizations

In many narrow-band applications, the values of impedance or admittance obtained from direct synthesis, or from Table IV, will not be practical. For those cases it is necessary to develop alternative networks that approximate the response of the commensurate transmission-line reactance network called for by the theory. A commonly used circuit in equalizer design is the shunt inductive coupled cavity.[10] By direct analysis, it is easily shown that a single cavity corresponds to a waveguide C-section; a double cavity corresponds to a waveguide D-section, or possibly a double C-section. Additional cavities will naturally correspond to higher-order networks, but ones which are reducible to combinations of C- and D-sections. An equivalence between the inductive-coupled n-cavity reactance network and the n-section cascaded commensurate

Table IV

FORMULAS FOR ALL-PASS EQUALIZERS

Case 1: First-Order Network (C-Section)	$H(t) = t + \sigma$ $y(i\Omega) = i\,\frac{\Omega}{\sigma}$ $y_1 = \frac{1}{\sigma}$ $\beta = -2\tan^{-1}\frac{\Omega}{\sigma}$ $\tau_N = \frac{\sigma(1+\Omega^2)}{2(\sigma^2+\Omega^2)}\,S(F,F_0)$
Case 2: Second-Order Network (D-Section)	$H(t) = t^2 + 2\sigma_o t + \lvert t_o\rvert^2$ $y(i\Omega) = \frac{i2\sigma_o\Omega}{\lvert t_o\rvert^2 - \Omega^2}$ $y_2 = \frac{2\sigma_o}{1+\lvert t_o\rvert^2}$ $y_1 = \frac{2\sigma_o/\lvert t_o\rvert^2}{1+\lvert t_o\rvert^2} = y_2/\lvert t_o\rvert^2$ $\beta = -2\tan^{-1}\frac{2\sigma_o\Omega}{\lvert t_o\rvert^2 - \Omega^2}$ $\tau_N = \sigma_o(1+\Omega^2)\,\frac{\lvert t_o\rvert^2+\Omega^2}{\lvert t_o\rvert^4 + 2\Omega^2(\sigma_o^2 - \omega_o^2) + \Omega^4}\,S(F,F_0)$
Case 3: Double First-Order Network	$H(t) = (t+\sigma_1)(t+\sigma_2) = t^2 + t(\sigma_1+\sigma_2) + \sigma_1\sigma_2$ $y(i\Omega) = \frac{i\Omega(\sigma_1+\sigma_2)}{\sigma_1\sigma_2 - \Omega^2}$ $y_2 = \frac{\sigma_1+\sigma_2}{1+\sigma_1\sigma_2}$ $y_1 = \frac{(\sigma_1+\sigma_2)/\sigma_1\sigma_2}{1+\sigma_1\sigma_2} = y_2/(\sigma_1\sigma_2)$

Table IV (Concluded)

Case 3 (Continued)	$\beta = -2 \tan^{-1} \dfrac{\Omega(\sigma_1 + \sigma_2)}{\sigma_1\sigma_2 - \Omega^2}$ τ_N = Superposition of two first-order systems $\tau_N = \dfrac{(1+\Omega^2)(\sigma_1+\sigma_2)}{2}\left\{\dfrac{\sigma_1\sigma_2 + \Omega^2}{(\sigma_1\sigma_2)^2 + \Omega^2(\sigma_1^2+\sigma_2^2) + \Omega^4}\right\}S(F,F_0)$
Case 4: Third-Order Network (C-Section + D-Section)	$H(t) = (t + \sigma_1)\left(\lvert t_o\rvert^2 + 2\,\sigma_o t + t^2\right)$ $H(t) = t^3 + (\sigma_1 + 2\,\sigma_o)t^2 + \left(2\,\sigma_o\sigma_1 + \lvert t_o\rvert^2\right)t + \sigma_1\lvert t_o\rvert^2$ $y(i\Omega) = i\Omega \dfrac{\left(2\,\sigma_o\sigma_1 + \lvert t_o\rvert^2\right) - \Omega^2}{\sigma_1\lvert t_o\rvert^2 - (\sigma_1 + 2\,\sigma_o)\Omega^2}$ Define: $a = \left(2\,\sigma_o\sigma_1 + \lvert t_o\rvert^2\right)$, $b = \sigma_1\lvert t_o\rvert^2$, $c = (\sigma_1 + 2\,\sigma_o)$. Then $y_3 = \dfrac{a + 1}{b + c}$ $y_2 = y_3 \dfrac{ac - b}{(1 + a)b + (b + c)}$ $y_1 = y_2 \dfrac{(b + c)}{b(a + 1)}$ $\beta = -2 \tan^{-1} \dfrac{\Omega\left[2\,\sigma_o\sigma_1 + \lvert t_o\rvert^2 - \Omega^2\right]}{\sigma_1\lvert t_o\rvert^2 - (\sigma_1 + 2\,\sigma_o)\Omega^2}$ τ_N = Superposition of a first- and complex second-order system

transmission-line circuit may be established by computing the respective network input impedances in the variable t, expanding these functions about $t = \infty$, and equating corresponding coefficients.* The method is demonstrated below only for the two-cavity case, but the generalization of the method to higher-order networks is obvious.

The inductive coupled two-cavity network is illustrated in Fig. IV-6. The input cavity is coupled to the circulator via inductive reactance X_2; the second cavity is coupled via X_1. At band center the electrical length of the input cavity is θ_2 radians, and that of the remaining cavity is θ_1 radians.

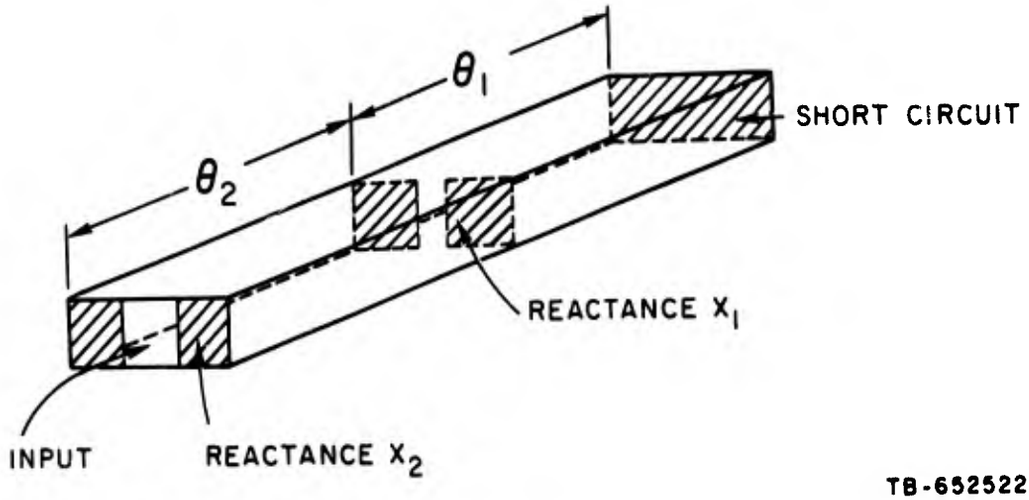

FIG. IV-6 INDUCTIVE COUPLED TWO-CAVITY REACTANCE NETWORK FOR A SECOND-ORDER MICROWAVE EQUALIZER

Using the concept of impedance inverters,[13] the network of Fig. IV-6 may be replaced by the equivalent network of Fig. IV-7. The equivalent network consists of two cavities, each π radians long at band

---

*This procedure is nearly analogous to Cohn's method,[13] but is more accurate for wider bandwidths.

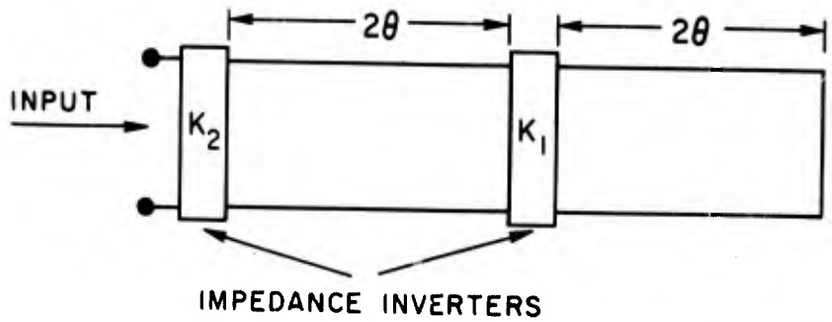

TB-652522-85

FIG. IV-7 EQUIVALENT NETWORK TO THAT OF FIG. IV-6 USING IMPEDANCE INVERTERS

center and coupled via ideal impedance inverters K_2 and K_1. The relationships between the two networks of Figs. IV-6 and IV-7 are

$$\frac{X_i}{Z_0} = \frac{K_i/Z_0}{1 - (K_1/Z_0)^2} \quad , \quad i = 2, 1 \quad , \qquad \text{(IV-41)}$$

and

$$\theta_2 = \pi - \frac{1}{2}\left\{\tan^{-1}\frac{2X_2}{Z_0} + \tan^{-1}\frac{2X_1}{Z_0}\right\} \quad , \qquad \text{(IV-42)}$$

$$\theta_1 = \pi - \frac{1}{2}\tan^{-1}\frac{2X_1}{Z_0} \quad . \qquad \text{(IV-43)}$$

The commensurate transmission-line cascade that must correspond to the network of Fig. IV-6 is the dual of the one given in Fig. IV-5 with $n = 2$, and line 1 terminated in a short circuit. Also, as noted previously, for this case $z(i\Omega)$ and z_i are to replace $y(i\Omega)$ and y_i in Table V, and β is to be replaced by $\beta + \pi$.

Since the cavities in Fig. IV-7 are π radians at band center, in contrast to $\pi/2$ radians for the cascade transmission-line network, the appropriate variable to use for the network in Fig. IV-7 is tan 2θ (rather than tan θ). In terms of t, tan 2θ corresponds to $2t/(1 + t^2)$. The input impedance of the network of Fig. IV-7 is next determined to be

$$\left(Z_{in}\right)_C = a_1\left\{\frac{t + t^3}{1 + b_2 t^2 + t^4}\right\} \quad , \qquad \text{(IV-44)}$$

with

$$a_1 = \frac{2K_2^2\left(1 + K_1^2\right)}{K_1^2} \qquad \text{(IV-45)}$$

and

$$b_2 = \frac{2}{K_1^2}\left(2 + K_1^2\right) \quad . \qquad \text{(IV-46)}$$

$\left(Z_{in}\right)_C$ is next expanded about $t = \infty$ giving

$$\left(Z_{in}\right)_C = \frac{a_1}{t} + \frac{a_1\left(1 - b_2\right)}{t^3} + \text{higher-order terms} \quad . \qquad \text{(IV-47)}$$

The input impedance of the transmission-line cascade is found to be

$$\left(Z_{in}\right)_T = \frac{\left(Z_2 + Z_1\right) t}{1 + Z_1 Y_2 t^2} \quad . \qquad \text{(IV-48)}$$

Expanding $\left(Z_{in}\right)_T$ about $t = \infty$ gives

$$\left(Z_{in}\right)_T = \frac{\left[\frac{Z_1 + Z_2}{Z_1 Y_2}\right]}{t} - \frac{\left[\frac{Z_1 + Z_2}{Z_1 Y_2}^2\right]}{t^3} + \text{higher-order terms} \quad . \qquad \text{(IV-49)}$$

Next, corresponding coefficients of the expanded functions $\left(Z_{in}\right)_T$ in Eq. (IV-49) and $\left(Z_{in}\right)_C$ in Eq. (IV-47) are equated giving

$$\frac{2K_2^2\left(1 + K_1^2\right)}{K_1^2} = \frac{Z_1 + Z_2}{Z_1 Y_2} = C_1 \qquad \text{(IV-50)}$$

$$\frac{2K_2^2\left(1 + K_1^2\right)}{K_1^2} \cdot \frac{2}{K_1^2}\left(2 + K_1^2\right) = \frac{Z_1 + Z_2}{\left(Z_1 Y_2\right)^2} = C_2 \quad . \qquad \text{(IV-51)}$$

These equations may be solved for K_2^2 and K_1^2 yielding

$$K_2^2 = \frac{2C_1^2}{C_2 + 3C_1} \quad , \qquad \text{(IV-52)}$$

$$K_1^2 = \frac{4C_1}{C_2 - C_1} \quad , \tag{IV-53}$$

with a good approximation for $K_i^2 << 1$ being

$$K_2^2 \approx 2C_1^2/C_2 \quad , \tag{IV-54}$$

$$K_1^2 \approx 4C_1/C_2 \quad . \tag{IV-55}$$

Taking the approximate solution above, which will be sufficient in most narrow-band applications, and substituting the values of z_2 and z_1 from Table V gives

$$\frac{K_2}{Z_0} = \frac{2\sqrt{\sigma_o}}{|t_o|} \quad , \tag{IV-56}$$

$$\frac{X_2}{Z_0} = \frac{2\sqrt{\sigma_o}\,|t_o|}{|t_o|^2 - 4\sigma_o} \quad , \tag{IV-57}$$

$$\frac{K_1}{Z_0} = \frac{2}{|t_o|} \quad , \tag{IV-58}$$

$$\frac{X_1}{Z_0} = \frac{2|t_o|}{|t_o|^2 - 4} \quad . \tag{IV-59}$$

These are the required relationships. The values of θ_i are found by substituting back into Eqs. (IV-42) and (IV-43).

A similar analysis for the single cavity (C-section) yields

$$\frac{X_1}{Z_0} = \frac{\sqrt{2\sigma}}{\sigma - 2} \quad , \tag{IV-60}$$

and

$$\theta_1 = \pi - \frac{1}{2}\tan^{-1}\frac{2X_1}{Z_0} \quad . \tag{IV-61}$$

The above procedure may also be generalized to the case of cavity impedances differing from Z_0. This would provide additional degrees of freedom to the designer, but it is unlikely that this would be needed in most cases of practical interest.

For narrow-band TEM network applications, the series capacitive coupled resonator network[2,3] shown in Fig. IV-8 is useful, particularly with printed circuits and microstrip, since grounding the strips is not

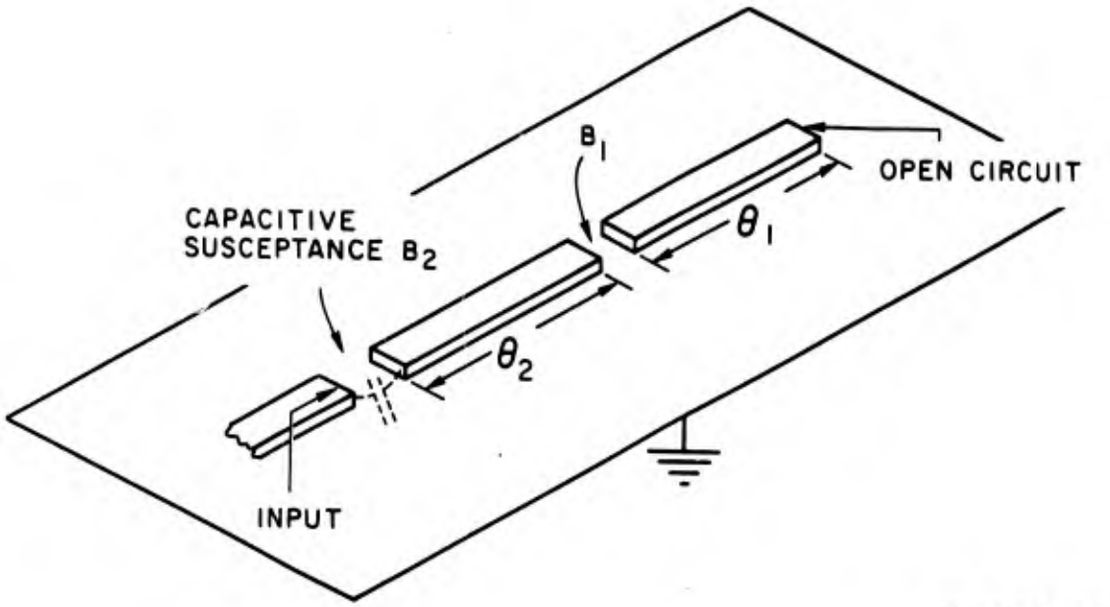

FIG. IV-8 CAPACITIVE COUPLED TWO-RESONATOR REACTANCE NETWORK FOR A SECOND-ORDER TEM TRANSMISSION-LINE EQUALIZER

required. (Also, here it is particularly attractive to replace the circulator by a quadrature hybrid, thereby making the entire circuit relatively compact and easily manufactured.*) This circuit is virtually

*Should the circulator be replaced by a single section 3-dB coupler, the effect on the phase and delay response would be equivalent to adding a C-section network to the equalizer and a fixed 90-degree phase shifter to the output. The effective σ of the C-section network would be $\sigma = \sqrt{1 - k^2}$, where k^2 is the power coupling coefficient of the directional coupler. Since k^2 must approximately equal 0.5 for a 3-dB coupler, σ would approximately equal 0.707. Consequently, the relative effects on the phase and time delay would be negligible in narrow-band applications.

the dual of the waveguide shunt inductive coupled cavity circuit just described. Therefore, Eqs. (IV-56) through (IV-61) and (IV-42)-(IV-43) apply provided X_i/Z_0 is replaced by B_i/Y_0, and K_i/Z_0 is replaced by J_i/Y_0. Here, B_i/Y_0 is the normalized series capacitive coupling susceptance and J_i/Y_0 is an ideal admittance inverter corresponding to the impedance inverter in the previous discussion.

Numerous other types of TEM reactance networks are possible by using various distributed coupled line configurations. For these cases exact correspondences can be established, and it is not necessary to expand the impedances about $t = \infty$. A simpler method is to first decide on the form of the coupled line network desired; then determine its open-wire-line equivalent. Next, synthesize the open-wire-line equivalent directly from the reactance function. Last, convert the open-wire-line circuit back to its coupled line form.

In order to obtain an idea of the approximate range of σ_o and $|t_o|$ to be expected for narrow-band equalizer design, Cohn's equations[13] for inductive coupled cavity filters were investigated with fractional bandwidth as a parameter. Although these equations are for filter design, they may be used as a rough guide in the present case.

In Cohn's equation the value of K_i/Z_0 is given by

$$\frac{K_i}{Z_0} = \frac{\pi}{2} w_\lambda \left(g_i g_{i+1}\right)^{-1/2} \qquad \text{(IV-62)}$$

where

$$w_\lambda = (\lambda_g/\lambda)_0^2 \, w = w/(1 - F_0^2)$$

w = fractional bandwidth

$(\lambda_g/\lambda)^2$ is the squared ratio of guide wavelength to freespace wavelength at band center

g_i is the normalized lumped element parameter of the low-pass filter whose attenuation response is being approximated.

An average value for $g_i g_{i+1}$ is typically about two, and the value of $F_0 = 0.6657$ used for computing Figs. IV-1 through IV-3 may be taken as representative. Substituting these values into Eq. (IV-62) gives

$$\frac{K_i}{Z_0} = \frac{\pi}{2}\left(\frac{1}{\sqrt{2}}\right)\frac{1}{0.556} \approx 2.0\ w \quad .$$

Let "narrow band" be defined as

$$w < 0.15 \quad ,$$

and for the purposes of this discussion let w be restricted to >0.01. Then

$$0.01 < \frac{K_i}{2\ Z_0} < 0.15$$

and

$$0.02 < \frac{K_i}{Z_0} < 0.30 \quad .$$

For C-sections

$$\frac{K_1}{Z_0} = \sqrt{2/\sigma}$$

and, therefore,

$$22 < \sigma < 5000 \quad , \qquad \text{(IV-63)}$$

approximately.

A similar analysis for the D-section shows

$$7 < |t_o| < 100 \qquad \text{(IV-64)}$$

and

$$4 < \sigma_o < |t_o| \quad . \qquad \text{(IV-65)}$$

E. Example Equalizer Designs

In the following example we require to equalize the differential time delay, given in Fig. IV-9 (solid line), to be flat to within a nanosecond over a 22 MHz band about band center. The filter being equalized had the following specifications:

(1) Nine resonator design

(2) Fractional bandwidth = $w = 0.00655$*

(3) Design based on a 0.01-dB Chebyshev ripple prototype filter[13]

(4) Center frequency = $f_0 = 5.960$ GHz

(5) Filter designed for WR-137 waveguide

(6) An unloaded Q of 5000 was assumed for the cavity resonators.

Although the shape of the differential delay curve appeared quite flat, suggesting that a D-section with "under-coupled response" would be most suitable, it was decided to first try to equalize with a single C-section because of its simpler design. Initially, several sets of data of unnormalized differential time delay were obtained for C-sections having σ's of 100, 200, and 400 in order to find the approximate range of σ needed. The data suggested that a σ of between 100 and perhaps 150 would probably be appropriate. Therefore, a second set of curves of delay was obtained for σ going from 100 to 150 in steps of 10. A quick scan of these data indicated that $\sigma = 120$ would probably provide the required equalization. This curve, with reversed sign, was then superimposed on Fig. IV-9, and is shown by the dark circle data points. The difference between the solid curve and the dark circle data points is the net differential time delay. It is seen that the maximum differential delay occurs about 7 MHz from f_0, and has an absolute magnitude

*A calculation of wf_0 gives the equiripple bandwidth as 39 MHz. This is approximately twice the bandwidth being equalized. The over-designed bandwidth was intentional in this case in order to ease the equalization requirements.

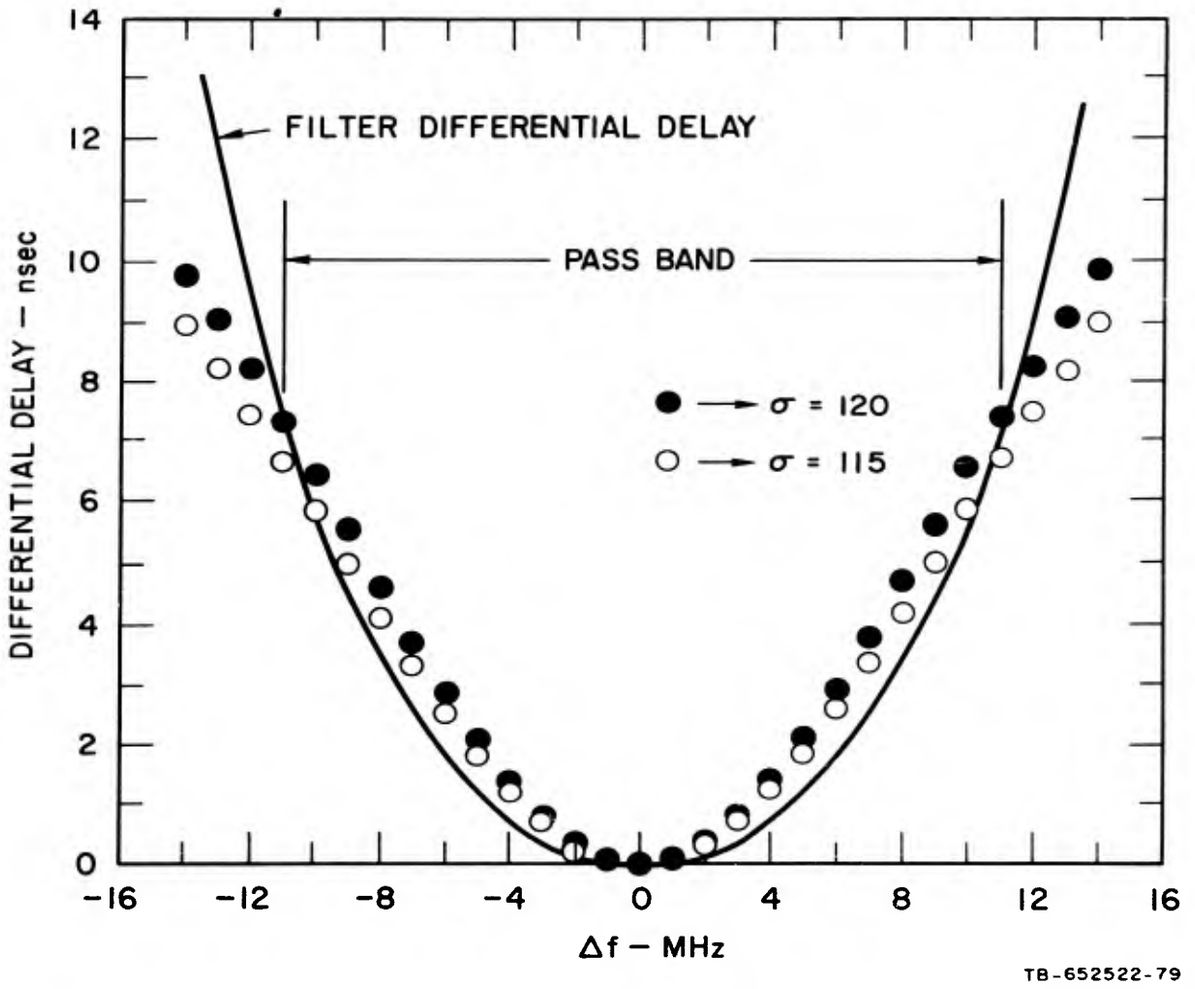

FIG. IV-9 DIFFERENTIAL DELAYS OF MICROWAVE FILTER AND C-SECTION EQUALIZERS FOR EXAMPLE IN TEXT

of 1.2 nanoseconds. This design, therefore, just misses meeting the specification.

A value of $\sigma = 115$ was then tried, and these data, with sign revised, are also plotted on Fig. IV-9 with open circles. It is now seen that this value of σ easily meets the delay specification across the 22-MHz band, and that further reductions in σ would deteriorate the equalization at the band edges. Hence, this equalization is about the best that can be done with a single-cavity equalizer.

Next, utilizing Eqs. (IV-60) and (IV-61), it is found that the required inductive coupled cavity equalizer calls for a normalized reactance of

$$\frac{X_1}{Z_0} = \frac{\sqrt{2\sigma}}{\sigma - 2} = \frac{\sqrt{230}}{113} = 0.134 \quad ,$$

and a cavity length at midband of

$$\theta_1 = 180° - \frac{1}{2} \tan^{-1} \frac{2X_1}{Z_0} = 180° - 7.5° = 172.5° \quad .$$

If still better equalization is required, it is necessary to go to higher-order equalizer networks. Figure IV-10 gives data of the equalization that could be obtained with a D-section (i.e., two-cavity) equalizer having a $\sigma_o = 102.0$ and $|t_o| = 112.0$. The solid curve in Fig. IV-10 is the differential time delay of the filter being equalized, and the dark circle data points are the negative of the differential time delay of the D-section equalizer. Again, the difference of the two sets of data is the net differential time delay of the system. It is seen that quite remarkable theoretical equalization has been obtained in this example with a two-cavity equalizer.

The electrical parameters of the two-cavity equalizer are calculated from σ_o and $|t_o|$ via Eqs. (IV-57), (IV-59), (IV-42), and (IV-43). The results are

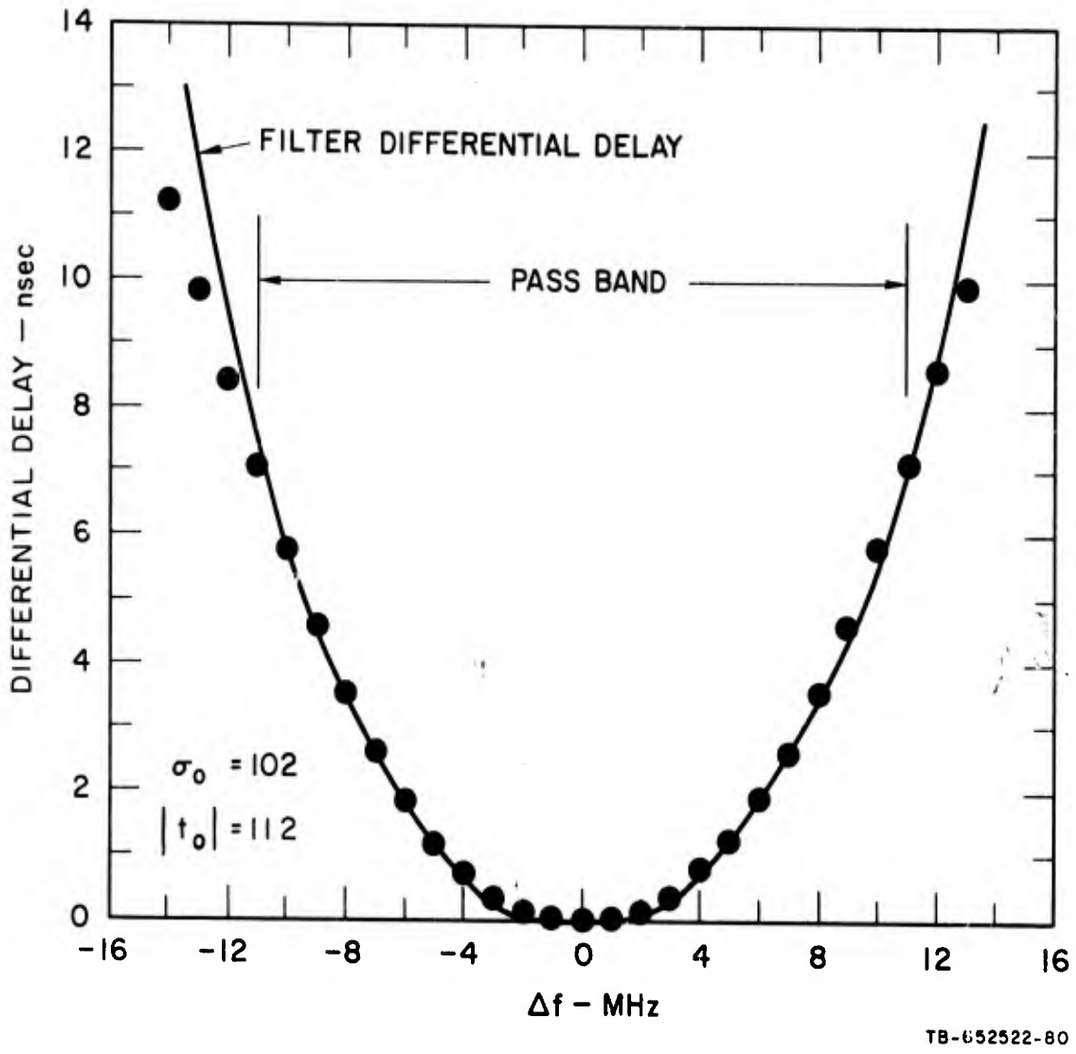

FIG. IV-10 DIFFERENTIAL DELAYS OF MICROWAVE FILTER AND D-SECTION EQUALIZER FOR EXAMPLE IN TEXT

$$X_2/Z_0 \approx 0.1803 \quad ,$$

$$X_1/Z_0 \approx 0.0178 \quad ,$$

$$\theta_2 \approx 169° \quad ,$$

$$\theta_1 \approx 179° \quad .$$

F. Equalizer Dissipation Loss

The effects of reactance network dissipation loss on the equalizer response were briefly considered. Dissipation loss may be accounted for by assigning a nonzero value to the real part of γ, and letting $t = \tanh \gamma L$ as θ varies. An expansion of t for complex γ is

$$t = \frac{\tanh \alpha L + i \tan \theta}{1 + i \tanh \alpha L \tan \theta} \quad , \qquad \text{(IV-66)}$$

where α is the real part of γ. Also, it can be shown that

$$\tanh \alpha L = \frac{\pi}{4Q_u} \frac{1}{1 - F_0^2} \quad , \qquad \text{(IV-67)}$$

with Q_u being the unloaded Q of the transmission line.

Using Eqs. (IV-66) and (IV-67), the general time delay expression given by Eq. (IV-20) was programmed on a digital computer. Data were computed for C- and D-sections for Q_u's of 2000 and 4000 with $F_0 = 0.6657$. The data showed that the normalized delay was virtually unaffected by the dissipation loss, and consequently, its effect on delay need not be considered in any but extremely lossy networks. A typical result of dissipation loss, corresponding to a D-section with $\sigma_o = 20$, $|t_o| = 40$, and $Q_u = 2000$, is given in Fig. IV-11. Comparison of this curve with the corresponding delay curve given in Fig. IV-2 shows marked similarity, and, in fact, the ratio of attenuation in dB to normalized delay varied only from 1.31×10^{-2} to 1.36×10^{-2} for $0.96 \leq F \leq 1.00$. Hence, one may take the dissipation loss to be

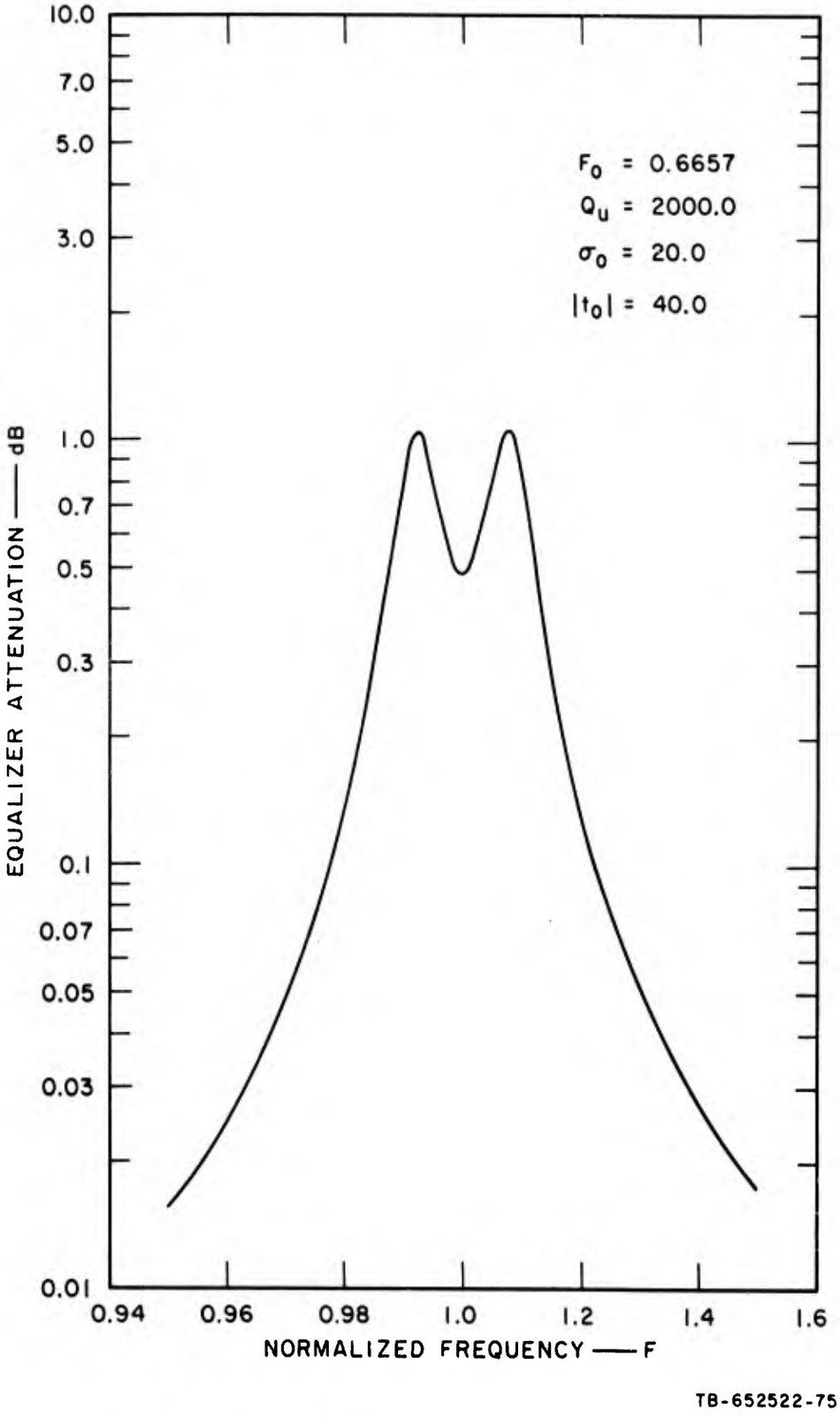

FIG. IV-11 DISSIPATION LOSS OF A MICROWAVE D-SECTION EQUALIZER

proportional to the delay, a result previously noted in filter theory.[14] The proportionality constant is most easily calculated at band center, where $t = 4/\{\pi Q_u(1 - F_0^2)\}$. This value may be substituted in Eq. (IV-1) to give the loss at $F = 1$, and the corresponding normalized time delay can be calculated from Eq. (IV-20), or from the equations in Table IV for low-order networks by letting $\Omega \to \infty$.

The following expressions are good approximations to the midband loss of C-section and D-section equalizers.

For C-sections:

$$\text{Loss} = \frac{4.343\pi}{1 - F_0^2} \frac{\sigma}{Q_u} \text{ dB} \quad . \tag{IV-68}$$

For D-sections:

$$\text{Loss} = \frac{4.343\pi}{1 - F_0^2} \frac{2\sigma_o}{Q_u} \text{ dB} \quad . \tag{IV-69}$$

The formula for the general n-section equalizer is

$$\text{Loss} = \frac{4.343\pi}{\left[1 - F_0^2\right] Q_u} \Sigma \text{ Re [all transmission zeros]} \quad . \tag{IV-70}$$

REFERENCES

1. R. Beatty, "A Differential Microwave Phase Shifter," IEEE Trans. on Microwave Theory and Techniques, Vol. MIT-12, p. 250 (March 1964).

2. K. Woo, "An Adjustable Microwave Delay Equalizer," IEEE Trans. on Microwave Theory and Techniques, Vol. MTT-13, pp. 224-233 (March 1965).

3. T. A. Abele and H. C. Wang, "An Adjustable Narrow Band Microwave Delay Equalizer," IEEE Trans. on Microwave Theory and Techniques, Vol. MTT-15, pp. 566-574 (October 1967).

4. B. M. Schiffman, "A New Class of Broad Band Microwave 90 Degree Phase Shifters," IEEE Trans. on Microwave Theory and Techniques, Vol. MTT-6, pp. 232-237 (April 1958).

5. W. J. D. Steenaart, "The Synthesis of Coupled Transmission Line All-Pass Networks in Cascades of 1 to n," IEEE Trans. on Microwave Theory and Techniques, Vol. MTT-11, pp. 23-29 (January 1963).

6. P. Shelton and J. Mosko, "Synthesis and Design of Wide-Band Equal Ripple TEM Directional Couplers and Fixed Phase Shifters," IEEE Trans. on Microwave Theory and Techniques, Vol. MTT-14, pp. 462-474 (October 1966).

7. E. G. Cristal, "Analysis and Exact Synthesis of Cascaded Commensurate Transmission Line C-Section All-Pass Networks," IEEE Trans. on Microwave Theory and Techniques, Vol. MTT-14, pp. 285-292 (June 1966) (and also Addendum to this article appearing in October 1966 issue of MTT-14).

8. J. O. Scanlan and J. D. Rhodes, "Microwave All-Pass Networks," IEEE Trans. on Microwave Theory and Techniques, Vol. MTT-16, pp. 62-80 (February 1968).

9. H. W. Bode, Network Analysis and Feedback Amplifier Design (D. Van Nostrand, Inc., New York, 1945).

10. D. Merlo, "Development of Group-Delay Equalizers for 4GC," Proc. IEE (London), Vol. 112, pp. 289-295 (February 1965).

11. P. I. Richards, "Resistor Transmission Line Circuits," Proc. IRE, Vol. 36, pp. 217-220 (February 1948).

12. E. A. Guillemin, Synthesis of Passive Networks, Chap. 14 (John Wiley & Sons, New York, 1957).

13. S. B. Cohn, "Direct Coupled-Resonator Filters," Proc. IRE, Vol. 45, pp. 187-196 (February 1957).

14. L. Young, "Analysis of a Transmission Cavity Wavemeter," IEEE Trans. on Microwave Theory and Techniques, Vol. MTT-8, pp. 436-439 (July 1960).

V ACTIVE FILTERS FOR UHF AND MICROWAVE FREQUENCIES

As the size of low-power microwave circuits becomes smaller through the use of integrated-circuit techniques, the importance increases of miniaturizing filters, matching networks, multiplexers, and other normally passive components. The straightforward approach of simply using smaller parts and dielectric loading to reduce the size of conventional filters leads to lower element Q, but in many filter applications high Q's simply cannot be sacrificed. Therefore, in the interest of reducing filter size we are moved to seek techniques that trade size for something other than Q. One worthwhile trade-off would be size for dynamic range, which is the advantage offered by active filters.

Design techniques for active filters below about 1 MHz are well established. Generally, low-frequency active filters employ feedback circuits consisting of transistor stages that individually have either 0° or 180° phase shift. In one common technique, the active network is used as an impedance inverter or gyrator[1-5] with a capacitive load to yield a virtual inductance as shown in Fig. V-1. However, at higher frequencies where the phase shift of a transistor is not constant, the

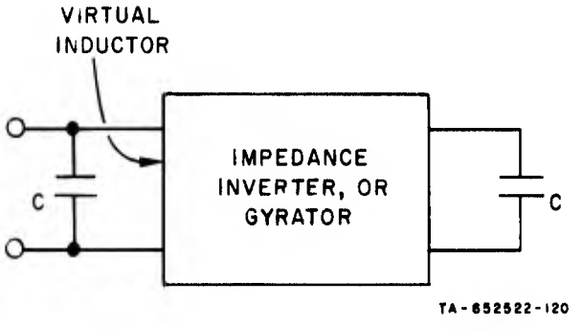

FIG. V-1 ACTIVE RESONATOR SUITABLE FOR LOW-FREQUENCY APPLICATIONS

direct application of low-frequency active-filter techniques is less promising. Therefore, at UHF and microwave frequencies, an alternative

approach to active filters has been pursued and is the subject of this section. The new method takes advantage of (rather than suffers from) the mechanism producing high-frequency phase shift in a transistor. With this approach, a single transistor can be used as an energy storage element and can produce very high-Q inductance without relying on external feedback mechanisms. The fact that the phase shift and energy storage are internal to the transistor means that it is relatively insensitive to external circuit effects, which are often a source of difficulty in conventional active filters.

A. The Internal Inductive Properties of a Transistor

While the inductive effect in transistors has been known for many years,[6-12] it has only recently received serious attention at high frequencies.[13,14] The inductive effect is associated with the transit-time properties of the transistor, which can easily be explained from the T-equivalent circuit of the transistor. Consider the inverted common-collector configuration shown in Fig. V-2(a). If an impedance Z is present in the base, the input impedance is

$$Z' = (1 - \alpha)Z + Z_e \qquad \text{(V-1)}$$

where α is the short-circuit current gain and Z_e is the emitter impedance.

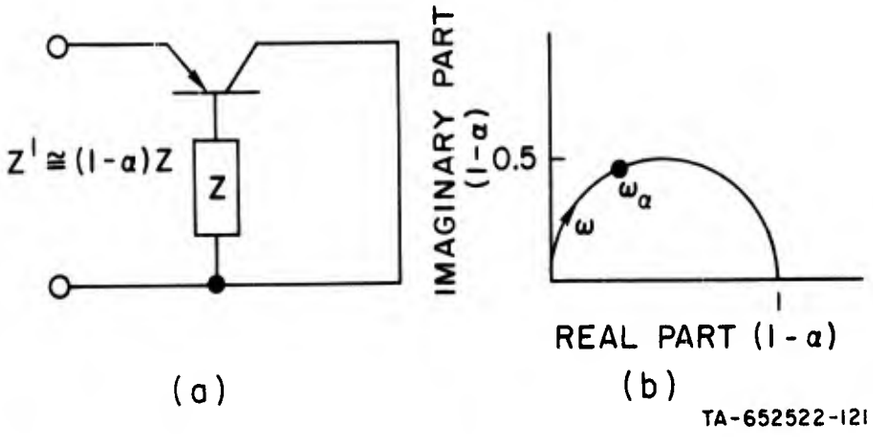

FIG. V-2 INDUCTIVE TRANSISTOR CIRCUIT SUITABLE FOR MICROWAVE APPLICATIONS

Transit-time effects are reflected by the frequency dependence of α and Z_e expressed as follows:

$$Z_e = r_e + \frac{1}{j\omega C_e} \qquad \text{(V-2a)}$$

$$\alpha = \frac{\alpha_o e^{-jMf/f_\alpha}}{1 + jf/f_\alpha} \qquad \text{(V-2b)}$$

where

f_α = the alpha-cutoff frequency

M = the drift parameter

$r_e = \frac{kT}{qI_e}$

I_e = the dc emitter current.

Even though associated physically with transit-time phenomena, the effective series capacity C_e is large and is not important to the ensuing discussion. The important transit-time effects arise from the complex nature of α as given in Eq. (V-2b). The drift parameter M accounts for the possible existence of an electric field within the base region of the transistor. Fields that aid the normal diffusion carrier flow in the base will increase both M and f_α. In the absence of a drift field, $M = 0.22$.[15]

1. Impedance Rotation

A simplified plot of the quantity $(1 - \alpha)$ in Fig. V-2(b) shows that it is essentially an imaginary quantity over a large frequency range. More precisely, the imaginary part of $(1 - \alpha)$ exceeds the real part over the range

$$\frac{1 - \alpha_o}{\alpha_o (1 + M)} < \frac{f}{f_\alpha} < \frac{\alpha_o (1 + M)}{1 + \alpha_o M + \alpha_o M^2} \quad . \qquad \text{(V-3)}$$

Therefore, because of the term $1 - \alpha$ in Eq. (V-1), the inverted common-collector circuit in Fig. V-2(a) is basically an impedance rotator, which provides the basis for the simulated inductive effect. If Z is a

resistor (in the base), a virtual inductance is seen at the emitter. Or, if Z is an inductance, a virtual negative resistance appears at the emitter. However, any virtual impedance presented at the emitter will be in series with Z_e which reduces essentially to the small current dependent resistance r_e. The resistive component of Z_e will degrade the Q of any virtual inductance derived from the rotation property of the inverted common-collector circuit, as previously noted by Lindmayer and North.[12] If the base circuit impedance is simply the resistance r_b, the virtual inductance appearing in the emitter will have a Q limited approximately to $(f/f_\alpha)(r_b/r_e)$. Therefore, some modification of the technique of transit-time impedance rotation is needed to obtain high Q.

2. The Useful Influence of Parasitics on Inductive Transistor Effects

In any high-frequency transistor network, parasitic effects tend to have a major influence on the ultimate circuit performance. As noted above, when high-Q inductances are being synthesized with transit-time effects, the emitter resistance r_e constitutes an important parasitic. Other more common transistor parasitics are interelectrode capacitances, package capacitances, and package inductances. A full discussion of the effects of package parasitics in the inverted common-collector configuration is given in Appendix B, but for simplicity the circuit in Fig. V-3 is representative of the major parasitic influences. Grounding the collector allows the collector-base capacity to be lumped into the base capacity C_B. Similarly, collector-emitter parasitic capacity becomes part of the input capacity C_e', and appears in shunt with the inductance being synthesized. The base inductance L_b includes the effect of the base lead and will be shown to have an important usefulness in obtaining high-Q inductance. However, the Q of the base circuit in this application need only be low, so the use of a small inductive effect in the base to produce high-Q inductance in the emitter is a practical approach to the problem. Regarding stability, the evidence to date (as presented in Sec. V-D-2) is that high-Q inductances can be realized at UHF and microwave frequencies with sufficient stability for resonator application in both narrow- and wide-band filters.

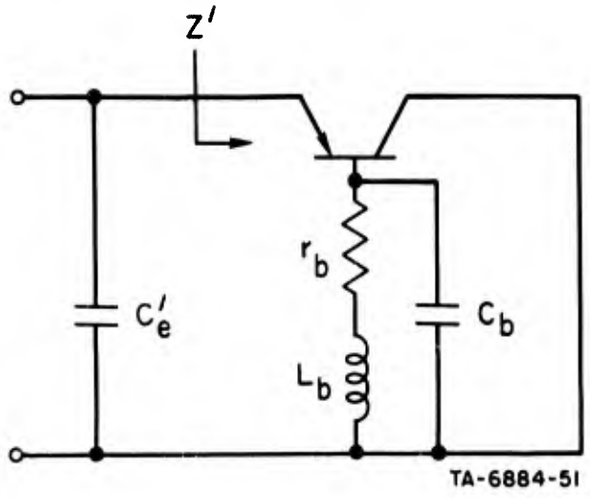

FIG. V-3 INVERTED COMMON-COLLECTOR CIRCUIT FOR REALIZING STABLE, HIGH-Q INDUCTANCE AT MICROWAVE FREQUENCIES

B. Analysis of a High-Q Inductive Transistor Circuit

As noted previously, the impedance rotation property of the inverted common-collector transistor is not sufficient to transform a base resistance into a high-Q inductance, because of the series emitter resistance. The inevitable presence of reactive parasitics in the base also means that analysis of a purely resistive base circuit is only an academic exercise. Including a small series inductance in the base (which arises normally, due to the base lead) produces a virtual negative resistance in the emitter which can be chosen to balance r_e and hence to yield inductance with essentially infinite Q. Therefore, with some prerotation of the base impedance vector, sufficient negative resistance results in the emitter to balance r_e and to allow high-Q inductance to be synthesized by the transit-time rotation property of $(1 - \alpha)$ in Eq. (V-1).

In practice, the necessary base inductance can be estimated from the formulas that will be given later in this section, and the base lead cut approximately to length. Obtaining an exact value of negative resistance is not required, because adjustment of the emitter current will control r_e. With inductance in the base circuit, the emitter resistance can be adjusted to bring the total resistance in the emitter circuit close to zero, which produces the high-Q virtual inductance needed.

Base inductance is not the only parasitic that must be considered. As shown in Fig. V-3, the collector-base capacity of the transistor plus other parasitics give rise to the base capacity C_b. In addition, as noted further in Sec. V-D-3, an external variable capacitor in the position of C_b in Fig. V-3 is useful for tuning. At higher frequencies, the base capacity tends to offset the effect of base inductance, and it will be shown that this too produces a useful effect.

An analysis of the circuit in Fig. V-3 is aided by defining two parameters: A is the ratio of the alpha-cutoff frequency to the self-resonant frequency of the base circuit

$$A = \frac{\omega_\alpha}{\omega_o} \quad , \tag{V-4a}$$

where

$$\omega_o = \frac{1}{\sqrt{L_b C_b}}$$

and Q_α is the Q of the base circuit at the alpha-cutoff frequency

$$Q_\alpha = \frac{\omega_\alpha L_b}{r_b} \tag{V-4b}$$

where r_b denotes the total resistance of the base circuit, including any externally added resistance. The input impedance at the emitter then becomes

$$\frac{Z'}{r_b} \cong \frac{r_e}{r_b} + (1 + M)\left\{ \frac{x^2\left[1 - Q_\alpha + \frac{A^2}{Q_\alpha}\right] + x^4 A^2 Q_\alpha}{(1 + x^2)\left[\left(1 - A^2x^2\right)^2 + \left(\frac{xA^2}{Q_\alpha}\right)^2\right]} + j \frac{x\left[1 + x^2\left(Q_\alpha - \frac{A^2}{Q_\alpha}\right) - x^4 A^2 Q_\alpha\right]}{(1 + x^2)\left[\left(1 - A^2x^2\right)^2 + \left(\frac{xA^2}{Q_\alpha}\right)^2\right]} \right\} \tag{V-5}$$

where $x = \omega/\omega_\alpha$ and where the approximations $\alpha_o = 1$ and $e^{-jMx} \approx 1 - jMx$ have been used.

The first term in Eq. (V-5) is the normalized emitter resistance, which is controlled by the transistor current. The second and third terms are the impedance components reflected from the base. For a typical case, with $Q_{\alpha'} = 1.5$, the reflected resistance and reactance terms are plotted in Fig. V-4 with A as a parameter. It is noteworthy that the input reactance is inductive, and that the reflected resistance is negative over a considerable range of frequency. It is of major interest, however, that the reflected resistance has a minimum in the negative resistance region. The negative resistance minimum is due to the capacity C_b in the base circuit. Raising the base capacity (which includes the collector-base capacity of the transistor) increases A, which causes the negative resistance minimum to move to lower frequencies. In the absence of any base capacity (A = 0), a negative resistance minimum will not appear. Therefore, the presence of capacity in the base circuit has a useful influence on circuit stability. If the transistor is used as a high-Q inductor at frequencies near the negative resistance minimum, the tendency for the circuit to oscillate at some other frequency will be avoided.

A practical operating technique, based on the curves in Fig. V-4, is to position the negative resistance minimum close to the desired frequency of operation, and then to adjust the transistor current so that the emitter resistance r_e just cancels the negative reflected resistance. The result will be that an inductance appears at the emitter terminal of the transistor with essentially infinite Q. Evidence is offered in Sec. V-D-2 that adequate stability can be maintained by this technique.

Experimental verification of the impedance predictions of Fig. V-4 is given in Fig. V-5. Excluding the emitter resistance, the input resistance reaches the extreme negative value of -8 ohms between 300 and 350 MHz. Therefore, with the transistor current adjusted to 3.25 mA to yield an emitter resistance of 8 ohms, a very high-Q inductance was realized between the above-noted frequencies. The Q-stability of the virtual inductance depends mainly upon the stability of the dc current.

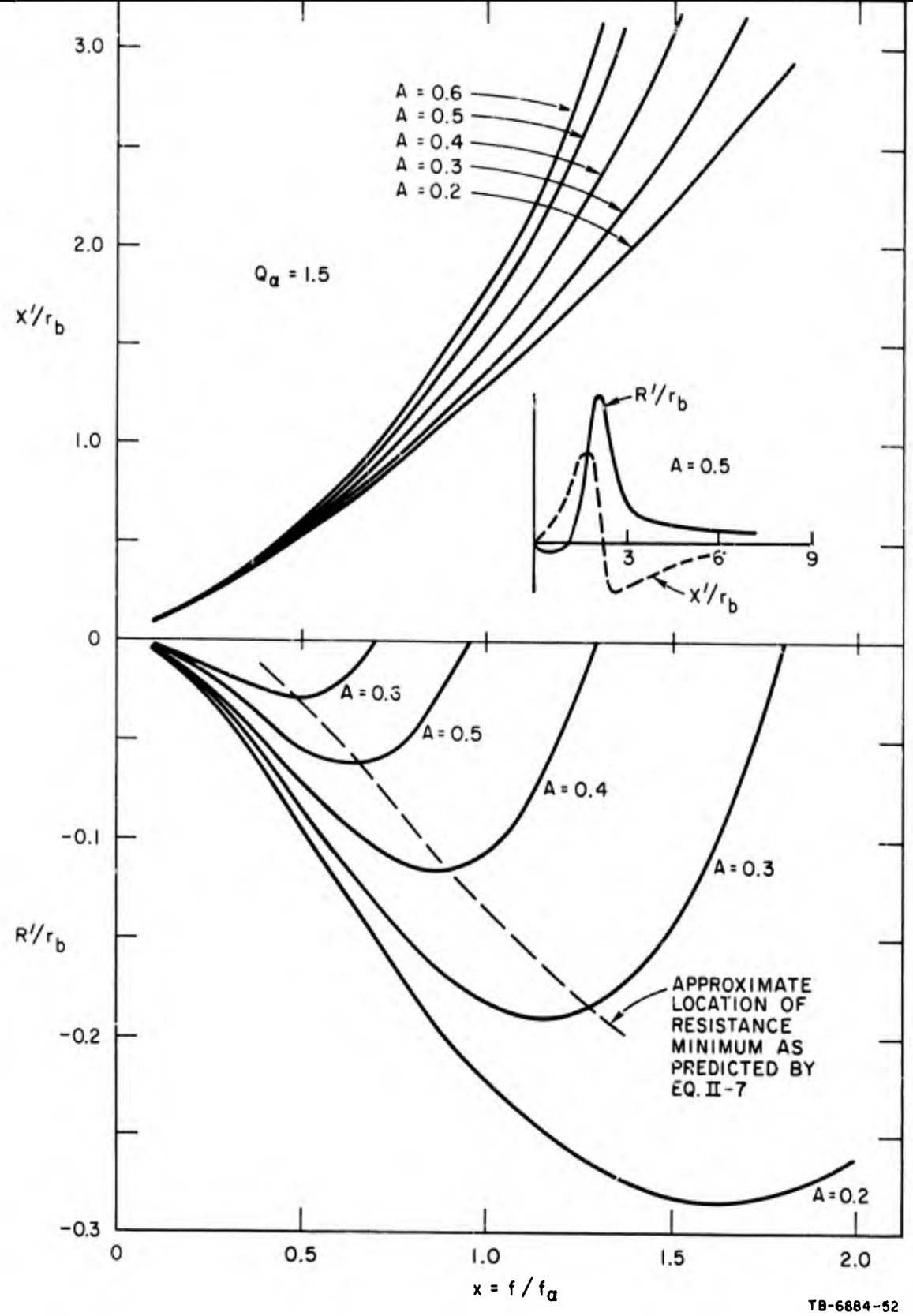

FIG. V-4 REFLECTED REACTANCE AND RESISTANCE COMPONENTS OF Z' IN FIG. V-3, EXCLUDING THE CONTRIBUTION OF r_e. The insert shows the general function shape over a full frequency range

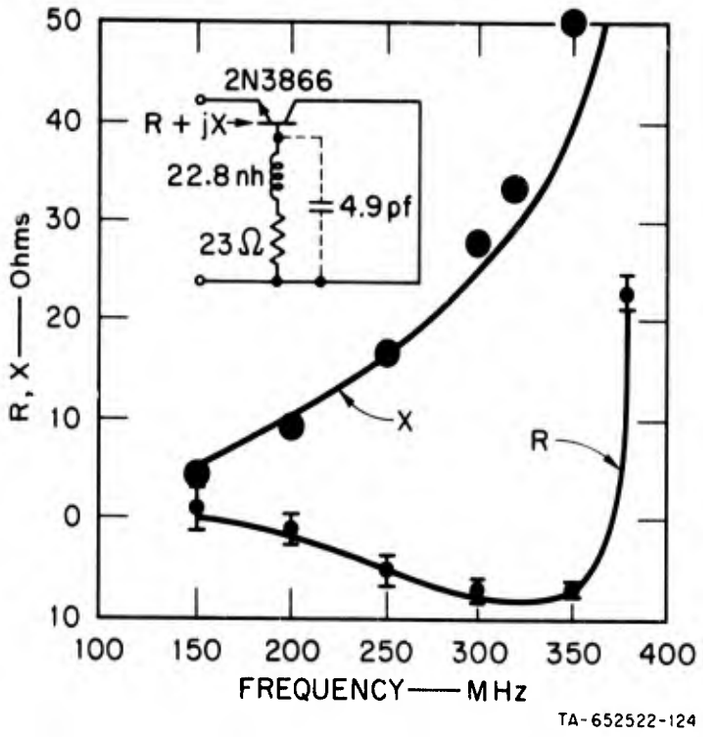

FIG. V-5 MEASURED EMITTER IMPEDANCE OF 2N3866 TRANSISTOR IN THE INVERTED COMMON-COLLECTOR CONFIGURATION, EXCLUDING THE CONTRIBUTION OF r_e

It is generally possible to choose the dc current in a range where α_o and ω_α are fairly constant and where only r_e changes with current.

The relative frequency x_M of the negative resistance minimum is predicted to good accuracy by the following expression:

$$x_M = \left[\frac{\sqrt{1 - \beta(1 - \gamma)} - 1}{\Delta(1 - \gamma)}\right]^{1/2} \qquad \text{(V-6)}$$

where

$$\Delta = 1 - 2A^2 + A^4$$

$$\beta = \Delta\left(\frac{1 - Q_\alpha}{A^2 Q_\alpha} + \frac{1}{Q_\alpha^2}\right)$$

$$\gamma = \frac{\beta}{\Delta^2}\left[A^4\left(1 + \frac{1}{Q_\alpha}\right)^2 - 2A^2\right] \quad .$$

Up to the alpha-cutoff frequency, Eq. (V-6) reduced approximately to

$$x_M \approx \sqrt{\frac{-\beta}{2\Delta}} \quad ; \quad x_M < 1 \tag{V-7}$$

which is plotted in Fig. V-4. The virtual inductance associated with the negative resistance minimum can be calculated from Eq. (V-5), but it is given approximately by

$$L_e \simeq \frac{r_b(1 + M)}{\omega_\alpha} \cdot \frac{1 + 2Q_\alpha^2 x_M^2}{1 + 2Q_\alpha x_M^2} \quad . \tag{V-8}$$

Further study of Eqs. (V-6) and (V-7) shows that Q_α must be greater than unity for negative resistance to appear, and that x_M is a monotonically increasing function of Q_α/A^2. From Eq. (V-4) it follows that

$$\frac{Q_\alpha}{A^2} = \frac{\alpha_o \omega_\alpha}{\omega_\alpha r_b C_b} = 4\left(\frac{\omega_{max}}{\omega_\alpha}\right)^2 \tag{V-9}$$

where ω_{max} is a fundamental transistor parameter, the maximum frequency of oscillation,

$$\omega_{max} = \sqrt{\frac{\alpha_o \omega_\alpha}{4 r_b C_b}} \quad . \tag{V-10}$$

In the sense in which Eq. (V-9) is written, ω_{max} includes effects of external base resistance and capacity. The upper value of ω_{max} arises when r_b and C_b consist of only the intrinsic transistor parasitics, the base resistance (r_b'), and the collector-base capacity (C_{cb}). Therefore, the transistor imposes an upper limit on Q_α/A^2, and hence on the frequency $(x_M \omega_\alpha)$ at which a negative resistance extremum can be obtained. For the configuration under study, the negative resistance extremum can occur up to and beyond the alpha-cutoff frequency.

Figure V-6 shows the results of a calculation of the negative resistance extremum as a function of the ω_{max} of the transistor and circuit. In a well-designed RF transistor, the intrinsic ω_{max} will exceed ω_α by a factor of two or more, which shows that stable high-Q inductance can be realized above the alpha-cutoff frequency. The second curve

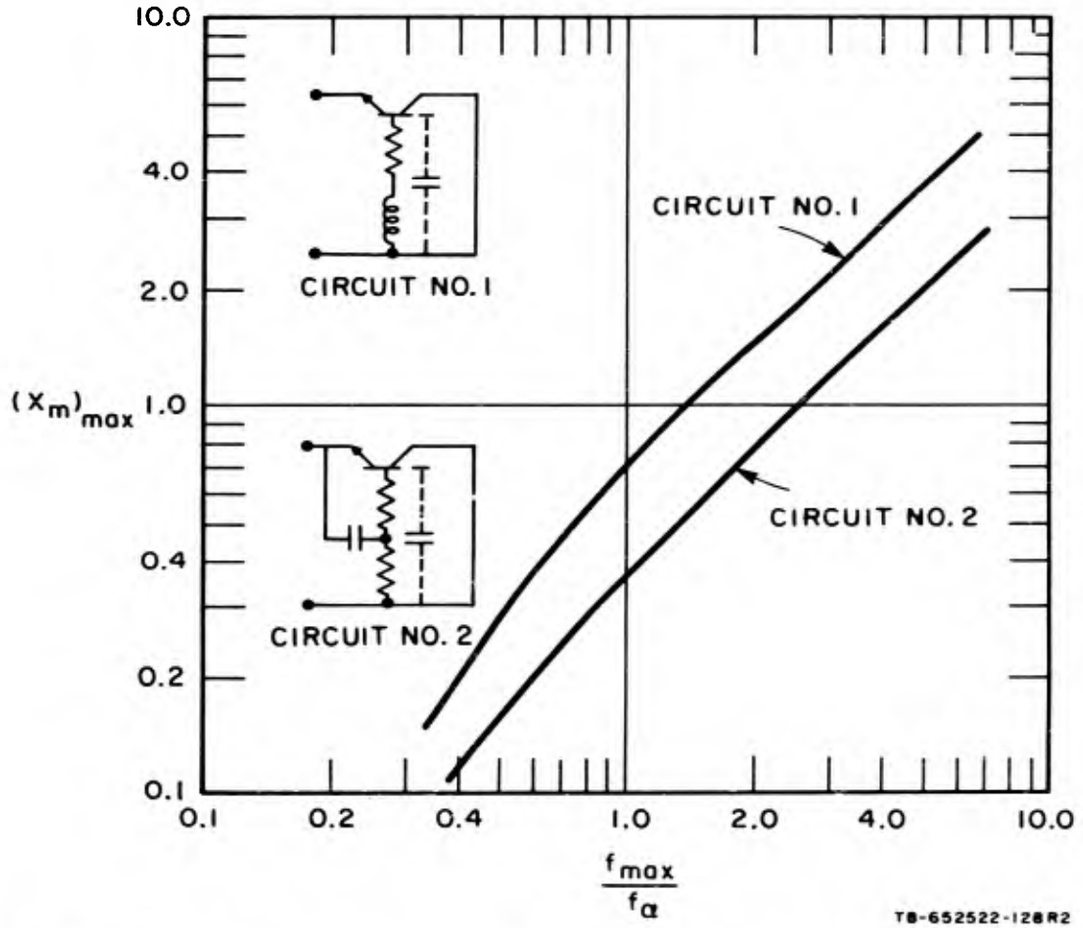

FIG. V-6 THEORETICAL PREDICTION OF THE MAXIMUM OBTAINABLE x_m FOR TWO GROUNDED COLLECTOR CONFIGURATIONS AS A FUNCTION OF $f_{max}/f\alpha$ OF THE TRANSISTOR USED

shown in Fig. V-6 applies to an alternate method for obtaining impedance prerotation in the base circuit. In the manner proposed by Jindal,[16] an RC phase shifting network can be used to obtain negative input resistance. It is the authors' understanding that the Jindal circuit has never been considered for microwave applications, but the analysis in Fig. V-6 shows that high-frequency applications are possible, although the frequency range is higher for the circuit in Fig. V-3, which employs a small inductive effect in the base. However, the importance of the Jindal circuit will increase if and when monolithic integrated circuits become a serious reality at microwave frequencies.

C. Physical Model of the Inductive Transistor Effect

In the previous discussion, the inductive effect in a transistor has been treated from the electronic-circuit viewpoint; i.e., the inverted common-collector circuit is basically an impedance rotator which produces approximately a 90-degree rotation in transforming the base impedance to the emitter. The 90-degree impedance rotation property is a direct result of the dominant imaginary part (at higher frequencies) of the quantity $(1 - \alpha)$. The mechanism causing $(1 - \alpha)$ to be strongly imaginary can alternately be described from the physical viewpoint.

Figure V-7 shows the physical cross section of a typical RF transistor, which is assumed to be npn so that the current flow in the normal

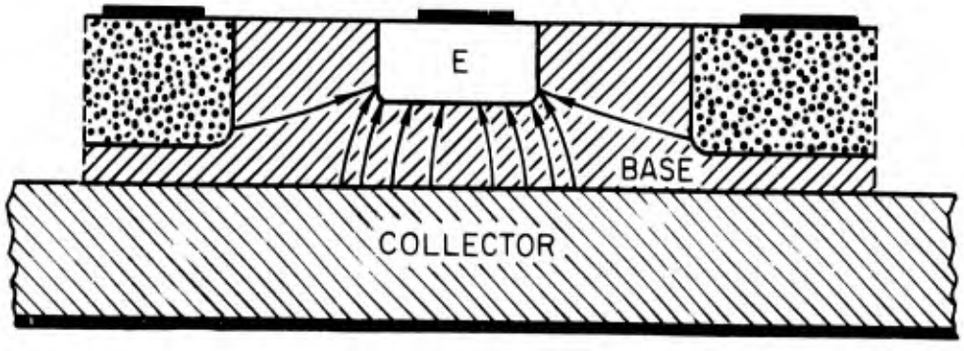

TRANSISTOR CURRENT FLOW

TA-652522-125

FIG. V-7 CROSS SECTION OF A TYPICAL MICROWAVE TRANSISTOR

bias condition will be from collector to emitter. There will also be a small base current as indicated in Fig. V-7. The ratio of these two currents determines the alpha of the transistor. The important difference between these currents, however, is that collector current flows mainly by diffusion while the base current flows mainly by conduction. Because the carrier velocities are considerably different for these two flow mechanisms, a relative phase shift approaching 90 degrees arises which produces the 90-degree base-emitter impedance rotation property. Therefore, the diffusion delay of the carrier flow from collector to emitter is an internal energy storage mechanism suitable for active-filter applications. It can be observed that an internal energy storage mechanism leads to simple active-filter circuits, since only one active element is required per section and external feedback networks are not required.

D. Active Microwave Filters Using Inductive Transistors

In the previous sections, a technique has been described for realizing high-Q inductance with a single transistor. Inductors of this type can be used, together with capacitors, to realize compact resonators and filters. Several narrow-bandwidth filters have been built at UHF to demonstrate this principle and to show the considerable advantage in both size and performance over their passive counterparts. Passive UHF filters require quarter-wavelength stubs of large cross section to yield low insertion loss, and are therefore bulky. The basic circuit used is the capacitively coupled bandpass filter shown in Fig. V-8. An experimental version of this filter, consisting of two active resonators for use around 500 MHz is shown in Fig. V-9.

The end-coupling capacitors are visible near the connectors in Fig. V-9, on the left and right sides of the package. The center-coupling capacitor passes through the shield separating the two resonators. The two transistors are held in place by small blocks, one of which is removed in the photo to expose the base circuit lead, which enters a hole containing the external base resistor (10 ohms in this case). The length of the base lead determines the base circuit inductance used to

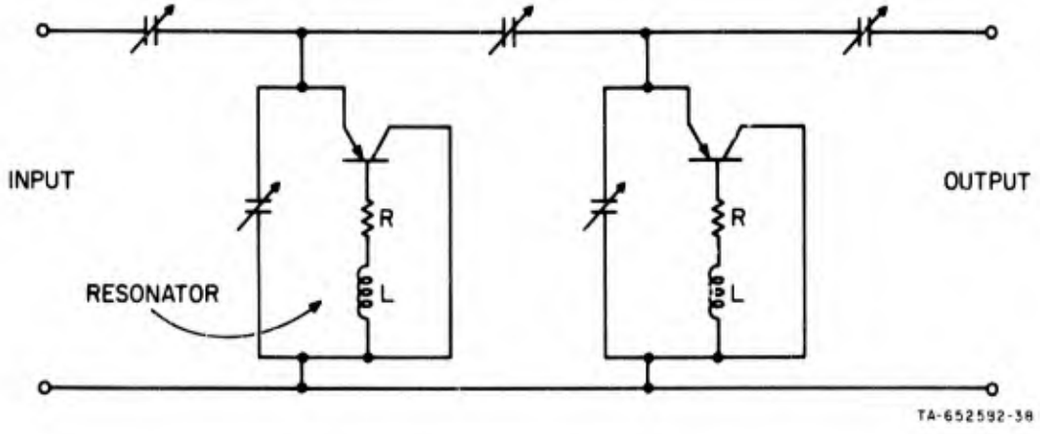

FIG. V-8 BANDPASS FILTER CONFIGURATION USED FOR ACTIVE RESONATOR TESTING

produce the negative input resistance required for Q multiplication. The visible coils are RF chokes, which could be reduced in size considerably in future designs. A three-resonator filter, similar in form to that shown in Fig. V-9, has also been built and tested. Its performance is similar to that obtained for the two-resonator filter, except that proportionally higher stopband attenuation was obtained.

1. Insertion Loss and Pass-Band Shape of Active Bandpass Filters

A pass band obtained with the two-resonator active filter is shown in Fig. V-10. Zero insertion loss was measured, which implies infinite unloaded Q in each resonator. The filter bandwidth was approximately 2 percent at 500 MHz, but it could be tuned to yield other (both wider and narrower) bandwidths. A rather narrow-bandwidth filter was chosen for initial tests because low-loss, narrow-bandwidth filters are difficult to realize with passive elements. Bandpass filters realized with low-Q elements not only have high insertion loss but also have rounded pass-band corners. The latter defect is particularly serious in multiplexers, where adjacent channels must be sharply defined.

By shortening the length of the base leads in the circuit in Fig. V-9, a stable resonator was also obtained at 615 MHz with the measured performance shown in Fig. V-11. Also shown in the latter figure is the theoretical response based on the standard low-pass to bandpass mapping function[17] and a 0.1 dB ripple, low-pass prototype.

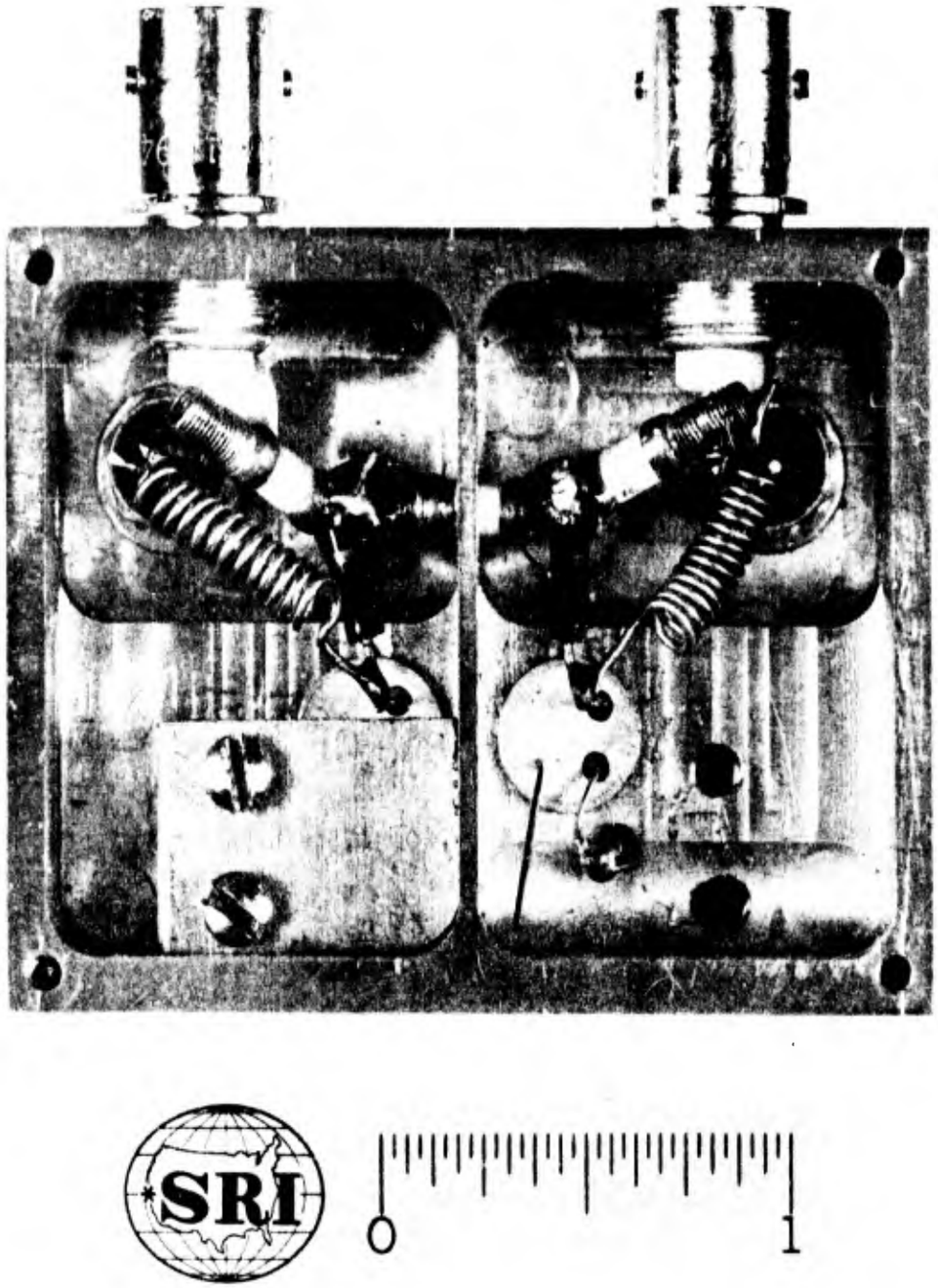

FIG. V-9 TWO-RESONATOR, ACTIVE BANDPASS FILTER FOR UHF APPLICATION. The transistors are (Fairchild) 2N3866. The supporting block for the right-hand transistor has been removed to show base circuit.

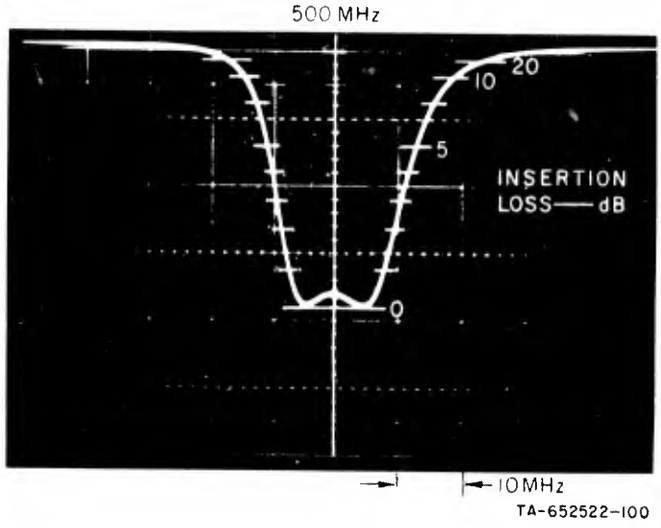

FIG. V-10 TYPICAL PASS BAND OBTAINED WITH THE FILTEF IN FIG. V-9. The bandwidth is about 2 percent at 500 MHz for the case shown.

Evidence that wider bandwidth filters can be realized with transistor elements is offered in Fig. V-12, which shows the computed performance of three five-resonator active bandpass filters with 1 percent, 5 percent, and 10 percent bandwidths at a design center frequency of 500 MHz. An inductive transistor configuration was used with a base circuit Q of 0.75 in the pass band (Q = 1.5), and an alpha-cutoff frequency of 1 GHz. The transistor circuit was chosen to give infinite resonator Q at midband which resulted in Q = 420 at ±5 percent of the 500 MHz midband frequency. In the stopband, at 500 ± 100 MHz, the resonator Q drops to about 110, but the stopband insertion loss is still very high with no serious degradation of stopband shape.

2. Stability of High-Q Active Resonators

In considering the stability of resonators made with active inductors having very high Q, contrast must be made between the loaded and the unloaded Q in the filter circuit. Active resonators with infinite unloaded Q can be stable in a filter circuit, since each resonator is loaded to some extent by external sources and loads. Instability occurs when the poles of the complete filter cross the imaginary axis.

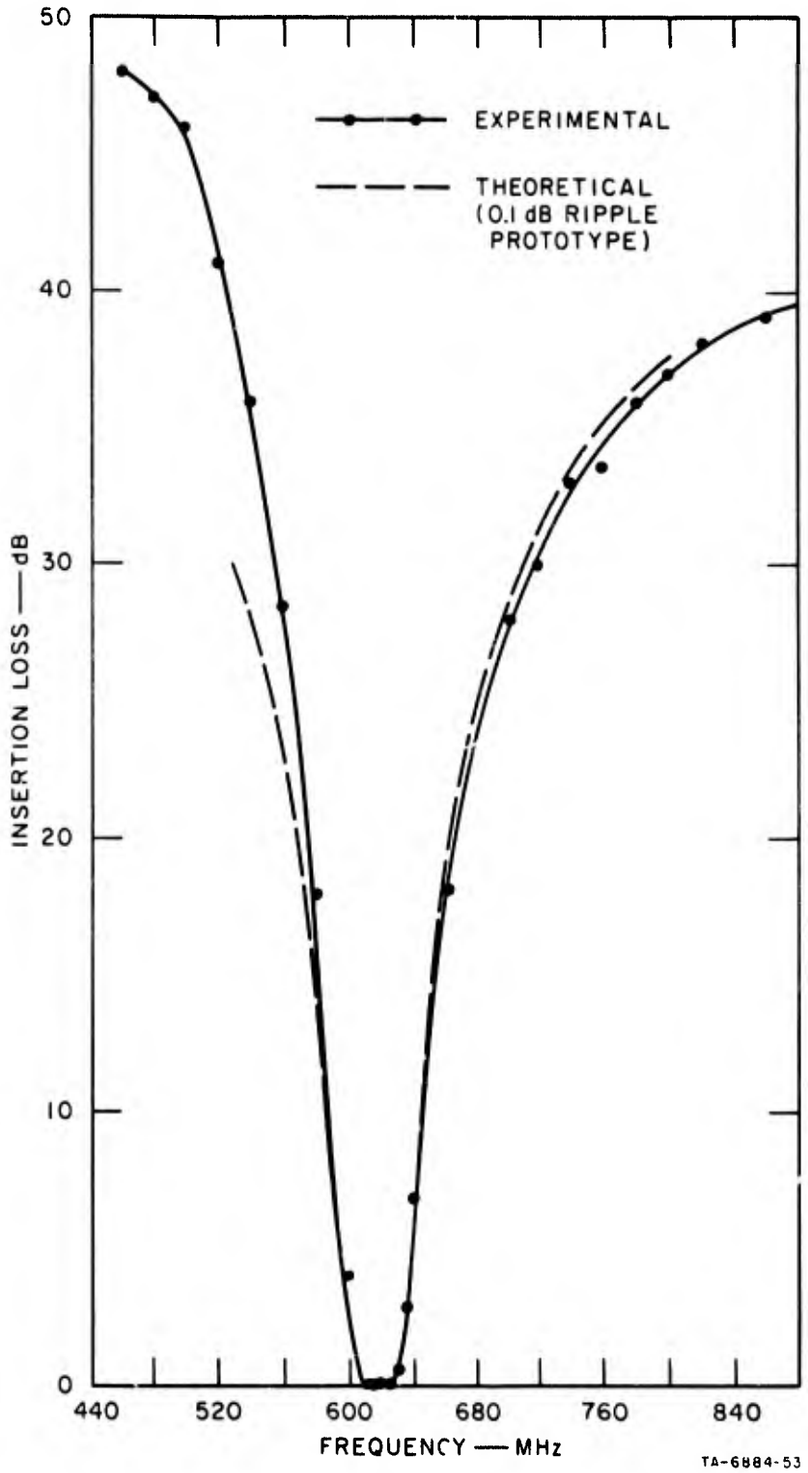

FIG. V-11 COMPUTED RESPONSE OF THREE FIVE-RESONATOR TRANSISTOR FILTERS.
Transistor alpha-cutoff frequency of 1 GHz assumed

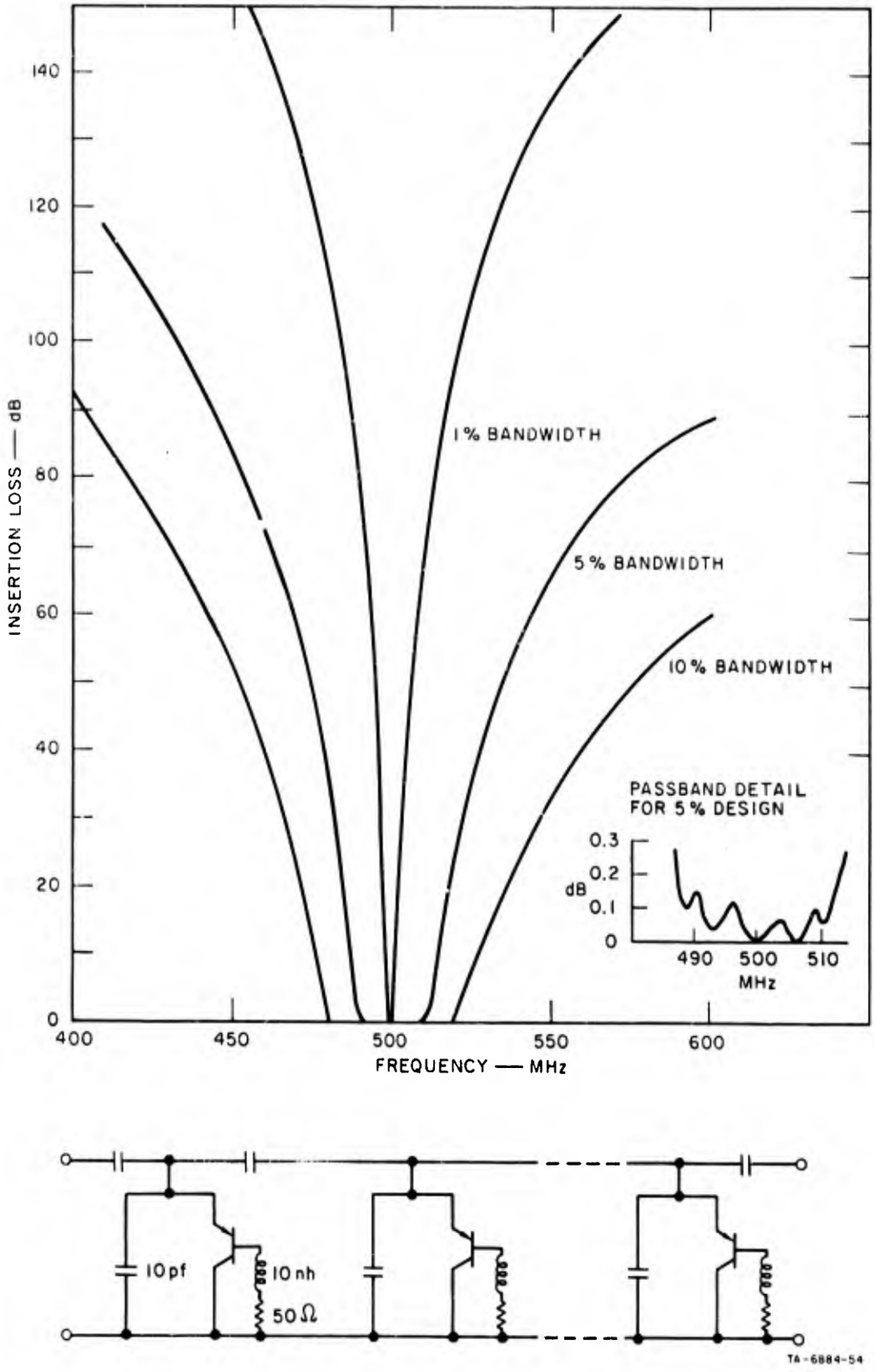

FIG. V-12 PASS BAND SHAPE OF THE TWO-RESONATOR ACTIVE FILTER AT 620 MHz COMPARED WITH A 0.1 dB RIPPLE PROTOTYPE

In any bandpass filter, even with infinite-Q resonators, the poles are not on the imaginary axis but take positions to the left of this axis in the stable half-plane.

No serious stability problem was encountered with the circuit in Fig. V-9, or in the corresponding three-resonator filter built subsequently. The transistor current could be adjusted so that the unloaded Q of each resonator passed through infinity (as evidenced by the filter insertion loss passing through 0 dB) without oscillation or detuning occurring. Since the transistor current mainly controls the emitter resistance, the filter tuning is nearly independent of current.

The observed sensitivity is about 1 dB change in insertion loss per milliamp change in transistor current. The nominal transistor current for the active resonator is about 10 mA, which can be stabilized within a few percent; thus it is concluded that the filter insertion loss can be stabilized within a fraction of a dB. The observed effects of temperature are shown in Fig. V-13. Above 0°C, but without any

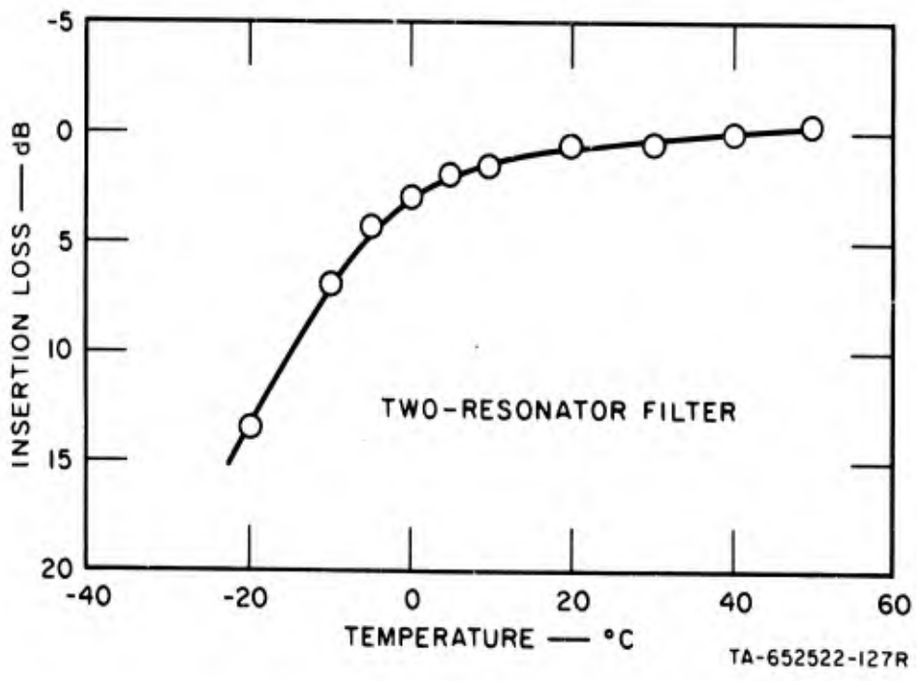

FIG. V-13 INSERTION LOSS TEMPERATURE DEPENDENCE OF THE ACTIVE FILTER IN FIG. V-9

attempt at temperature stabilization, the insertion loss changes rather slowly with temperature at a slope of about 0.05 dB/°C. Therefore, simple temperature stabilization is expected to yield resonators with extremely good temperature stability. Again, very little tuning sensitivity was noted during temperature cycling.

3. Initial Results on Filter Tunability

A brief study has been made of the tunability of filters made with inductive transistors. Referring to Fig. V-8, one approach is to vary the emitter tuning capacitor on each resonator, but quite limited tuning range results. For example, within a single resonator, unity insertion loss could be maintained only over a 19 MHz range at 500 MHz approximately. An alternate approach is to insert a variable capacitor in series with the base inductor L_b (see Fig. V-3). In the first experiment, it was found that unity insertion loss could be maintained (by some adjustment of the transistor current) over a 27 percent range (150 MHz) from 496 to 649 MHz. The instantaneous half-power bandwidth varied from 18 MHz at the low end of the range to 25 MHz at the high end of the range. However, the fractional bandwidth was more constant, increasing from 3.64 percent to 3.86 percent over the same range.

Tuning with a series capacitor in the base lead is preferred because it produces a favorable change in negative resistance along with a change in virtual inductance. Also, since the Q of the base circuit is quite low, a tuning element can more easily be incorporated in the base than in the emitter.

E. Large Signal Limitations of Inductive Transistors

It was mentioned previously that active filters offer a trade-off between filter size and dynamic range. In Fig. V-14 the responses of the active filters in Fig. V-9 are shown for various signal levels. The small-signal insertion loss of 0 dB is degraded to 1 dB with 1.2 mW incident on the filter. The signal level producing 1 dB increase in insertion loss will henceforth be called the filter saturation level. Note in Fig. V-14 that very little change in pass-band shape results at

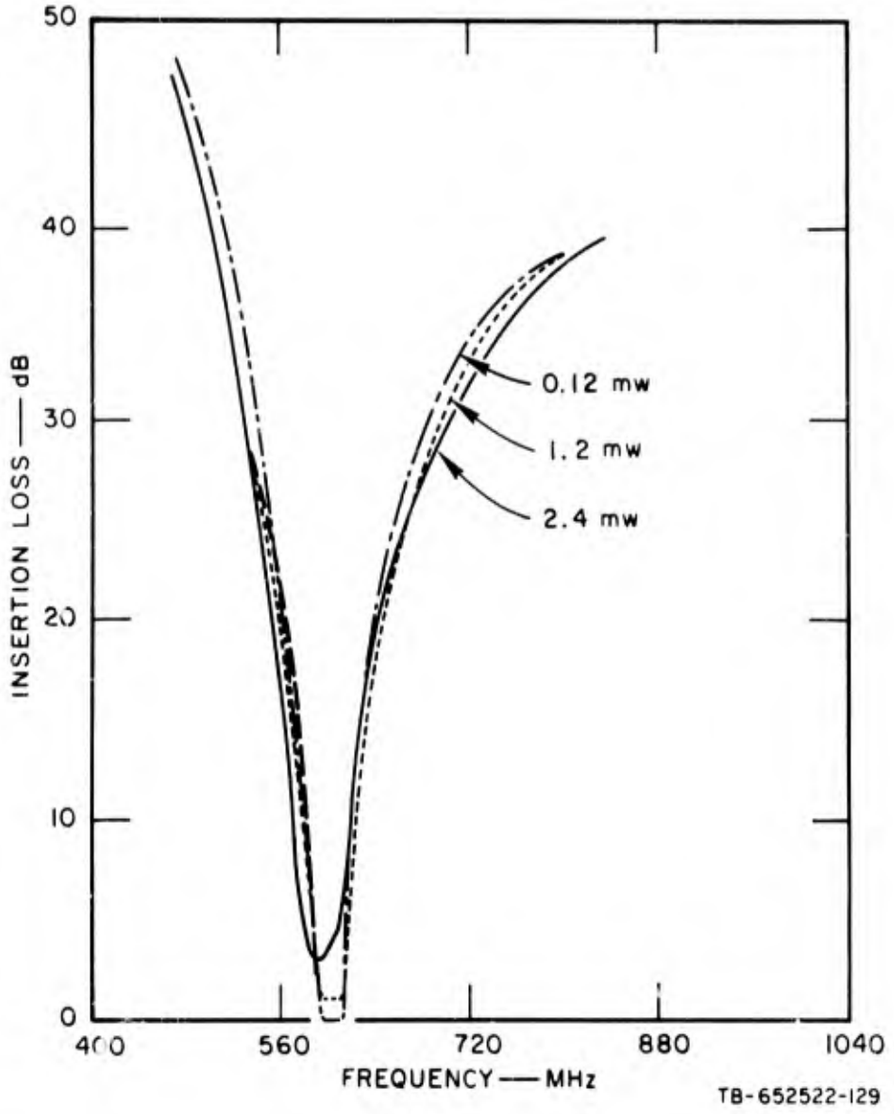

FIG. V-14 COMPARISON OF LARGE- AND SMALL-SIGNAL PASS BAND AND INSERTION LOSS FOR THE TWO-RESONATOR ACTIVE FILTER

the saturation level. Above the saturation level, however, some passband distortion occurs, but this is accompanied by another useful effect, which is depicted in Fig. V-15. The insertion loss produced by large input signals is mainly due to input mismatch which increases above the saturation level. Therefore, the transistor filter has been found to act as a limiter to large input signals.

The large-signal limitations of the active filter result from the nonlinear characteristics of the transistor, and arise at RF levels well below those producing excessive thermal dissipation. Intermodulation and cross modulation are observed in transistors (as in other electron devices) at still lower levels, well below the threshold of saturation. Still, intermodulation and saturation are closely related phenomena.

A common technique for describing large-signal effects is to express the device characteristics with Taylor series. In many devices, a single equation can be used to describe the nonlinear effects. Usually, for example, only the last stage of an amplifier chain needs to be modeled, but in a multistage active filter the largest signal amplitude will occur in different stages in different parts of the frequency band.* It is generally necessary to consider the whole filter when nonlinear effects are being studied, and separate series must be used to represent the input and output characteristics of the device. For example,

$$i_{in} = a_1 V_g + a_2 V_g^2 + a_3 V_g^3 + \ldots \qquad \text{(V-11a)}$$

$$i_{out} = b_1 V_g + b_2 V_g^2 + b_3 V_g^3 + \ldots \qquad \text{(V-11b)}$$

---

*Consider a symmetrical two-resonator bandpass filter, such as that shown in Fig. V-8. Even-mode excitation (using two identical generators at input and output) will yield a voltage V_1 across each resonator. Odd-mode excitation (using out-of-phase generators at input and output) will produce the voltages V_2 and $-V_2$ across the two resonators. Therefore, with only one source applied, the input resonator experiences the voltage $1/2\ (V_1 + V_2)$, while $1/2\ (V_1 - V_2)$ appears across the output resonator, showing that the signal distribution is not symmetrical even in a symmetrical network.

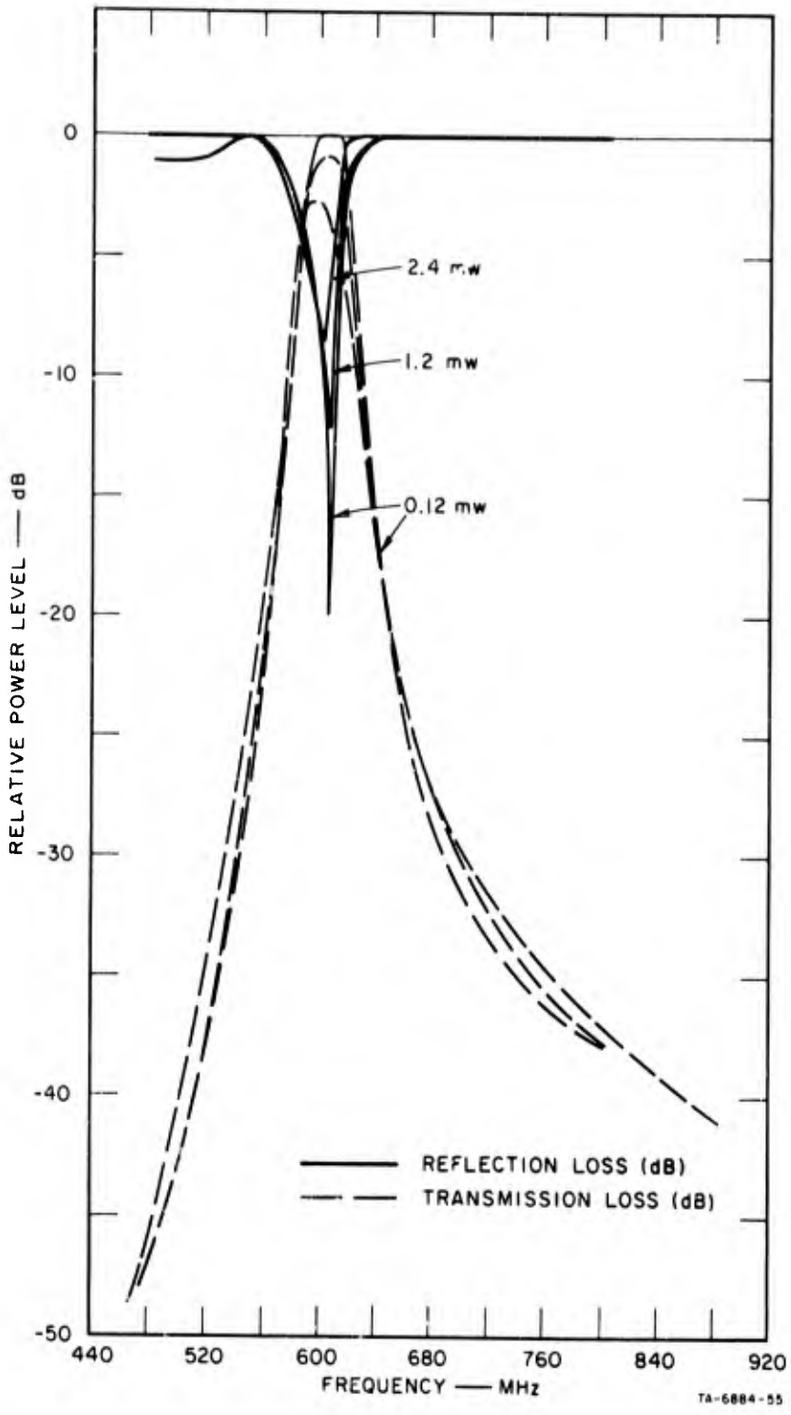

FIG. V-15 SMALL- AND LARGE-SIGNAL REFLECTION CHARACTERISTICS OF TWO-RESONATOR ACTIVE, SHOWING LIMITING EFFECT

where V_g is the external source voltage. However, to simplify the discussion of nonlinear effects in inductive transistor circuits, only a single-resonator filter will be considered. Assuming symmetrical input and output coupling, the two equations in (V-11) then become identical.

The second term in Eq. (V-11a) with coefficient a_2, will be responsible for dc bias shifts and the generation of even-order harmonics when V_g is large. In narrow-bandwidth filter applications, the term with coefficient a_3 is of greater importance. It contributes large-signal effects that are directly observable with inband signals through impedance changes and intermodulation. In Appendix C, a large-signal input admittance is shown to be a function of the applied phasor V:

$$Y_{in} = a_1 + \left(\frac{3a_3}{4}\right) V^2 \quad . \tag{V-12}$$

Similarly, two closely spaced input signals at frequencies ω_a and ω_b, with available powers P_a and P_b respectively, will produce intermodulation products P_{21} at $2\omega_a + \omega_b$ and P_{12} at $2\omega_b + \omega_a$ according to the following relations:

$$P_{21} = K_{21} P_a^2 P_b \tag{V-13a}$$

$$P_{12} = K_{12} P_a P_b^2 \tag{V-13b}$$

where $K_{12} = K_{21}$ is the coefficient of third-order intermodulation. As shown in Appendix C,

$$K_{12} = 36 a_3^2 R_{ge}^4 \tag{V-14}$$

where R_{ge} is the Thevenin equivalent source resistance, as seen by the single resonator under discussion. Comparison of Eqs. (V-12) and (V-14) shows the close relationship between third-order intermodulation and saturation. Experimentally, a_3 can be measured by observing the intermodulation produced by two closely spaced, medium-intensity inband

signals, and then this value can be used to predict the saturation threshold.

In Appendix C, the following expression is derived for a_3 for a transistor in the inverted common-collector configuration:

$$a_3 = \left(\frac{-Z_e}{6I_E^2}\right)\left(\frac{2\left[Z_e + Z_{ge} + (1-\alpha)Z\right] - 3Z_e}{\left[Z_{ge} + Z_e + (1-\alpha)Z^3\right]^5}\right) \qquad \text{(V-15)}$$

where Z_{ge} is the Thevenin equivalent of all impedance elements (input and output) external to the resonator. The analysis leading to Eq. (V-15) has neglected the possible large-signal dependence of alpha and f_α, and has assumed that the major circuit nonlinearity is associated with the emitter junction. Some experimental verification of these approximations will be presented later in this section.

The term $Z_e + Z_{ge} + (1-\alpha)Z$ in the denominator of Eq. (V-15) is the total impedance of the active filter circuit in the small-signal condition. At midband, this term must be positive, real, and nonzero for the filter to be stable, which is equivalent to requiring a finite loaded Q for the resonator. Therefore, the sign of a_3 will be determined by the numerator, which can be observed to go through zero if

$$Z_e = 2\left[Z_{ge} + (1-\alpha)Z\right] \quad . \qquad \text{(V-16)}$$

Since Z_e is current dependent, it is possible to minimize the effects of a_3 for some particular value of transistor current. Figure V-16 shows measurements of the relative output power of a two-resonator filter as a function of bias voltage at two signal power levels differing by exactly 20 dB. Under low-current conditions, the power output for the larger signal exceeded that for the smaller signal by more than 20 dB, implying a positive value of a_3. Similarly, under high-current conditions, the output from the larger signal exceeded that from the smaller signal by less than 20 dB, implying that a_3 is zero at V_{EC} = 18 V (which corresponded to a bias current of about 18 mA per transistor).

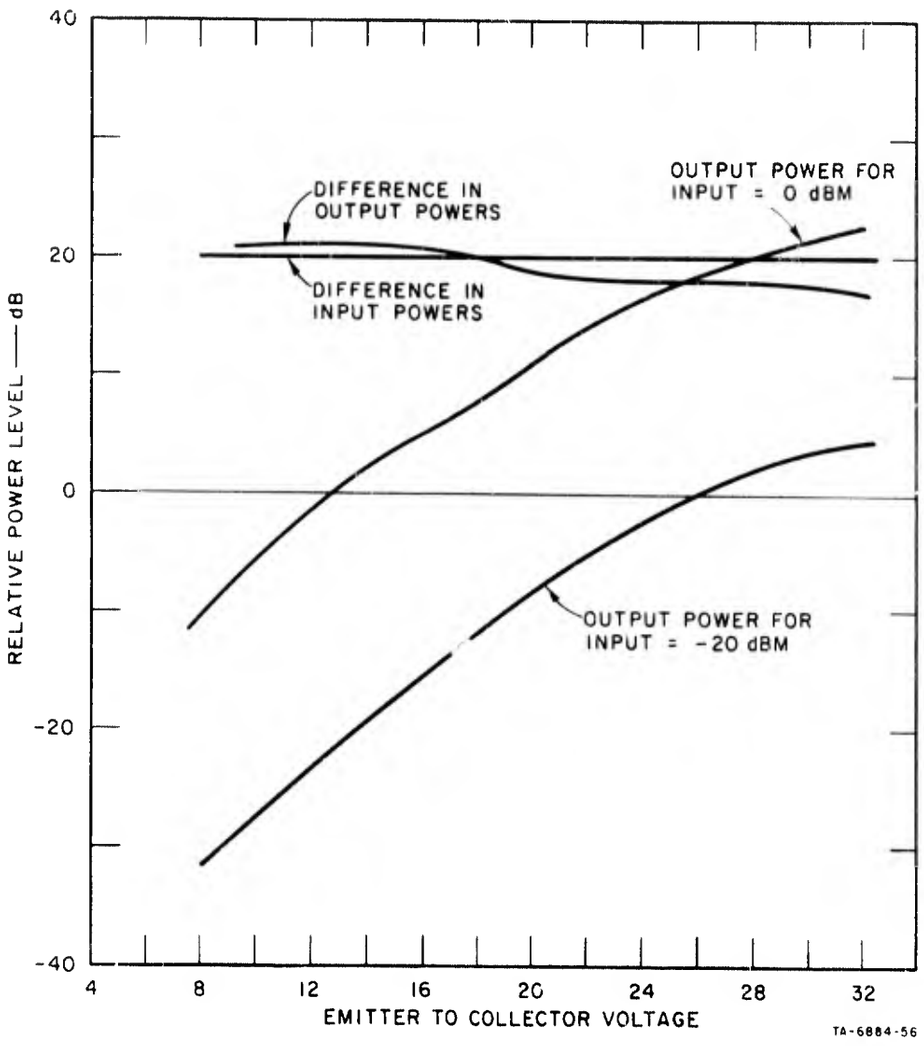

FIG. V-16 COMPARISON OF THE SATURATION EFFECTS PRODUCED BY THE COEFFICIENT a_3 FOR LOW AND HIGH BIAS VOLTAGE (and current). The output power is plotted for two input power levels vs. bias voltage. The output powers differ from the input powers by exactly 20 dB when $a_3 = 0$.

A similar measurement on the coefficient of third-order intermodulation is shown in Fig. V-17.* The measured data dips at a current of about 21 mA, which corresponds to the zero of a_3 as noted in Fig. V-16, although these two measurements were made with somewhat different filter tunings. Third-order intermodulation does not have a deep null when a_3 vanishes, because contributions to the same spurious frequency arise from higher-order intermodulation processes. The data in Figs. V-16 and V-17 show that the large-signal limitations in inductive transistor circuits are fairly well understood, and can be expressed analytically in terms of basic circuit and device parameters.

F. Noise Characterization of Inductive Transistor Filters

The transistor noise model due to Nielsen[20] can be applied to microwave transistors if the parasitic reactances are accounted for adequately. Transistor noise can be attributed to major noise sources in the collector, emitter, and base, as indicated in the inverted common-collector circuit in Fig. V-18(a). The three noise voltages are uncorrelated, to good approximation, wher expressed in the following form:

$$\overline{e_e^2} = 2KTr_e\,\Delta f$$

$$\overline{e_b^2} = 4KTr_b'\,\Delta f \qquad \text{(V-17)}$$

$$\overline{e_c^2} = \frac{2KT\,\alpha_o\,(1-\alpha_o)\,|Z_c^2|\left[1+\left(\frac{f}{\sqrt{1-\alpha_o}\,f_\alpha}\right)^2\right]}{r_e\left[1+\left(\frac{f}{f_\alpha}\right)^2\right]}\,\Delta f \quad .$$

A more convenient form of the inductive transistor circuit for noise analysis is the Norton equivalent in Fig. V-18(b), which has the following circuit elements:

---

*The analysis in this section is for a single-resonator filter, while the experimental data was taken near midband on a two-resonator filter. Near midband, the input resonator experiences the largest signals, so the single-resonator theory can be applied. (See preceding footnote.)

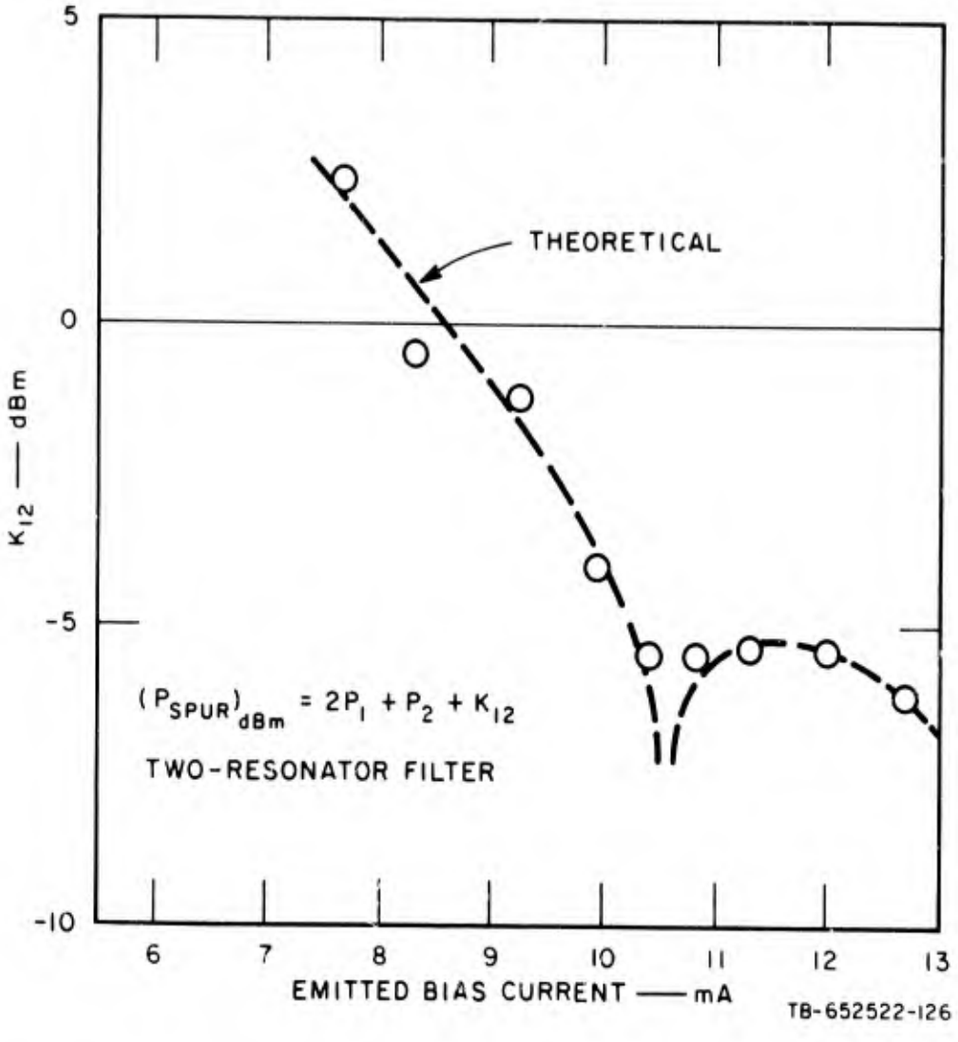

FIG. V-17 MEASURED THIRD-ORDER INTERMODULATION COEFFICIENT vs BIAS CURRENT FOR THE TWO-RESONATOR ACTIVE FILTER

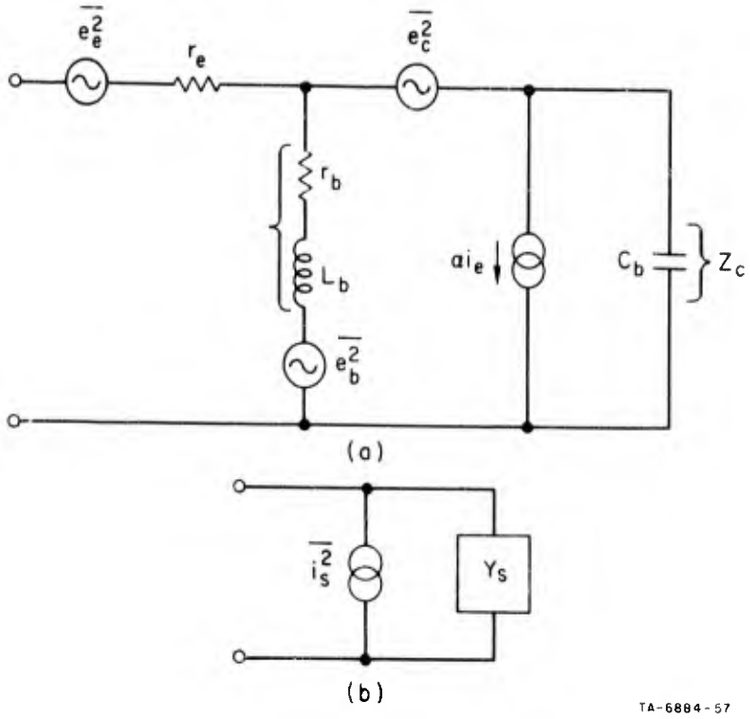

FIG. V-18 (a) Noise sources in the inductive transistor circuit
(b) Norton equivalent circuit

$$\overline{I_s^2} = \frac{\overline{e_e^2} + \overline{e_b^2}\left|\frac{Z}{Z_B}\right|^2 + \overline{e_c^2} + \overline{e_c^2}\left|\frac{Z}{Z_C}\right|^2}{\left|r_e + (1-\alpha)Z\right|^2} \qquad \text{(V-18)}$$

$$\overline{Y_s} = \left[r_e + (1-\alpha)Z\right]^{-1}$$

where Z is the parallel combination of the base and collector impedances (Z_b and Z_c, respectively) and therefore is the same Z as in Fig. V-2.

The general circuit model for noise analysis of the capacitively coupled active bandpass filters is shown in Fig. V-19. The element values depend upon the filter bandwidth and the desired pass-band shape, as described in Ref. 17, Chap. 8. One useful feature of this filter design is that each transistor can be identical, and the desired pass-band shape can be obtained entirely with the coupling capacitors. When the

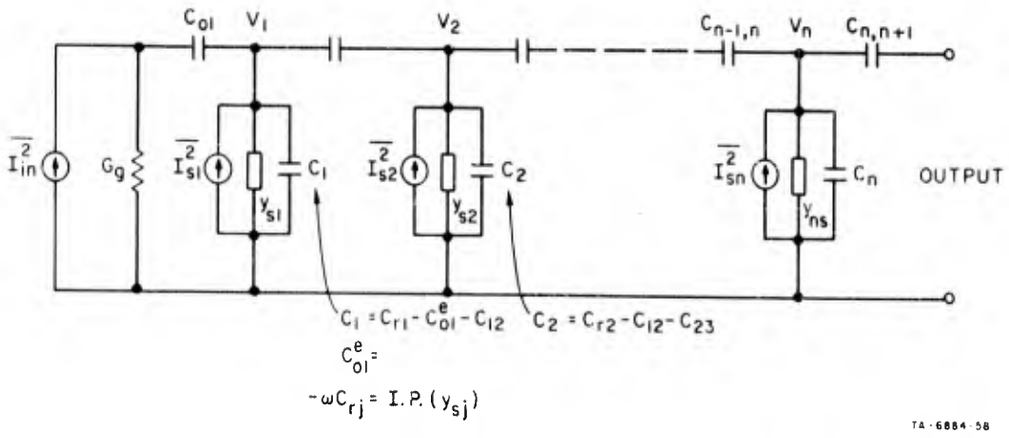

FIG. V-19 NOISE EQUIVALENT CIRCUIT OF THE n-RESONATOR, CAPACITIVELY COUPLED ACTIVE FILTER

transistors are identical, the equivalent short-circuit noise currents $\overline{I_{sk}^2}$ are equal, but they make unequal contributions to the output noise level. Therefore a noise analysis of the circuit in Fig. V-19 requires that the noise power contributions from each transistor be summed in the output. (The individual noise contributions will be uncorrelated.) The noise figure of the filter will be defined in the conventional manner.

$$F = \frac{\text{total mean source noise voltage at the filter output}}{\text{output mean square noise voltage due to the input source only}} \quad . \quad \text{(V-19)}$$

The noise figure for an arbitrary capacitively coupled bandpass filter of the type shown in Fig. V-19 is found to be as follows:

$$F = 1 + N' \left\{ (\omega R_g C_r)^2 \left[1 + \sum_{k=0}^{n-2} \left(\frac{C_{k,k+1}^e}{C_{k+1,k+2}} \right)^2 \right] + \left(\frac{C_r}{C_{01}} \right)^2 \left[1 + \sum_{k=1}^{M} \left(\frac{C_{2k-1,2k}}{C_{2k,2k+1}} \right)^2 \right] \right\} \quad \text{(V-20)}$$

where

$$N' = \frac{r_e}{2R_g} + \frac{r_b'}{R_g}\left|\frac{Z}{Z_B}\right|^2 + \frac{\alpha_o(1-\alpha_o)|Z|^2\left[1+\left(\frac{f}{\sqrt{1-\alpha_o}\,f_\alpha}\right)^2\right]}{2r_eR_g\left[1+\left(\frac{f}{f_\alpha}\right)^2\right]} \qquad \text{(V-21)}$$

$$C^2_{k,k+1} = C_{k,k+1} \qquad k > 0$$

n = number of resonators

$$M = \frac{n-1}{2} \quad , \quad \text{if } n \text{ odd}$$

$$= \frac{n-3}{2} \quad , \quad \text{if } n \text{ even}$$

$$\omega C_r = \text{I.P.}\left(Y_s\right) \quad .$$

The factor N' is the excess noise of each transistor alone, when used as an amplifier with source impedance R_g^{20}. Inspection of Eq. (V-20) shows that the active-filter circuit tends to have a higher noise figure than would the same set of transistors used as an amplifier. However, the actual noise figure depends strongly on the filter bandwidth. In a narrow-bandwidth filter, large impedance transformations are required between sections, to produce the desired selectivity, but these transformations are not generally the most favorable for noise reduction. When broad-bandwidth active filters are compared with transistor amplifiers (which are usually quite broadband), comparable noise figures will result.

Further insight regarding the noise characteristics of the filters under discussion is gained by considering only a two-resonator filter. In this case, the general expression in Eq. (V-20) reduces to the following:

$$F = 1 + N'\left\{\left[\left(\omega R_g C_r\right)^2 + \left(\frac{C_r}{C_{o1}}\right)^2\right] + \left(\omega R_g C_r\right)^2\left(\frac{C^e_{o1}}{C_{12}}\right)^2\right\} \text{(two-resonator filter)}. \qquad \text{(V-22)}$$

For narrow fractions bandwidths w, Eq. (V-22) reduces to the following approximate form:

$$F \cong 1 + N' \left\{ \frac{\omega_\alpha R_g}{K\ \omega r_b} \left[\frac{\omega_\alpha R_g}{K\ \alpha r_b} + \frac{1}{W} \left(g_1 + \frac{g_2}{g_1} \right) \right] \right\} \qquad \text{(V-23)}$$

where $K = 1 + \omega^2 (Q_\alpha - 1)/\omega_\alpha^2$ and where g_1 and g_2 are the low-pass prototype elements used in the design. For the narrow-bandwidth case where Eq. (V-23) applies, the last term on the right is much larger than the preceding term, which shows that the filter noise figure increases inversely with bandwidth. Another conclusion of interest concerns the dependence of F upon r_b. Although the term in brackets in Eq. (V-23) increases inversely with r_b, the term in N' involving r_b is often dominant. Therefore, to first approximation, F is largely independent of r_b. A similar observation can be made regarding the near independence of F upon frequency below the alpha-cutoff frequency.

Example

The noise figure of the two-resonator filter described in Sec. II-E was measured. Two experimental techniques were used, as described in Appendix D. The measured noise figures by the two methods are 9.05 dB and 9.25 dB. Substituting the following set of parameter values, which closely approximate the measured circuit, into Eq. (V-22) yields a theoretical noise figure of 9.3 dB.

$r_b = 20$ ohms

$\omega C_r = 0.02$ ohms

$R_g = 50$ ohms

$r_e \ll R_g$

$\alpha_o = 1$

$|Z| \cong |Z_b|$, since $Q_\alpha \cong 1$

REFERENCES

1. M. S. Ghausi and F. D. McCarthy, "A Realization of Transistor Gyrators," Proc. Natl. Electronics Conf., Vol. 19, p. 396 (1963).

2. B. A. Shenoi, "Practical Realization of a Gyrator Circuit and RC-Gyrator Filters," IEEE Trans. on Circuit Theory, Vol. CT-2, No. 3, p. 374 (September 1965).

3. S. S. Haykim, "RC-Gyrator Low-Pass Filter," Proc. IEEE, Vol. 113, No. 9, p. 1504 (September 1966).

4. K. L. Su, "A Transistor-Circuit Realization of the Inductor," Proc. IEEE, Letters, Vol. 54, No. 12, p. 2025 (December 1966).

5. D. F. Sheahan and H. J. Orchard, "Bandpass-Filter Realization Using Gyrators," Electronics Letters, Vol. 3, No. 1, p. 39 (December 1966).

6. J. Yamaguchi, "On the Inductive Reactance and Negative Resistance in the Transistor," J. Phys. Soc. (Japan), Vol. 11, p. 717 (June 1956).

7. R. E. Burgess, "Emitter-Base Impedance of Junction Transistors," J. Electron, Vol. 2, p. 301 (November 1956).

8. J. F. Gibbons, "An Analysis of the Modes of Operation of a Simple Transistor Oscillator," Proc. IRE, Vol. 49, p. 1383 (September 1961).

9. J. Lindmayer and C. Wrigley, "Some Generalities of Transit-Time Mode for Two-Barrier Devices," J. Electron, Vol. 13, p. 137 (1962).

10. S. C. Dutta Roy, "The Inductive Transistor," IEEE Trans. on Circuit Theory, Vol. CT-10, p. 113 (March 1963).

11. J. E. Norman and R. A. Greiner, "The Small-Signal Inductive Effect in a Long P-I-N Diode," IEEE Trans. on Electron Devices, Vol. ED-10, p. 171 (May 1963).

12. J. Lindmayer and W. North, "The Inductive Effect in Transistors," Solid State Electronics, Vol. 8, p. 409 (1965).

13. J. A. Archer, J. F. Gibbons, and G. M. Purnaiga, "Use of Transistor-Simulated Inductance as an Interstage Element in Broadband Amplifier," IEEE Trans. on Solid-State Circuits, Vol. SC-3, No. 1, p. 12 (March 1968).

14. D. K. Adams and R. Y. Ho, "The Transistor, A Microwave Filter Element," paper presented at the G-MTT International Microwave Symposium, Detroit, Michigan (May 1968).

15. D. E. Thomas and J. L. Moll, "Junction Transistor Short-Circuit Current Gain and Phase Determination," Proc. IRE, Vol. 46, pp. 1177-1184 (June 1958).

16. G. R. Jindal, "High Q Single Inductive Transistor Arrangement," IEEE Proc. Letters, Vol. 55, No. 1, p. 105 (January 1967).

17. G. L. Matthaei, L. Young, and E. M. T. Jones, Microwave Filters, Impedance Matching Networks, and Coupling Structures, p. i, Chap. 8 (McGraw-Hill Book Company, Inc., New York, 1964).

18. O. Hickelman, et al., "Interference Analysis of New Components and Circuits," RADC-TDR-64-161 (May 1964).

19. D. Kornfeed, G. M. Kanishak, and S. Becker, "Investigation of the RFI due to Nonlinearities in Transistor Amplifiers," paper presented at the IEEE 1967 Symposium on Electromagnetic Compatibility (July 1967).

20. E. G. Nielsen, "Behavior of Noise Figure in Junction Transistor," Proc. IRE, Vol. 45, No. 7, p. 957 (July 1957).

VI CONCLUSIONS

A. Slot Line

The ability of slot line to propagate a tightly bound wave with velocity substantially less than that of light has been verified theoretically and experimentally. Slot line can be used compatibly with microstrip located on the opposite side of the dielectric substrate. Couplers, filters, and other components can be made with slot line or combinations of slot and microstrip line. The slot geometry is convenient for connecting shunt elements such as diodes, resistors, and capacitors, since the wave's voltage exists across the slot rather than through the substrate as in microstrip. Elliptically polarized regions of H field near the slot may prove useful in ferrite components. The second-order solution derived in this report has proved highly versatile, yielding slot-line wavelength, phase velocity, group velocity, characteristic impedance, and effect of adjacent electric and magnetic walls. Future applications of the second-order solution will include coupling between slots and effect of metal thickness. Measurements have thus far been limited to λ'/λ data on a single test piece. Additional measurements of λ'/λ and Z_o are needed as a check on the theoretical computations.

B. Design Considerations for Microstrip Parallel Coupled Resonator Bandpass Filters and Directional Couplers

Both the modified and new equations for microstrip parallel-coupled-resonator filters produce satisfactory designs. In most cases there results a skewness in the VSWR response, but this is usually satisfactorily remedied by slightly lengthening the first and last sections of the filter. The skewness of the VSWR is more apparent for narrow-band designs than for wide-band ones.

Based on the several examples presented in Sec. III, it may be concluded that both the modified and new equations produce narrow-bandwidth microstrip filter designs that have responses only slightly

degraded from those of corresponding designs in homogeneous media. Although there is in all cases a shift in the center of the pass band, it is predictable by a simple formula for those designs based on the modified equations. The same formula is not very good for designs based on the new equations, although in all the cases which were examined the shift was always less than the formula predicted.

For wide-band designs, again both sets of equations can be used. But the new equations, particularly for $\alpha \approx 1.0$, produce designs which have better controlled pass-band responses in that the bandwidth and ripple more nearly meet the design specifications. Here again, the formula for the shift in the center of the pass band works well for designs based on the modified equations, but can only be used as an upper limit for those designs based on the new equations. However, for $\alpha \approx 1.0$ the shift is sufficiently small that this is not an important factor.

The directivity of microstrip coupled transmission-line directional couplers is seriously degraded by differences in the even- and odd-mode propagation velocities. For a given ratio of even- to odd-mode velocity the degradation is greater for weak couplers. The directivity cannot be improved by perturbing the even- or odd-mode impedance since their contribution to the directivity is orthogonal to the contribution from differences in the even- and odd-mode velocities. However, it does seem feasible that substantial improvement in directivity can be obtained by designing a small mismatch in each port, but suitably located away from the coupled region. This would not seriously affect the VSWR.

Three other important characteristics of microstrip directional couplers are: (1) The center of the coupling band is shifted and the peak coupling slightly decreased from its nominal value. These effects, however, may be predicted from graphs given in Sec. III. (2) The VSWR is not seriously degraded. (3) The quadrature relationship of the phase of waves at the coupled ports is maintained in the pass band to within 1.5 degrees.

C. Theory and Design of Transmission-Line All-Pass Equalizers

The equalizer network consisting of a three-port circulator having (1) the second port terminated in a reactance network of cascaded commensurate transmission lines, and (2) a matched line $n\theta$ long in series with either the input or output port is a canonical network capable of realizing any arbitrary all-pass commensurate transmission-line network transfer function of the variable t. The network of cascaded commensurate transmission lines is intimately related to the Hurwitz polynomial of the transfer function, and a recursion formula for this relationship was established.

The network of cascaded commensurate transmission lines may be replaced by an equivalent network, or approximately equivalent network, whenever such alternate designs are required, either because of practical realizability constraints, or other considerations. Two such networks were described. Also, the three-port circulator may be replaced by a quadrature 3-dB directional coupler, and the same theory applies. In that case the normally coupled ports of the directional coupler are terminated in identical reactance networks, and the normally isolated port of the coupler becomes the output port of the equalizer. In narrow-band applications, the frequency dependence of the coupler may be neglected.

Dissipation loss was found to be very nearly proportional to the delay and to have negligible effect on the time delay response. A method for determining the constant of proportionality was stated. Also, a formula was presented for the midband loss of the general n-section equalizer.

D. Active Filters for UHF and Microwave Frequencies

An active-filter technique has been described in this report which uses a basic impedance rotation effect that is present in any transistor at higher frequencies. Study of this effect has shown that stable, high-Q inductance can be realized up to and above the alpha-cutoff frequency of the transistors used. Therefore, useful and compact active

filters can be built at the lower microwave frequencies where transistors are presently available. Since conventional resonators and filters are physically large in the lower microwave region, the potential usefulness of transistor filters is quite apparent.

Several active filters have been built at UHF to demonstrate the inductive transistor principle. Stable performance with 0 dB insertion loss and sharp pass-band corners has been observed. Measurements made on current and temperature sensitivity show that the circuits used are readily amenable to stabilization against environmental changes. Wide dynamic ranges have been observed, in agreement with analytical treatments of noise figure, intermodulation, and large-signal saturation thresholds. The inductive transistor filter is recommended for all types of small-signal filtering and multiplexing at lower microwave frequencies. In future advancement of the active microwave filter art, it is expected that the inductive transistor effect will play an important role.

Appendix A

ALGORITHM FOR SYNTHESIS OF REACTANCE FUNCTIONS IN A CASCADE OF COMMENSURATE TRANSMISSION LINES

Appendix A

ALGORITHM FOR SYNTHESIS OF REACTANCE FUNCTIONS IN A CASCADE OF COMMENSURATE TRANSMISSION LINES

Rule: Let $H_n(t)$ be the associated Hurwitz function of the normalized function $y_n(t)$. That is,

$$y_n(t) = \frac{H_n(t) - H_n(-t)}{H_n(t) + H_n(-t)} \qquad \text{(A-1)}$$

and

$$H_n(t) = \text{numerator of } y_n(t) + \text{denominator of } y_n(t) \quad . \qquad \text{(A-2)}$$

The value of the jth line admittance of the cascade transmission-line network shown in Fig. IV-5 is given by the formula

$$y_j = \frac{H_j(1) - H_j(-1)}{H_j(1) + H_j(-1)} \quad \text{for} \quad j = n, n-1, \ldots, 1 \quad . \qquad \text{(A-3)}$$

$H_{j-1}(t)$ is given by

$$H_{j-1}(t) = \frac{1}{4(t^2 - 1)} \left\{ tH_j(t)\left[H_j^2(1) + H_j^2(-1)\right] - 2tH_j(-t)H_j(1)H_j(-1) - H_j(t)\left[H_j^2(1) - H_j^2(-1)\right] \right\} \quad \text{for} \quad j = n, n-1, n-2, \ldots, 2 \quad . \qquad \text{(A-4)}$$

The above formulas apply equally to the dual network of Fig. IV-5. In that case the output in Fig. IV-5 is short circuited, and $y_n(t)$ and y_i in Eqs. (A-1) through (A-4) are to be replaced by $z_n(t)$ and z_i.

Appendix B

MICROWAVE EQUIVALENT CIRCUIT OF THE INVERTED COMMON-COLLECTOR TRANSISTOR CONFIGURATION

Appendix B

MICROWAVE EQUIVALENT CIRCUIT OF THE INVERTED COMMON-COLLECTOR TRANSISTOR CONFIGURATION

The high frequency equivalent circuit of any transistor configuration is strongly dependent upon the package configuration. Since most high-frequency transistors are made with planar-construction techniques, the model in Fig. B-1 is a general representation of the reactive parasitics in high-frequency transistors. In the study reported in Sec. V, the circuit in Fig. B-1 is assumed to be reducible to the model in Fig. V-3. The following observations show the relationship between these two circuit models.

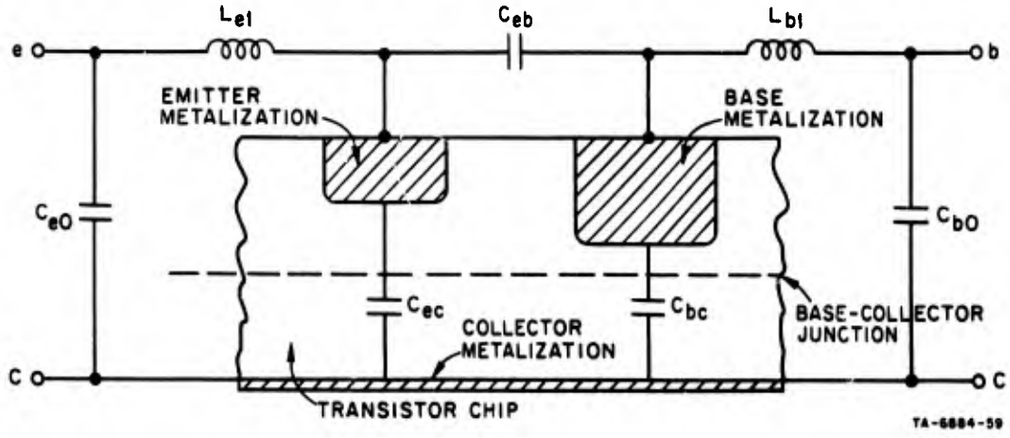

FIG. B-1 TRANSISTOR MODEL, SHOWING PACKAGE AND INTERELECTRODE PARASITICS

(1) The interelectrode capacity C_{eb} is small and appears in parallel with the rather large injection capacity C_e [see Eq. (V-2a) in the text] together with the (usually small) emitter resistance r_e. Therefore, C_{eb} is neglected in this analysis.

(2) The interelectrode capacity C_{ec}, the emitter lead inductance L_{el}, and the emitter lead capacity C_{eo}

form a pi-network that can usually be reduced to an effective input capacity C_e', as indicated in Fig. V-3. Further correction can be made by transforming the virtual inductance being synthesized through the pi-network.

(3) The base collector interelectrode capacity C_{bc} adds directly to the space-charge capacity of the junction, with the latter usually being the larger contribution. The base lead capacity C_{bo} will have a small effect and can usually be combined with the lead inductance L_{bl} to yield an effective inductance $L_b = L_{bl} - 1/\omega^2 C_b$. Therefore, over modest bandwidths, the base-circuit parasitics can be represented by the elements L_b and C_b shown in Fig. V-3.

Appendix C

LARGE SIGNAL CHARACTERIZATION OF THE INDUCTIVE TRANSISTOR CIRCUIT

Appendix C

LARGE SIGNAL CHARACTERIZATION OF THE INDUCTIVE TRANSISTOR CIRCUIT

The equivalent circuit for a symmetrical, one-resonator filter may be represented as shown in Fig. C-1, where Z_{ge} is the Thevenin equivalent impedance of the circuit external to the inductive transistor. The

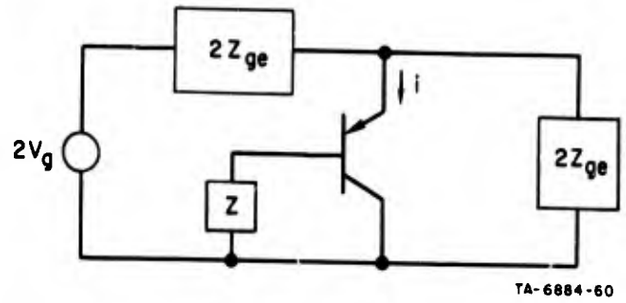

FIG. C-1 EQUIVALENT CIRCUIT OF A SYMMETRICALLY COUPLED, SINGLE-RESONATOR FILTER

transistor current is

$$i = I_E + i_e = I_E\, e^{-1/V_T\left\{V_g - \left[Z_{ge} + (1-\alpha)Z\right] i_e\right\}} \qquad \text{(C-1)}$$

where I_E is the dc bias current and i_e is the RF component of the emitter current, and $V_T = q/kT$ is the equivalent thermal potential. If the exponential form of the input current is expressed by a Taylor expansion, then it is

$$i_{in} = a_0 + a_1 V_g + a_2 V_g^2 + a_3 V_g^3 + \ldots + a_n V_g^n \qquad \text{(C-2)}$$

where

$$a_n = \frac{1}{n!}\left[\frac{d^n i_n}{dV_g^n}\right]_{V_g=0} . \qquad \text{(C-3)}$$

Differentiation yields

$$a_0 = I_E \tag{C-4}$$

$$a_1 = \left[Z_e + Z_{ge} + (1 - \alpha)Z\right]^{-1} \tag{C-5}$$

$$a_2 = \frac{Z_e}{2I_E}\left[Z_e + Z_{ge} + (1 - \alpha)Z\right]^{-3} \tag{C-6}$$

$$a_3 = \left(-\frac{Z_e}{6I_E^2}\right)\left(\frac{2\left[Z_e + Z_{ge} + (1 - \alpha)Z\right] - 3Z_e}{\left[Z_e + Z_{ge} + (1 - \alpha)Z\right]^5}\right) . \tag{C-7}$$

If we assume the input voltage $V_g = V \sin \omega t$, then the input current, including terms up to the third order, may be expressed as

$$i_{in} = \left(a_0 + \frac{V^2}{2} a_2\right) + \left(a_1 + \frac{3V^2}{4} a_3\right) V \sin \omega t - \frac{a_2 V^2}{2} \cos 2\omega t$$

$$- \frac{a_3 V^3}{4} \sin 3 \omega t \tag{C-8}$$

from which the large-signal input impedance can be identified as

$$Z_{in} = a_1 + \frac{3V_3}{4} a_3 \tag{C-9}$$

which is quoted as Eq. (V-12) in the text.

Third-order intermodulation can be analyzed by letting $V_g = V_1 \sin \omega_1 t + V_2 \sin \omega_2 t$. The spurious current at $2\omega_2$ is then

$$i_{21} = \frac{3a_3 V_1 V_2^2 \sin\left(2\omega_2 - \omega_1\right)}{4} \tag{C-10}$$

which divides between the source and load portions of the circuit. The output spurious power is then

$$P_{21} = \frac{i_{21}^2 R_{ge}}{8} \qquad \text{(C-11)}$$

where R_{ge} is the real part of Z_{ge}. The available signal powers at ω_1 and ω_2 are

$$P_1 = V_1^2/8R_{ge} \qquad \text{(C-12a)}$$

$$P_2 = V_2^2/8R_{ge} \qquad \text{(C-12b)}$$

so

$$P_{21} = 36\, a_3^2\, P_1\, P_2^2\, R_{ge}^4 \qquad \text{(C-13)}$$

which is used in Eqs. (V-13) and (V-14) in the text.

Appendix D

NOISE MEASUREMENT TECHNIQUES FOR ACTIVE FILTERS

Appendix D

NOISE MEASUREMENT TECHNIQUES FOR ACTIVE FILTERS

Figure D-1 is a block diagram of the setup to measure the noise figure of the active filter. The basic elements used to measure the noise figure are the Hewlett-Packard Gass Discharge Noise Source, Type 349A, and the Hewlett-Packard Noise Figure Meter 340A. For convenience,

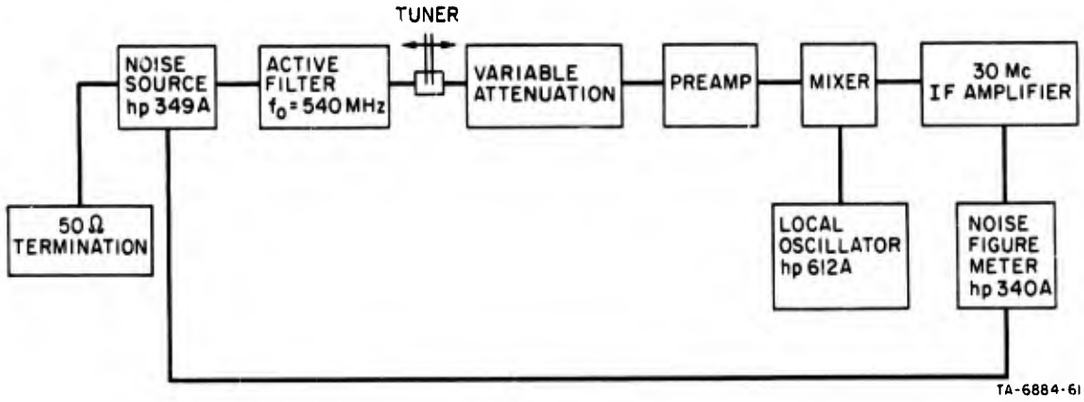

FIG. D-1 BLOCK DIAGRAM OF EQUIPMENT USED TO MEASURE ACTIVE FILTER NOISE FIGURE

these components can be grouped into the three cascaded networks shown in Fig. D-2. First, is the active filter. The second network is a variable attenuator, and the third network consists of a preamplifier, a balanced-detector mixer and its associated components, the IF amplifier, and the noise-figure meter. The overall noise figure of the three

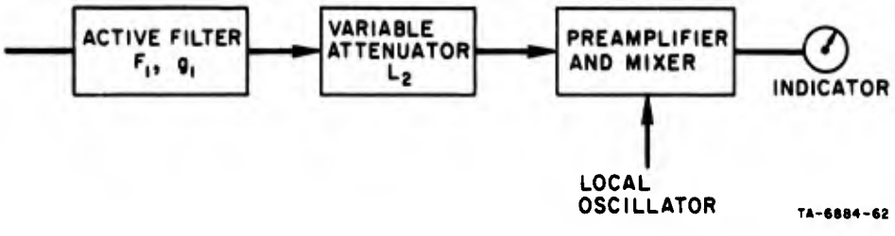

FIG. D-2 SIMPLIFIED EQUIVALENT NETWORK FOR FIG. D-1

cascade network is

$$F = F_1 + L_2 - 1 + (F_3 - 1\ L_2) \qquad \text{(D-1)}$$

where F_1 is the noise figure of the first network; i.e., the active filter L_2 is the attenuation of the second network, and F_3 is the noise figure of the third network. The insertion loss of the active filter is assumed to be 0 dB.

The overall noise figure F' was measured for various attenuation settings of the network 2, as shown in Fig. D-3. From Eq. (D-1) the noise figure of the active filter can be taken to be 1 plus the value of F_1 measured for $L_2 = 0$. From the reading of the intersection of the F' curve and the vertical axis, the noise figure of the active filter was found to be $F_1 = 9.05$ dB.

As a check of this measure result, the noise figure of the active filter was also measured directly. Figure D-4 is a block diagram of the setup for the direct noise measurement. The noise figure F'' of the system excluding the active filter is first measured. The overall noise figure F' (including the active filter) is then measured. The noise figure of the active filter, F_1, can be easily calculated from these two measurements. It is

$$F_1 = F' - (2F'' - 1) \quad . \qquad \text{(D-2)}$$

We note here that the factor 2 in Eq. (D-2) is introduced by the very narrow-band active filter, which eliminates one-half of the noise input to the mixer. The result obtained in this way is $F_1 = 9.25$ dB, which is very close to that obtained by the variable attenuator method.

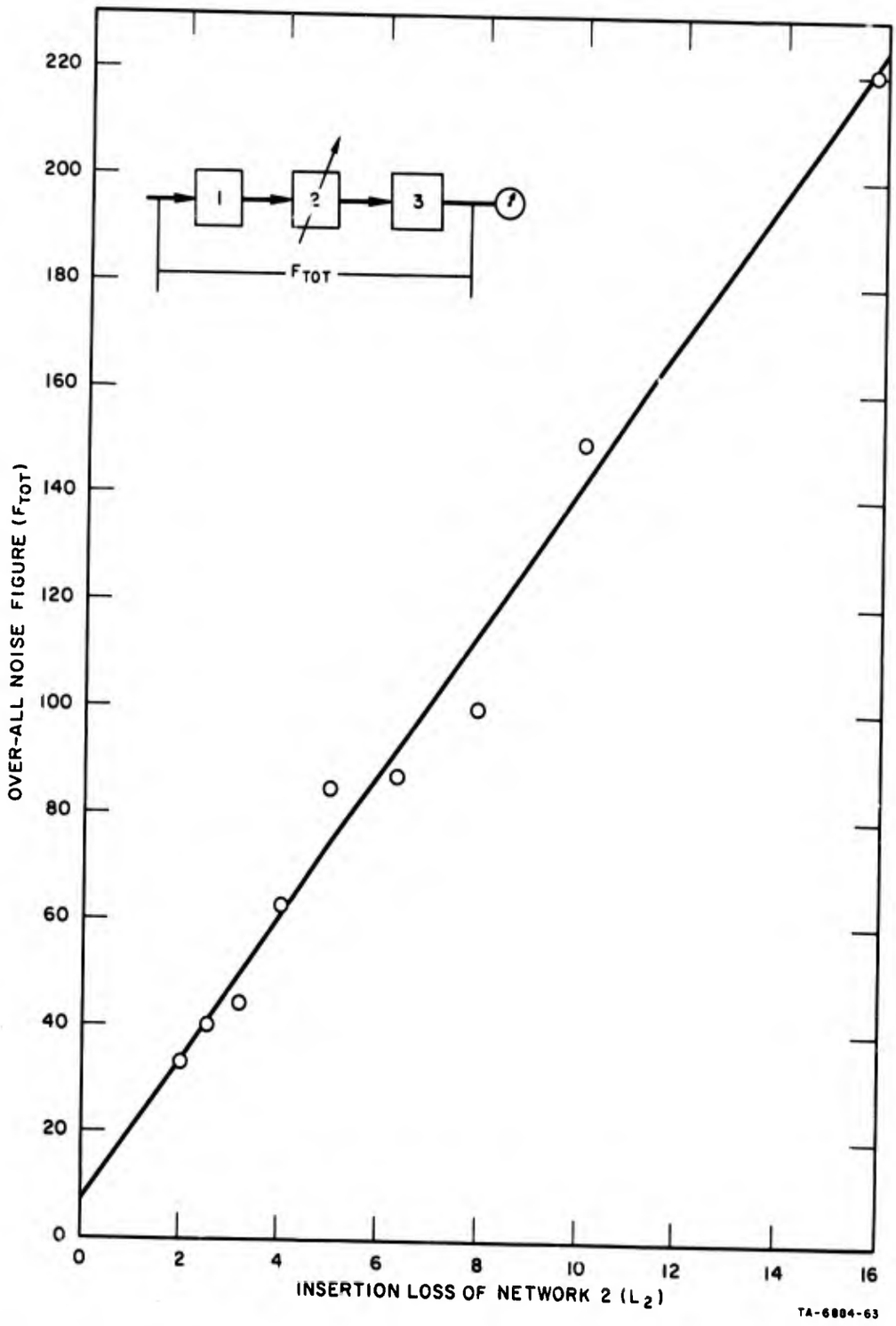

FIG. D-3 NOISE FIGURE OF THE NETWORK IN FIG. D-2 vs. INSERTION LOSS OF L_2

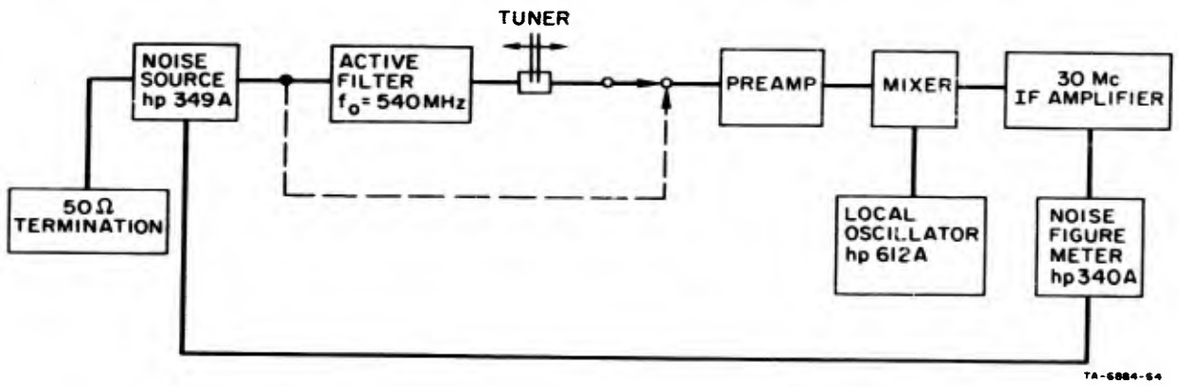

FIG. D-4 BLOCK DIAGRAM OF EQUIPMENT USED FOR THE DIRECT MEASUREMENT OF ACTIVE FILTER NOISE FIGURE

UNCLASSIFIED

Security Classification

DOCUMENT CONTROL DATA - R & D

(Security classification of title, body of abstract and indexing annotation must be entered when the overall report is classified)

1. ORIGINATING ACTIVITY *(Corporate author)*
Stanford Research Institute
333 Ravenswood Avenue
Menlo Park, California 94025

2a. REPORT SECURITY CLASSIFICATION
UNCLASSIFIED

2b. GROUP
N/A

3. REPORT TITLE

MICROWAVE SYNTHESIS TECHNIQUES

4. DESCRIPTIVE NOTES *(Type of report and inclusive dates)*
Annual Report Covering the Period 1 October 1967 to 30 June 1968

5. AUTHOR(S) *(First name, middle initial, last name)*

Edward G. Cristal David K. Adams Raymond Y. C. Ho Seymour B. Cohn

6. REPORT DATE	7a. TOTAL NO. OF PAGES	7b. NO. OF REFS
September 1968	166	45

8a. CONTRACT OR GRANT NO.	9a. ORIGINATOR'S REPORT NUMBER(S)
DAAB07-68-C-0088	Annual Report
b. PROJECT NO.	SRI Project 6884
c.	9b. OTHER REPORT NO(S) *(Any other numbers that may be assigned this report)*
d.	ECOM-0088-1

10. DISTRIBUTION STATEMENT
Each transmittal of this document outside the Department of Defense must have prior approval of CG, U.S. Army Electronics Command, Fort Monmouth, New Jersey, Attn: AMSEL-KL-EM.

11. SUPPLEMENTARY NOTES	12. SPONSORING MILITARY ACTIVITY
	U.S. Army Electronics Command Fort Monmouth, New Jersey 07703 Attn: AMSEL-KL-EM

13. ABSTRACT

Four major topics of research related to microwave synthesis techniques are covered: slot-line theory and applications, microstrip parallel-coupled-resonator filters, commensurate transmission-line all-pass equalizers, and active filters for UHF and microwave frequencies.

Slot line consists of a narrow gap in a conductive coating on one side of a dielectric substrate, the other side of the substrate being bare. If the substrate's permittivity is sufficiently high, such as ϵ_r = 10 to 30, the slot-mode wavelength will be much smaller than free-space wavelength, and the fields will be closely confined to the slot. Possible applications of slot line to filters, couplers, ferrite devices, and circuits containing semiconductor elements are discussed. Slot line can be used either alone or in conjunction with microstrip line on the opposite side of the substrate. A "second-order" analysis yields formulas for slot-line wavelength, phase velocity, group velocity, characteristic impedance, and effect of adjacent electric and magnetic walls.

Modified and alternative design equations for microstrip parallel-coupled-resonator filters are presented. Computed VSWR responses are given for designs having coupled lines with even- to odd-mode propagation velocity ratios of 1.0, 0.95, and 0.90. The responses show that practical, controlled designs are obtainable in all cases. Also presented are useful design data for microstrip directional couplers.

A general theory of commensurate transmission-line all-pass equalizers operating in either TEM, TE, or TM modes is presented. Application of the theory to practical problems is straightforward, and circuit realizations of the equalizers are often simply related to easily computed design curves. Although the theory, strictly speaking, is for commensurate transmission-line networks, it is not essential that the network being equalized, or even that the equalizer itself, be of commensurate-length

DD FORM 1 NOV 1473

UNCLASSIFIED

Security Classification

14 KEY WORDS	LINK A		LINK B		LINK C	
	ROLE	WT	ROLE	WT	ROLE	WT
Slot Line						
Microstrip						
Filters						
Equalizers						
Active Filters						

Item 13. Abstract (Continued)

lines. Design formulas for narrow-band equalizers of up to two cavities are presented, and a method for extending the extending the design to a greater number of cavities is described. The effect of equalizer dissipation loss is investigated and briefly described. Two example designs are presented.

A technique is described for using transistors directly as high-Q inductors at microwave frequencies. Several experimental bandpass filters have been built and tested to verify usefulness of the inductive transistor circuit. Stable filters with unity insertion loss have been realized at UHF. Observations made during temperature cycling show that environmental stabilization can also be achieved. Analysis has been made of noise figure and nonlinear distortion, and supporting experimental data are provided. The inductive transistor circuit is expected to be practical for a variety of small-signal filtering and multiplexing applications.